Search for Technicolor with the OPAL Detector in e^+e^- Collisions at the Highest LEP Energies

Diplomarbeit

Institut für Experimentalphysik
Universität Hamburg

vorgelegt von

Nils Gollub

November 2001

Abstract

A search for the production of Technicolor particles in e^+e^- collisions at the highest centre–of–mass energies at LEP is presented based on data collected by the OPAL detector at $\sqrt{s} \approx 200-209\,\mathrm{GeV}$. Technicolor theories offer an alternative to the Higgs mechanism as implemented in the Standard Model of particle physics for the generation of mass. The search has been performed for the processes $e^+e^- \to \rho_T^0/\omega_T \to \pi_T^+\pi_T^- \to b\bar{q}\bar{b}q'$ and $e^+e^- \to \rho_T^0/\omega_T \to \pi_T^+ W_L^- \to \bar{b}q\bar{q}'q''$. No excess over the expectation from Standard Model processes is observed. Therefore upper limits for the production cross–sections as a function of the technipion mass m_{π_T} are derived. The results are interpreted within the Technicolor Straw Man Model and regions in the $(m_{\rho_T/\omega_T},\, m_{\pi_T})$ plane are excluded.

Zusammenfassung

In dieser Arbeit wird die Suche nach Technicolor–Teilchen in e^+e^-–Kollisionen bei den höchsten LEP Energien beschrieben. Sie basiert auf Daten, welche vom OPAL Detektor im Laufe des Jahres 2000 bei Schwerpunktsenergien von $\sqrt{s} \approx 200-209\,\mathrm{GeV}$ aufgezeichnet wurden. Technicolor–Theorien bieten eine Alternative zum Higgs–Mechanismus des Standard–Modells um Teilchenmassen zu erzeugen. Die betrachteten Produktionskanäle sind $e^+e^- \to \rho_T^0/\omega_T \to \pi_T^+\pi_T^- \to b\bar{q}\bar{b}q'$ und $e^+e^- \to \rho_T^0/\omega_T \to \pi_T^+ W_L^- \to \bar{b}q\bar{q}'q''$. Es wird kein Überschuss über die vom Standard–Modell erwarteten Teilchenraten beobachtet. Daher werden obere Schranken für die Wirkungsquerschnitte der untersuchten Prozesse in Abhängigkeit von der Technipion–Masse bestimmt. Die Ergebnisse werden im Rahmen des "Technicolor Straw Man Model's" interpretiert und ermöglichen den Ausschluss der Produktion von Technicolor–Teilchen für Bereiche der $(m_{\rho_T/\omega_T},\, m_{\pi_T})$ Ebene.

Contents

1 Introduction **3**

2 Theory **7**

2.1 The Standard Model 7

2.1.1 The Electro–Weak Interaction 7

2.1.2 The Strong Interaction 9

2.1.3 Spontaneous Symmetry Breaking 11

2.2 Technicolor 16

2.2.1 Why Technicolor ? 16

2.2.2 Technicolor (TC): Weak Gauge Boson Masses 17

2.2.3 Extended Technicolor (ETC): Fermion Masses 18

2.2.4 Realistic Models 20

2.3 The Technicolor Straw Man Model 20

3 The Experiment **27**

3.1 The LEP Storage Ring 27

3.2 The OPAL Detector 28

3.3 Physics Processes at LEP2 32

3.3.1 Two–Photon–Processes 32

3.3.2 Two–Fermion–Processes 33

3.3.3 Four–Fermion–Processes 34

3.4 Simulation of Events 35

4 The Event Reconstruction **39**

4.1 Reconstruction of Event Kinematics 39

4.1.1 Reconstruction of Particle Energies and Momenta 39

4.1.2 Jet–Reconstruction 40

4.1.3 Kinematic Fits 40

4.2 Identification of b–Quarks 42

4.2.1 The Lifetime Likelihood $\mathcal{L}_{lt}$ 42

4.2.2 The Lepton Likelihood $\mathcal{L}_{p_t}$ 43

4.2.3 The Jet–Kinematic Likelihood $\mathcal{L}_{kin}$ 43

4.2.4 The Combined b–Likelihood $\mathcal{B}$ 44

5 The Selections **47**
5.1 Data Set and Monte Carlo Samples 47
5.1.1 The Data Set 47
5.1.2 Signal Monte Carlo Samples 47
5.1.3 Standard Model Background Monte Carlo Samples 48
5.2 Preselection 50
5.3 The Likelihood Method 54
5.4 Search in the $e^+e^- \to \rho_T^0/\omega_T \to \pi_T^+\pi_T^-$ Channel 56
5.4.1 Likelihood Selection 57
5.4.2 Systematic Uncertainties 62
5.5 Search in the $e^+e^- \to \rho_T^0/\omega_T \to \pi_T^\pm W_L^\mp$ Channel 67
5.5.1 Jet Pairing 68
5.5.2 Likelihood Selection 69
5.5.3 Systematic Uncertainties 74

6 Interpretation of Results **77**
6.1 Limit Calculation 77
6.1.1 Confidence Levels 77
6.1.2 Combining Search Channels, Test Statistic 79
6.1.3 Expected Exclusion Limit 80
6.1.4 Handling of Systematic Uncertainties 81
6.2 Exclusion Limits 81

7 Summary **87**

Chapter 1

Introduction

The aim of elementary particle physics is to identify and explain the constituents and forces of the world surrounding us. After years of struggling to integrate all experimental facts into one consistent framework of theories which could explain well known and predict new outcomes of experiments, the basis of the Standard Model (SM) of particle physics was put forward by Glashow, Weinberg and Salam in 1967/68, thereby unifying the electro–magnetic and the weak force. By the time 't Hooft proved the renormalisability of the Standard Model in 1971, i.e. that no divergences would spoil its predictive power, it was fully elaborated.

The Standard Model describes the world as consisting of fundamental matter particles and includes three of the four known forces of Nature which are responsible for their interactions. The gravitational force is not included in the SM since it is very weak at distances resp. energies accessible at current particle physics experiments. The point–like matter particles are divided into three families of leptons (e , ν_e) (μ , ν_μ) (τ , ν_τ), three families of quarks (u , d) (c , s) (t , b), and their anti–particles. All these particles are fermions with spin $\frac{1}{2}$.

The three forces considered in the Standard Model are the electro–magnetic, the weak and the strong interaction. They are mediated by gauge bosons of spin 1. The exchange particle of the electro–magnetic (EM) interaction is the photon γ. It is massless, reflecting the infinite range of the electro–magnetic interaction. The photon couples to all matter particles carrying electric charge. The weak interaction is mediated by the charged weak gauge bosons W^+ and W^-, and the neutral Z. The very small range of the weak interaction requires the gauge bosons to be massive: the measured masses are approximately 80.2 GeV for the $W^\pm$ and 91.1 GeV for the Z. All matter particles interact through the weak interaction. The charge of the strong interaction is colour, only carried by quarks. Colour can occur in three states referred to as red, green, and blue. Eight massless gluons mediate the strong interaction between quarks. Heavier particles like mesons and baryons are composed of quarks bound together by the strong interaction.

On the way to the Standard Model the existence of massive weak gauge bosons was one of the problems which was difficult to overcome. Lagrangians of realistic field theories have to be globally invariant under the symmetry transformations of the Lorenz group, ensuring the correct behaviour with respect to special relativity. The existence of interactions is explained by postulating that the free Lagrangian should also be invariant under local transformations of one or more internal symmetry groups. On one hand this ensures the

renormalisability of the theory, on the other hand it forbids the introduction of mass terms for gauge fields into the Lagrangian. To integrate the observation of massive weak gauge bosons with locally gauge invariant theories, Higgs and others employed the mechanism of spontaneous symmetry breaking for particle physics in 1964. Higgs postulated additional scalar fields which have to be included in the Lagrangian of the theory, causing the weak gauge bosons to gain an effective mass through their interaction with these fields, but also predicting at least one new scalar spin–0 particle, the so called Higgs boson. Since then the search for the Higgs boson is one of the most pressing topics in high energy physics. To date, no Higgs boson has been observed [1].

The introduction of fundamental scalar fields make some physicists feel uneasy, since all other fundamental fields in the Standard Model's free Lagrangian are fermion fields. But, apart from this, also intrinsic shortcomings of the SM including scalar fields arise. It is widely accepted that the SM can not be the "theory of everything". At least at the Planck scale of $\mathcal{O}(10^{19}\,\mathrm{GeV})$ the Standard Model must break down, since there the gravitational force can no longer be neglected. Why two fundamental scales, the scale of electro–weak symmetry breaking ($\mathcal{O}(100\,\mathrm{GeV})$) and the Planck scale, should exist at so vastly different energies can not be understood within the Standard Model. This is the so called "hierarchy problem" of the Standard Model. Radiative corrections tend to pull the Higgs mass up to the order of the Planck mass. If there is a light Higgs boson, as suggested by electro–weak precision measurements and required to cancel divergencies in the production cross–section for massive gauge boson pairs, these radiative corrections must be cancelled out to an unphysically high precision in order to keep the Higgs boson light. This is the "finetuning problem".

In order to tackle these problems, the idea of Dynamical Electro–Weak Symmetry Breaking, also known as Technicolor[1], was put forward by Weinberg, Susskind and others in the 1970s. A new Technicolor interaction is postulated to act on a set of additional fermions, carrying a Technicolor charge. The Technicolor interaction is constructed in analogy to the strong interaction, copying its important features. Hence these new fermions are named "techniquarks". The concept of Dynamical Electro–Weak Symmetry Breaking opens the possibility for an alternative mechanism to generate particle masses, avoiding the difficulties related to the introduction of scalar fields. In Technicolor theories the scalar Higgs sector of the Standard Model is replaced by a condensate of techniquarks in the theory's vacuum state and no fundamental scalar field is needed anymore to break electro–weak symmetry. Hence no finetuning problem, which is connected to scalar fields, can arise.

The idea of Technicolor looked very promising in the beginning, since it seemed to solve most of the problems of the Standard Model in an elegant and consistent way. However, constructing a phenomenological model in agreement with precision measurements turned out to be difficult. Various extensions have been worked out to describe these observations, but thereby giving up the simple structure and predictive power of the basic Technicolor ideas. Calculations within these advanced models are difficult since perturbative approaches are only valid to a limited extent. In order to allow experimental physicists to search for possible Technicolor production at todays particle colliders, an effective low–energy model of Technicolor has been developed. This so called "Techni-

[1] Although this thesis is written in British English, the American way of writing "Technicolor" is the widely accepted standard. Therefore "Technicolor" is spelled the American way throughout this thesis.

color Straw Man Model" makes testable predictions for the lowest–lying states of a more complete Technicolor particle spectrum and is the basis for the analysis presented here.

Other extensions to the Standard Model have also been developed. Supersymmetric extensions postulate the existence of supersymmetric partners for each Standard Model particle. They thereby also solve the finetuning problem and make various other testable predictions. Lately the existence of extra space dimensions has been suggested as another alternative to circumvent the hierarchy problem. However, to date no unique hint of the realisation of any of the models in Nature has been found, leaving questions of how particles gain their masses unanswered.

In this thesis, a search for Technicolor particles within the framework of the Technicolor Straw Man Model is described. The search is carried out using the data of the OPAL detector at the electron–positron collider LEP. The considered search channels are $e^+e^- \to \rho_T^0/\omega_T \to \pi_T^+\pi_T^- \to b\bar{q}\bar{b}q'$ and $e^+e^- \to \rho_T^0/\omega_T \to \pi_T^+ W_L^- \to \bar{b}q\bar{q'}q''$.

Other collaborations have searched for Technicolor production as well. Resent results have been published by the DELPHI collaboration, based on data taken in the years 1999 and 2000 [2]. Also L3 has presented preliminary results [3]. Results on the search for Technicolor production at hadron colliders have been published by each of the two Tevatron experiments D0 [4] and CDF [5,6].

This thesis is structured as follows. In Chapter 2 a brief introduction to the Standard Model with special emphasis on the mechanism of spontaneous symmetry breaking is presented. The basic ideas of Technicolor theories are explained and the chapter closes with a more detailed description of the Technicolor Straw Man Model which provides the theoretical framework for this analysis. Chapter 3 describes the OPAL detector and the most important Standard Model physics processes occurring as background for the search for Technicolor production. In Chapter 4 the reconstruction of events is explained. Techniques for jet–finding and b–quark identification are of special interest, since they are important tools for this analysis. The search for Technicolor production in two different search channels is described in Chapter 5. One of the channels is sensitive to a four–quark final state involving two b–quarks. This search channel might be sensitive to all kinds of mass generating mechanisms, coupling to final state quarks with a strength proportional to the final state fermion masses. Therefore it might also be of interest for other searches outside the framework of Technicolor. In Chapter 6 the obtained results are interpreted within the Technicolor Straw Man Model and cross–section times branching ratio limits are calculated for each process under consideration. The details of how limits are obtained at a certain confidence level are explained. Chapter 7 summarises the results of the work presented in this thesis.

Chapter 2

Theory

In this chapter some details of the Standard Model (SM) [7–9] are discussed, particularly the description in terms of local gauge theories and the mechanism which generates the particle masses. For more detailed descriptions of the SM see e.g. [10, 11]. Some shortcomings of the SM are pointed out [12] to motivate the consideration of alternative theories such as Technicolor [7–9, 12, 13]. The chapter closes with a more detailed description of a special implementation of Technicolor theories, the Technicolor Straw Man Model [14–16], which is the theoretical basis for the analysis presented here.

2.1 The Standard Model

2.1.1 The Electro–Weak Interaction

In 1957 it was discovered that the charged weak interaction is maximally parity violating, coupling only to left–handed fermions [17]. It was found that the charged weak currents only mediate transitions within each family of leptons, coupling with the same strength to the left–handed charged leptons and neutrinos. Also, no huge flavour changing neutral currents exist, excluding transitions between families mediated by the Z boson. These experimental observations led to ordering the matter particles of the SM into multiplets of the weak isospin I, see Table 2.1. I_3 denotes its third component. The weak hyper–charge Y is then introduced defined by $Q = I_3 + Y/2$ such that it has the same value for the members of a multiplet. Q denotes the electric charge.

In order to allow the $W^{\pm}$ bosons to mediate transitions between the left–handed up and down type leptons by changing the third component of the weak isospin, a weak isospin of 1 is assigned to them. Since the Z does not mediate transitions between any different flavours, it is assigned a weak isospin of 0. This way of ordering the particles expresses the invariance of the weak force under rotations in the weak isospin space, describing neatly all the experimental facts mentioned above. For quarks, the charged weak currents can mediate transitions between the three families but the mixing is small. This fact is taken care of by defining the down type quark (I_3=-1/2) electro–weak (EW) eigenstates as an admixture of the three down type quark mass eigenstates. The transition between these

	leptons	I_3	Q	Y	quarks	I_3	Q	Y
doublet	$\begin{pmatrix}\nu_e\\ e\end{pmatrix}_L \begin{pmatrix}\nu_\mu\\ \mu\end{pmatrix}_L \begin{pmatrix}\nu_\tau\\ \tau\end{pmatrix}_L$	$1/2$ $-1/2$	0 -1	-1 -1	$\begin{pmatrix}u\\ d'\end{pmatrix}_L \begin{pmatrix}c\\ s'\end{pmatrix}_L \begin{pmatrix}t\\ b'\end{pmatrix}_L$	$1/2$ $-1/2$	$2/3$ $-1/3$	$1/3$ $1/3$
singlet					$u_R \quad c_R \quad t_R$	0	2/3	4/3
singlet	$e_R \quad \mu_R \quad \tau_R$	0	-1	-2	$d'_R \quad s'_R \quad b'_R$	0	-1/3	-2/3

Table 2.1: *The electro–weak eigenstates of the matter particles and their quantum numbers.*

eigenstates is described by the 3×3 CKM matrix, whose off–diagonal elements are small:

$$\begin{pmatrix} d' \\ s' \\ b' \end{pmatrix} = \begin{pmatrix} V_{ud} & V_{us} & V_{ub} \\ V_{cd} & V_{cs} & V_{cb} \\ V_{td} & V_{ts} & V_{tb} \end{pmatrix}_{CKM} \begin{pmatrix} d \\ s \\ b \end{pmatrix}$$

V_{ij} is proportional to the coupling at the quark–$W^{\pm}$–vertex, describing the transition from quark i to j.

In field theories, interactions of particles are described by postulating the invariance of the particles' free Lagrangian under local phase transformations of one or more internal symmetry groups. In Quantum Electro Dynamics (QED), describing the electro–magnetic interaction, the requirement that the free QED Lagrangian should be invariant under local phase transformations can only be fulfilled when a new gauge field is introduced. This can subsequently be identified with the observed electro–magnetic field. Phase transformations are represented by the group U(1) and have one free parameter, the phase transformation angle. Generally, for each free parameter of a group a new gauge field arises when requiring the local invariance of the Lagrangian under the transformations of the group.

Of special interest for particle physics are the special unitary groups SU(n) of dimension n. They have $n^2 - 1$ free parameters [11, ch. 1.2.1]. The non–abelian group SU(2) describes particles which carry weak isospin. It has three free parameters and thus three gauge fields need to be introduced when requiring local gauge invariance for the free Lagrangian. It was found that the electro–weak interactions could be described when requiring the free quantum flavour dynamic (QFD) Lagrangian

$$\mathcal{L}^{\text{free}}_{\text{QFD}} = i\bar{\text{L}}\gamma^\mu\partial_\mu\text{L} + i\bar{\text{R}}\gamma^\mu\partial_\mu\text{R}$$

to be invariant under the local gauge transformations of $\text{SU(2)}_\text{L} \times \text{U(1)}_\text{Y}$:

$$\begin{aligned} \text{L}' := \begin{pmatrix}\nu_e\\ e\end{pmatrix}'_\text{L} &= \exp\left(i\frac{g'}{2}Y_\text{L}\chi(x)\right) \times \exp\left(i\frac{g}{2}\sum_{i=1}^{3}\tau_i\beta_i(x)\right)\begin{pmatrix}\nu_e\\ e\end{pmatrix}_\text{L} \\ \text{R}' := {e_\text{R}}' &= \exp\left(i\frac{g'}{2}Y_\text{R}\chi(x)\right) e_\text{R}. \end{aligned}$$

Here only the electron – electron neutrino family is considered, but the transformations look the same for all families of fermions. g and g' are the two different coupling constants for SU(2)_L and U(1)_Y respectively. As can be seen from the locally invariant QFD Lagrangian below, Eq. 2.1, they describe the strength with which the required gauge

fields couple to the weak isospin resp. the weak hyper–charge. $\beta_i(x)$ and $\chi(x)$ are the space-time dependent transformation angles for $\mathrm{SU(2)_L}$ and $\mathrm{U(1)_Y}$ and τ_i are the Pauli matrices, being a representation of the SU(2) group in two dimensions. Mass terms, like $m(\bar{R}L + \bar{L}R)$, for the fermions are not allowed in the free QFD Lagrangian since the different transformation properties of L and R would spoil its global invariance under $\mathrm{SU(2)_L \times U(1)_Y}$.

When requiring the free QFD Lagrangian to be *locally* invariant under $\mathrm{SU(2)_L \times U(1)_Y}$ transformations, four gauge fields have to be introduced: one (B_μ) to compensate for the local phase transformation of the $\mathrm{U(1)_Y}$ group and three more ($\mathrm{W}^{\mathrm{a}}_\mu, \mathrm{a} = 1,2,3$) related to the transformations of $\mathrm{SU(2)_L}$. The locally invariant QFD Lagrangian is

$$\begin{aligned}\mathcal{L}_{\mathrm{QFD}} = i\bar{\mathrm{L}}\gamma^\mu\partial_\mu\mathrm{L} + i\bar{\mathrm{R}}\gamma^\mu\partial_\mu\mathrm{R} - \frac{1}{4}\mathrm{B}^{\mu\nu}\mathrm{B}_{\mu\nu} - \frac{1}{4}\vec{\mathrm{W}}^{\mu\nu}\vec{\mathrm{W}}_{\mu\nu} + \\ \bar{\mathrm{L}}\gamma^\mu g'\frac{Y_\mathrm{L}}{2}\mathrm{B}_\mu\mathrm{L} + \bar{\mathrm{R}}\gamma^\mu g'\frac{Y_\mathrm{R}}{2}\mathrm{B}_\mu\mathrm{L} + \bar{\mathrm{L}}\gamma^\mu g\frac{1}{2}\vec{\tau}\vec{\mathrm{W}}_\mu\mathrm{L}\end{aligned} \tag{2.1}$$

with the field tensors $\mathrm{B}_{\mu\nu} = \partial_\mu\mathrm{B}_\nu - \partial_\nu\mathrm{B}_\mu$ and $\vec{\mathrm{W}}_{\mu\nu} = \partial_\mu\vec{\mathrm{W}}_\nu - \partial_\nu\vec{\mathrm{W}}_\mu + ig\vec{\mathrm{W}}_\mu \times \vec{\mathrm{W}}_\nu$. The terms in the first line describe the kinetic energy of the fermions and the gauge fields. The last term also contains self–interactions of the SU(2) gauge fields W^a_μ, a feature common for non–abelian gauge groups. The second line describes interactions between the fermions and gauge fields.

The introduced gauge fields B_μ, W^a_μ can not be identified directly with the experimentally observed gauge bosons γ and $\mathrm{W}^\pm$, Z because Eq. 2.1 would describe a coupling of the neutrino to the photon (first term in second line). The last term lets all three weak gauge bosons mediate transitions within one left–handed family. These two features contradict observation. To describe the gauge boson fields realised in nature, the following combinations have to be constructed

$$\begin{aligned}\mathrm{W}^\pm_\mu &= \frac{1}{\sqrt{2}}(\mathrm{W}^1_\mu \mp i\mathrm{W}^2_\mu) \\ \mathrm{Z}^\mu &= -\mathrm{B}^\mu\sin\theta_W + \mathrm{W}^\mu_3\cos\theta_W \\ \mathrm{A}^\mu &= \ \ \mathrm{B}^\mu\cos\theta_W + \mathrm{W}^\mu_3\sin\theta_W\end{aligned} \tag{2.2}$$

where the Weinberg angle θ_W is determined by

$$\cos\theta_W = \frac{g}{\sqrt{g^2 + g'^2}}.$$

The coupling constants g and g' are related to the electric charge by

$$\mathrm{e} = g'\cos\theta_W = g\sin\theta_W.$$

When inserting the fields Eq. 2.2 into Eq. 2.1 the QFD Lagrangian with respect to the observed fields is obtained. Still all fermion and gauge fields are massless. Mass terms will be introduced by the Higgs mechanism described in section 2.1.3.

2.1.2 The Strong Interaction

Through the invention of the static quark model [18] one was able to order all the detected mesons and baryons into multiplets of quark flavour, assuming that mesons are

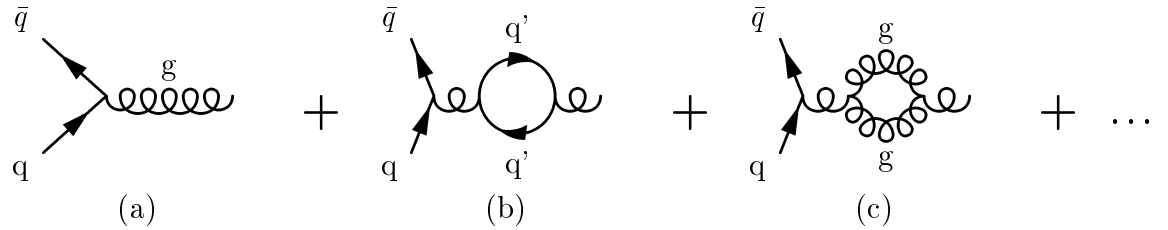

Figure 2.1: *(a) the quark–gluon vertex, (b) the quark loop, and (c) the gluon loop which modify the gluon propagator and hence renormalise the colour coupling.*

built out of two and baryons of three quarks. For some baryons the total wave function of its constituent quarks was symmetric when exchanging any two quarks. This is a central feature of bosons. In contradiction, the baryon's spin was measured to be $\frac{1}{2}$. This seemed to violate Pauli's principle. To preserve this fundamental principle, a new quantum number, colour, was introduced. Colour appears in three states, commonly referred to as red, green and blue.

It is then postulated that all hadrons are colour singlets. As can be shown, the nuclear force acting between hadrons would otherwise have a component of infinite range. This contradicts observation. Mesons are assumed to consist of a quark–antiquark pair, one quark carrying colour and the other one its anti-colour. Baryons are constructed out of three quarks, each one carrying a different colour so the whole object is colourless. Beside these valence quarks, hadrons further consist of gluons and so called sea quarks, being constantly created and annihilated through vacuum polarisation.

The strong interaction does not distinguish between the three colours, it is invariant under rotations in the three–dimensional colour space. Following the arguments from the previous section, the strong force can be described by requiring the quark's free Lagrangian to be locally invariant under $\mathrm{SU}(3)_C$ gauge transformations

$$\Psi' = \exp\left(i\frac{g_s}{2}\sum_{i=1}^{8}\lambda_i\epsilon_i(x)\right)\Psi.$$

Here λ_i are the eight generators of the group SU(3), $\epsilon_i(x)$ the corresponding free transformation angles and g_s is the strong coupling constant. Ψ represents a quark colour triplet:

$$\Psi = \begin{pmatrix} \mathrm{q}_{\mathrm{red}} \\ \mathrm{q}_{\mathrm{green}} \\ \mathrm{q}_{\mathrm{blue}} \end{pmatrix}.$$

Local gauge invariance can only be assured when introducing $3^2 - 1 = 8$ new gauge fields into the QCD Lagrangian. They describe the eight exchange bosons of the strong interaction, the gluons. They themselves carry colour giving rise to gluon self–interactions. These are the reason for two central features of the strong interaction: asymptotic freedom and confinement.

The parameter which describes the strength of the electro–magnetic interaction in perturbative QED is the fine structure constant $\alpha = e^2/(4\pi)$. If $\alpha \ll 1$ perturbative calculations are valid. Similarly, the strength of the strong interaction is described by $\alpha_s = g_s^2/(4\pi)$. In Figure 2.1 (a) the Feynman diagram of the quark–gluon vertex is shown. Vacuum polarisations can introduce one or more virtual quark loops in the gluon

propagator (b). When adding up all these contributions to the vertex, perturbative calculations produce unphysically infinite results. Therefore the procedure of renormalisation has to be applied to the theory, removing these infinities but resulting in energy depending coupling constants and masses.

Virtual charged fermion loops can also occur in the photon propagator. The resulting energy dependence of α is normally expressed in terms of the momentum transfer Q^2 or a probing distance r, where large r correspond to small momentum transfer. It is found that α increases with increasing Q^2 resp. decreasing r. This behaviour can be qualitatively understood: vacuum fluctuations described by QED constantly create and annihilate virtual electron–positron pairs around an electric charge. They act as an effective dielectricum, shielding the charge from a charge sensitive probe. When decreasing the distance between the charge and the probe, fewer and fewer electron–positron pairs lie between them, hence the shielding effect decreases.

In QCD a second effect is overlayed. The self–interactions of gluons give rise to additional gluon loops in the gluon propagator (Figure 2.1 (c)). These are the reason why, by summing up the contributions of the two processes, α_s is found to decrease with increasing Q^2. As a function of the distance r involved in the process, α_s is given by [19, ch. 1]

$$\alpha_s \approx \frac{1}{\frac{b_0}{2\pi}\log\left(\frac{\hbar c}{\Lambda_C r}\right)}. \tag{2.3}$$

b_0 is a positive constant depending on the number of colours and flavours. Λ_C is a QCD parameter, describing the hadronic energy scale. From Eq. 2.3 follows $\alpha_s \to 0$ as $r \to 0$, giving rise to *asymptotic freedom*. This describes the fact that quarks and gluons inside hadrons behave like free particles at short distances resp. high energies.

On the other hand α_s diverges as $r \to R_C \equiv \hbar c/\Lambda_C$. This behaviour indicates the breakdown of perturbative calculations at this distance and suggests that the strong force between quarks will increase when pulled apart. As a result, quarks and gluons are *confined* in hadrons whose typical size is of order $R_C \approx 1\,\mathrm{fm}$.

The energy scale of the strong interaction Λ_C can be measured by measuring α_s and is found to be [19, ch. 1]

$$\Lambda_C \approx 200 - 300\,\mathrm{MeV}. \tag{2.4}$$

2.1.3 Spontaneous Symmetry Breaking

The observation of massive weak gauge bosons implies that the local $\mathrm{SU(2)_L} \times \mathrm{U(1)}_Y$ symmetry of the QFD Lagrangian (Eq. 2.1) is not realised in nature, i.e. it is not a symmetry of the universe's vacuum state. On the other hand the photon is observed to be massless, hence the universe's vacuum state should still be invariant under $\mathrm{U(1)_{EM}}$.

The only known way of accomplishing the task of breaking $\mathrm{SU(2)_L} \times \mathrm{U(1)}_Y$ down to $\mathrm{U(1)_{EM}}$ while maintaining the initial gauge invariance of the Lagrangian, is by the formalism of spontaneous symmetry breaking (SSB). A symmetry is said to be spontaneously broken if the theory's Lagrangian is invariant under this symmetry but its vacuum state is not.

A phenomenon closely related to spontaneous symmetry breaking is the appearance of massless bosons. These are named Goldstone bosons after Goldstone's theorem [20].

It states that for each broken generator of a symmetry group one massless spin–0 boson appears. These Goldstone bosons play a crucial role in giving masses to the weak gauge bosons.

The spontaneous symmetry breaking is induced by a scalar field which has a non–vanishing vacuum expectation value (vev). This scalar field can either be fundamental or composite. In the following, two examples of SSB will be looked at. The Higgs mechanism describes the $\mathrm{SU(2)_L \times U(1)_Y \to U(1)_{EM}}$ breaking in the Standard Model by introducing fundamental scalar fields. Chiral symmetry breaking in QCD is considered as an example for dynamical symmetry breaking, where the scalar particle is composite. It is closely related to the way Technicolor breaks electro–weak symmetry.

The Higgs Mechanism

The Higgs mechanism [21–23] of the Standard Model realises the $\mathrm{SU(2)_L \times U(1)_Y \to U(1)_{EM}}$ symmetry breaking by introducing an electro–weak doublet Φ of elementary complex scalar fields into the free QFD Lagrangian. They interact through a suitable potential $\mathrm{V}(\Phi)$ which is responsible for the non–vanishing vev of the Higgs field.

The simplest representation of such an EW doublet which is able to break the EW symmetry is assumed in the Standard Model:

$$\Phi = \begin{pmatrix} \Phi^+ \\ \Phi^0 \end{pmatrix} = \begin{pmatrix} \Phi_1 + i\Phi_2 \\ \Phi_3 + i\Phi_4 \end{pmatrix}, \text{where } \Phi_\mathrm{i} \text{ real.} \tag{2.5}$$

When claiming local gauge invariance under $\mathrm{SU(2)_L \times U(1)_Y}$, the following term must be added to Eq. 2.1:

$$\mathcal{L}_\mathrm{Higgs} = (\mathrm{D}_\mu\Phi)^\dagger(\mathrm{D}^\mu\Phi) - \mathrm{V}(\Phi), \quad \text{where} \tag{2.6}$$

$$\mathrm{V}(\Phi,\Phi^\dagger) = -\mu^2\Phi^\dagger\Phi + \lambda^2(\Phi^\dagger\Phi)^2 \quad \text{with} \quad \mu,\lambda > 0 \quad \text{and} \tag{2.7}$$

$$\mathrm{D}_\mu = (\partial_\mu - \frac{1}{2}ig\vec{\tau}\vec{W}_\mu - \frac{1}{2}ig'YB_\mu) \tag{2.8}$$

Mass terms for fermions must be placed into the Lagrangian by hand. These so called Yukawa terms couple the fermions to the Higgs field:

$$\mathcal{L}_\mathrm{Yukawa} = -\lambda_\mathrm{f}\left[\bar{\mathrm{R}}(\Phi^\dagger\mathrm{L}) + (\bar{\mathrm{L}}\Phi)\mathrm{R}\right], \tag{2.9}$$

where λ_f is the Yukawa coupling constant for fermion f.

The Higgs potential Eq. 2.7 is shown in Figure 2.2 as a function of two of its four degrees of freedom. The minima of this potential are possible vacuum states. In order to have the theory describe nature, a single definite stable vacuum state has to be chosen. Different vacuum states correspond to different worlds and it can be shown [11, ch. 3.2.2] that transitions between different vacua are impossible. Nevertheless, the choice of the vacuum state is irrelevant and normally

$$\Phi_1 = 0, \qquad \Phi_2 = 0, \qquad \Phi_3 = v, \qquad \Phi_4 = 0 \tag{2.10}$$

is chosen. This choice gives the neutral component of the Higgs field Eq. 2.5 a non–vanishing vacuum expectation value

$$v = \frac{\mu}{\lambda} \neq 0.$$

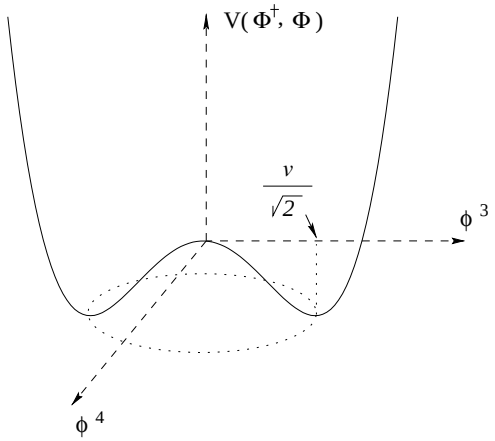

Figure 2.2: *The Higgs potential* $\mathrm{V}(\Phi, \Phi^\dagger)$ *as a function of two of its four degrees of freedom.*

By choosing a vacuum state the initial $\mathrm{SU(2)_L \times U(1)_Y}$ symmetry is spontaneously broken, as will be shown in the following.

In order to evaluate the physical spectrum, the EW Lagrangian has to be evaluated in the vicinity of its vacuum. The Higgs doublet Eq. 2.5 is replaced by

$$\Phi \rightarrow \Phi' = \frac{1}{\sqrt{2}} \begin{pmatrix} 0 \\ v + \eta \end{pmatrix} \tag{2.11}$$

where η describes the expansion of the Higgs potential along its Φ_3 component with respect to the vacuum state. Fields along the other three axes are suppressed in Eq. 2.11, since they do not lead to physical particles. When inserting Eq. 2.11 into Eq. 2.9 and Eq. 2.6, mass terms for fermions and weak gauge bosons show up. The Lagrangian is no longer invariant under $\mathrm{SU(2)_L}$ transformations. All masses are proportional to the vev and given by

$$m_f = \frac{\lambda_\mathrm{f}}{\sqrt{2}} v \tag{2.12}$$

$$m_\mathrm{W} = \frac{g}{2} v \tag{2.13}$$

$$m_\mathrm{Z} = \frac{g}{2\cos\theta_W} v = \frac{m_\mathrm{W}}{\cos\theta_W} \tag{2.14}$$

η represents a scalar spin–0 boson, the Higgs particle. It gains a mass of

$$m_\mathrm{H} = \sqrt{2}\mu.$$

The vev is related to the experimentally accessible Fermi constant G_F by

$$\frac{G_F}{2} = \frac{g^2}{8 m_\mathrm{W}^2} = \frac{1}{2v^2}. \tag{2.15}$$

This results in a value of

$$v = (\sqrt{2} G_F)^{-\frac{1}{2}} \approx 246\,\mathrm{GeV}. \tag{2.16}$$

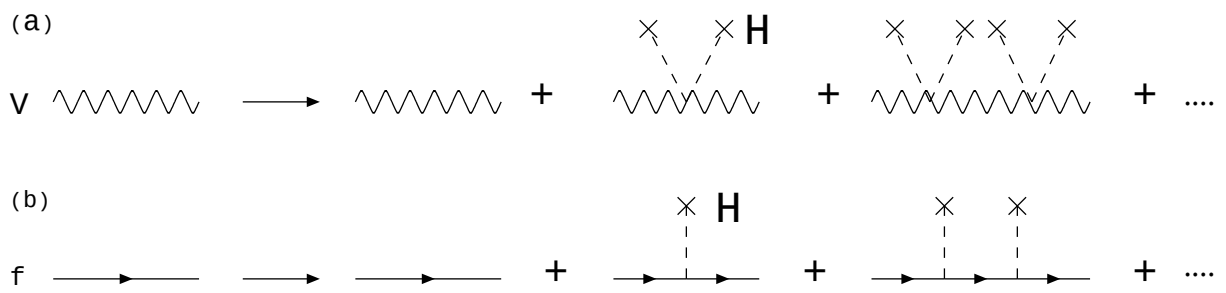

Figure 2.3: *Generating (a) gauge boson and (b) fermion masses through interactions with the vev of the Higgs field H. Figure taken from [24]; more details can be found therein.*

The interaction terms in the full QFD Lagrangian describing the Higgs field interaction with weak gauge bosons and fermions are shown as Feynman diagrams in Figure 2.3, depicting how mass is generated by interactions with the Higgs field [24].

The three Goldstone bosons which appear in the process of breaking $\mathrm{SU(2)_L \times U(1)}_Y$ down to $\mathrm{U(1)_{EM}}$ have not been mentioned so far. They are represented by the three fields suppressed in Eq. 2.11, describing the expansion of the Higgs potential with respect to the vacuum along the remaining three axes. Their three degrees of freedom are transformed into the three longitudinal polarisation states of the $\mathrm{W}^{\pm}$ and Z, which have to be present when they are massive.

Chiral Symmetry Breaking

Some experimentally verified results for strong interactions at low energy can be derived by considering only the lightest quarks, the u– and d–quark [19, ch. 3]. Their masses are small compared to the hadronic mass scale Λ_{C}, and so it is justified to consider the limit $m_{\mathrm{u,d}} \to 0$.

When neglecting the quark masses, the QCD Lagrangian becomes invariant under rotations in the U(2) flavour space. When writing the Lagrangian in terms of left– and right–handed chirality eigenstates of the quarks, q_{L} and q_{R}, this Lagrangian is invariant under independent rotations in the flavour space for left– and right–handed quarks separately:

$$q_{\mathrm{L}} \to \mathrm{U_L} q_{\mathrm{L}} \quad \text{and} \quad q_{\mathrm{R}} \to \mathrm{U_R} q_{\mathrm{R}}.$$

Since the limit assumed above is only approximate, especially for the s quark, the Lagrangian is said to have an approximate *chiral* $\mathrm{U(2)_V \times U(2)_A = SU(2)_V \times SU(2)_A \times U(1)_V \times U(1)_A}$ symmetry. Here the left– and right–handed chirality components, L and R, have been expressed through vector– and axial–vector components, V=R+L and A=R−L.

The $\mathrm{SU(2)_V \times U(1)_V}$ symmetries correspond to SU(2) flavour invariance and baryon number conservation. The latter is fully verified through experiment. Since SU(2) flavour multiplets are approximately degenerate in mass as predicted by this model, the assumption of vanishing quark masses seems to be appropriate.

The conditions for $\mathrm{SU(2)_V}$ symmetry to hold are identical to those needed for the validity of the full chiral symmetry, i.e. small quark masses compared to Λ_{C}. Hence one would expect hadron physics to manifest full chiral symmetry to the same degree as it does for $\mathrm{SU(2)_V}$. However, this would require hadrons to be either massless or to appear in

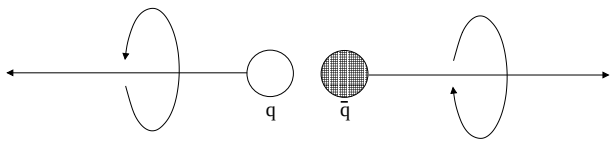

Figure 2.4: *A quark–antiquark pair with zero total momentum and angular momentum.*

parity doublets, since only in these cases chirally invariant mass terms can be formed. The observed hadron spectrum contradicts this prediction. For example there is no particle with spin–parity $\frac{1}{2}^-$ which is even approximately degenerate in mass with the proton, which has spin–parity $\frac{1}{2}^+$.

Chiral $\mathrm{SU}(2)_\mathrm{L} \times \mathrm{SU}(2)_\mathrm{R}$ symmetry must be broken down to $\mathrm{SU}(2)_\mathrm{V}$ [25]. This can be accomplished, as seen in the previous section, by introducing a scalar field which initiates the symmetry breaking. Here the introduction of a new scalar field is circumvented by requiring the QCD Lagrangian to produce scalar quark condensates, $(q\bar{q})$, which acquire non–zero vacuum expectation values. This assumption can be qualitatively understood by comparison with the theory of super–conductivity [26]. Here a small force between the electrons leads to the formation of Cooper pairs in the ground state of the supra-conductor. The electrons form a condensate.

In QCD a strong attractive force exists between the quarks and the energy cost of creating a new quark– antiquark pair out of the vacuum is small due to the small quark masses. Hence it is justified to assume a condensate of quarks as the QCD ground state [27, ch. 19]. The total momentum and angular momentum of this condensate must vanish and therefore chirality pairs have to be formed, see Figure 2.4. The vacuum state is thus characterised by a non–zero vacuum expectation value of the scalar operator

$$\langle 0|\bar{q}q|0\rangle = \langle 0|\bar{q}_\mathrm{L} q_\mathrm{R} + \bar{q}_\mathrm{R} q_\mathrm{L}|0\rangle \neq 0. \tag{2.17}$$

The three Goldstone bosons which appear in the process of $\mathrm{SU}(2)_\mathrm{L} \times \mathrm{SU}(2)_\mathrm{R} \to \mathrm{SU}(2)_\mathrm{V}$ symmetry breaking can be identified with the pions $\pi^{\pm,0}$. Since the broken symmetry holds only approximately, the Goldstones are only approximately massless. This explains the observed masses of the pions.

The decay of the pion as a Goldstone boson can also be described in this model. To parametrise the charged pion's coupling to $\mathrm{W}^\pm$, the pion decay constant f_π is introduced. By measuring the width of the pion decay process $\pi \to \mu\nu_\mu$ (see Figure 2.5), it is

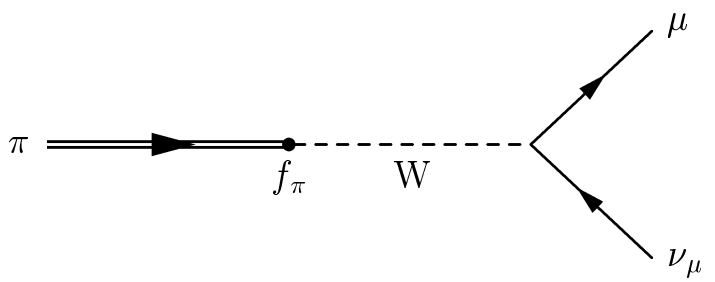

Figure 2.5: *The Feynman diagram describing the $\pi^\pm \to \mu^\pm\nu$ decay. The pion decay constant f_π parametrises the coupling of the W to the π.*

determined to [19, ch. 3]

$$f_\pi = 93\,\mathrm{MeV}. \tag{2.18}$$

2.2 Technicolor

In this chapter Technicolor models are discussed. In the first part shortcomings of the Standard Model are highlighted to motivate the search for alternative models such as Technicolor.

2.2.1 Why Technicolor ?

Although the Standard Model has been tested up to very high precision, the origin of electro–weak symmetry breaking has still not been revealed. To date no Higgs particle has been found [1] and this is the main motivation for an experimental physicist to search for particles predicted by various alternative models. Apart from these experimental considerations, the Standard Model itself has shortcomings which are related to the elementary scalar Higgs sector [12]. Some of these will be discussed below and in the next chapter it will be shown how Technicolor tackles them.

To begin with, the Standard Model can not explain *why* spontaneous symmetry breaking occurs and why it does so at an energy scale of $\mathcal{O}(10^2\,\mathrm{GeV})$. It is not deducible within the Standard Model why the vev of the Higgs potential is non–vanishing. Also there is no explanation for the wide range of lepton and quark masses, since the Yukawa couplings (see Eq. 2.12) are free parameters of the Standard Model.

Secondly, loop diagrams as shown in Figure 2.6 give quadratically divergent corrections to the Higgs mass of the form [19, ch. 8]

$$\delta \mathrm{M}_\mathrm{H}^2 \propto g^2 \int^\Lambda \frac{\mathrm{d}^4 k}{(2\pi)^4} \frac{1}{k^2} \approx g^2 \Lambda^2. \tag{2.19}$$

These divergences can only be removed when a finite cut–off energy scale Λ is introduced. At this energy scale some new physics must set in. Usually this cut–off is taken as the scale of grand unification, the GUT–scale $\Lambda_\mathrm{GUT} = \mathcal{O}(10^{15}\,\mathrm{GeV})$. Here all forces are assumed to be unified and can be described by requiring local gauge invariance under a larger symmetry group, which is spontaneously broken down to $\mathrm{SU}(3) \times \mathrm{SU}(2) \times \mathrm{U}(1)$ at $\sim \Lambda_\mathrm{GUT}$. Why spontaneous symmetry breaking should occur at such different energy scales is not clear and is normally referred to as the *hierarchy problem*, see e.g. [19, ch. 8]. In order to keep the two scales of spontaneous symmetry breaking so far apart, i.e. keeping the Standard Model Higgs boson light, cancellations of divergences as in Eq. 2.19 must be ensured to an enormous "unnatural" precision of $\sim 10^{-24}$. This is usually referred to as the *finetuning problem* or the *unnaturalness* of the Standard Model.

One possible solution for the finetuning problem is offered by supersymmetric (SUSY) theories, see e.g. [28–31]. Supersymmetric transformations mediate transitions between fermions and bosons. For each fermion a bosonic and for each boson a fermionic super–partner is introduced. These supersymmetric partners must also be taken into account when calculating renormalisation corrections for the Higgs mass, i.e. additional loops as in Figure 2.6 exist, where the particle in the loop is replaced by its superpartner. It

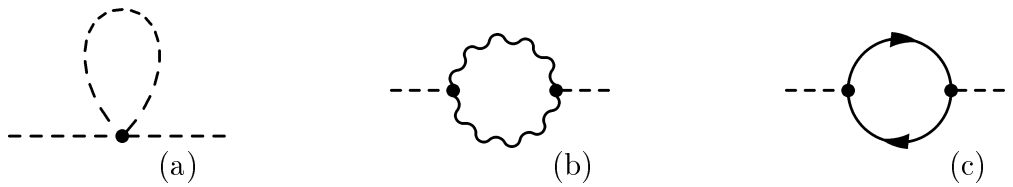

Figure 2.6: *Renormalisation corrections to the Higgs boson mass (a) the quartic Higgs self–coupling term, (b) the gauge boson loops and (c) fermion loops.*

turns out that these contributions exactly cancel the divergences term by term and so no unnatural finetuning of parameters is necessary.

The dynamical approach to electro–weak symmetry breaking and flavour symmetry breaking known as Technicolor [7–9] and Extended Technicolor [32, 33] emerged in the 1970s, also responding to the shortcomings of the Standard Model. This picture was motivated first of all by the premise that every fundamental energy scale should have a dynamical origin. In the same way as the QCD pion decay constant f_π reflects the dynamics of the strong interaction at the QCD scale Λ_{C}, the vacuum expectation value $v \approx 246\,\mathrm{GeV}$ should reflect the dynamics of a new strong interaction, Technicolor, at some higher scale Λ_{TC}. Since no fundamental scalar fields are necessary anymore to break electro–weak symmetry, the finetuning problem is solved naturally.

2.2.2 Technicolor (TC): Weak Gauge Boson Masses

It can be shown that the process of QCD chiral symmetry breaking (see 2.1.3) gives rise to mass terms in the propagators of the weak gauge bosons, but the resulting mass is much too small to explain the measured values. The basic idea of Technicolor is to construct a QCD like interaction between new technifermions, reproducing QCD's fundamental features such as confinement and asymptotic freedom. Essentially the same processes as in QCD will then lead to chiral symmetry breaking in the technifermion sector. The mass scale Λ_{TC} at which this spontaneous symmetry breaking occurs is assumed to be much larger than Λ_{C}, thereby reproducing the measured masses of the weak gauge bosons. For a review see e.g. [13].

In the simplest TC models, new massless technifermions F are introduced sitting in the fundamental representation of the Technicolor gauge group $\mathrm{SU}(N_{\mathrm{TC}})$. To avoid anomalies, the technifermions are assumed to transform under the electro–weak gauge group $\mathrm{SU(2)_L} \times \mathrm{U(1)_Y}$ just like ordinary quarks or leptons. Hence they are placed in electro–weak left–handed doublets and right–handed singlets:

$$F = \begin{pmatrix} U^i \\ D^i \end{pmatrix}_{\mathrm{L}}, \; U^i_R, \; D^i_R, \tag{2.20}$$

where $i = 1, \ldots, \mathrm{N_{TC}}$ is the Technicolor index.

If one neglected all non–Technicolor interactions and also non-perturbative effects, the theory of these massless fermions would have the global chiral flavour symmetry $\mathrm{SU(2)_L \times SU(2)_R \times U(1)_L \times U(1)_R}$. It is now assumed that the dynamics of the Technicolor interaction will cause the formation of scalar technifermion condensates $(F\bar{F})$ which, as in the QCD case, acquire non–vanishing vacuum expectation values

$$\langle 0|F\bar{F}|0\rangle \neq 0.$$

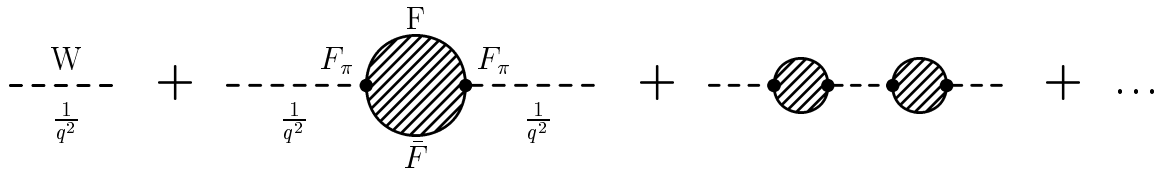

Figure 2.7: *Corrections to the* $\mathrm{W}^\pm$ *propagator due to the formation of* $(F\bar{F})$ *technifermion condensates.*

In QCD this spontaneous symmetry breaking leads to the appearance of Goldstone bosons, which can be identified as the normal pions. Accordingly, here also three Goldstone bosons $\Pi_T^\pm, \Pi_T^0$ arise. In analogy to the QCD case they are named technipions. These technipions can now appear as intermediate states in the massless $W^{\pm,0}$ propagator as shown in Figure 2.7. By summing up all the diagrams the full W propagator is obtained as the geometric series [19, ch. 8]

$$\frac{1}{q^2} + \frac{1}{q^2}\left(\frac{1}{2}gF_\pi\right)^2\frac{1}{q^2} + \frac{1}{q^2}\left(\frac{1}{2}gF_\pi\right)^2\frac{1}{q^2}\left(\frac{1}{2}gF_\pi\right)^2\frac{1}{q^2} + \cdots = \frac{1}{q^2 - \left(\frac{1}{2}gF_\pi\right)^2}.$$

F_π is the technipion decay constant which describes the coupling of the technipions to the charged weak gauge bosons in analogy to the pion decay constant f_π in QCD, cf. Eq. 2.21. When requiring the $W^\pm$ propagator to obtain a mass pole at the measured W boson mass, the following relation must hold:

$$\left(\frac{1}{2}gF_\pi\right)^2 = m_W^2 \qquad \Rightarrow \qquad F_\pi = 246\,\mathrm{GeV}. \tag{2.21}$$

The non–vanishing vev of the scalar Higgs potential is replaced by the non–vanishing vev of the techniquark condensate. The neutral W^0 field mixes with the $\mathrm{U(1)_Y}$ B field and, just as in the Standard Model, this breaks the SU(2) isospin symmetry and gives the relation Eq. 2.14 between the $\mathrm{W}^\pm$ and Z masses.

In the same way, the normal pions contribute to the W boson masses, but only with $\frac{1}{2}gf_\pi \approx 30\,\mathrm{MeV}$. This is why it is essential to introduce a much higher scale for the Technicolor theory. By naïve scaling from QCD the Technicolor scale can be estimated from

$$\frac{f_\pi}{\Lambda_\mathrm{C}} \approx \frac{F_\pi}{\Lambda_\mathrm{TC}}$$

to $\Lambda_\mathrm{TC} \approx 500\,\mathrm{GeV}$.

2.2.3 Extended Technicolor (ETC): Fermion Masses

The generation of fermion masses can not be accomplished in the same way as in the Standard Model. A Yukawa coupling term analogue to the one depicted in Figure 2.3 (b) would be of the four–fermion type, see Figure 2.8 (a). The coupling constant G_f is then of the dimension $(\mathrm{mass})^{-2}$, just as the Fermi constant G_F of the effective weak four–fermion interaction. Such theories are not renormalisable.

Therefore, new ETC gauge bosons have to be introduced coupling fermions to technifermions. These bosons are the gauge fields of some higher ETC symmetry group, in

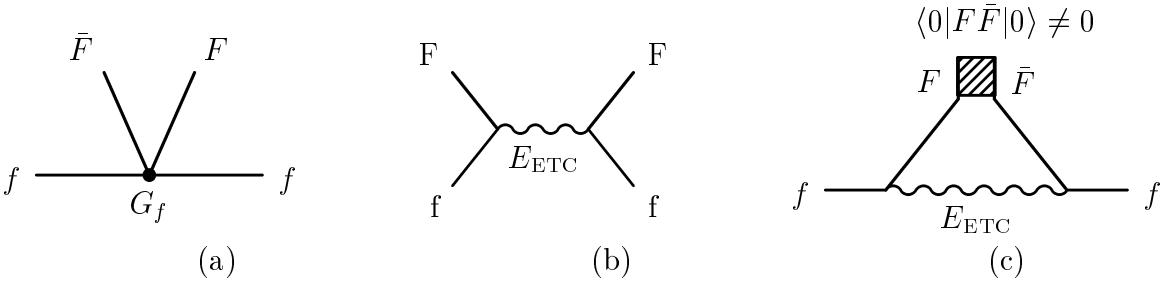

Figure 2.8: *(a) Not renormalisable four–fermion interaction; (b) The ETC gauge bosons couples fermions to technifermions; (c) Generation of fermion masses*

which the SU(N_{TC}) and the symmetry groups of the Standard Model are embedded. In principle scalar and vector particles are possible [19, ch. 8], but as the aim of Technicolor theories is to prevent the problems connected to scalar fields, the vector gauge boson option is chosen, see Figure 2.8 (b). The effective low–energy coupling corresponding to Eq. 2.15 is then [19, ch. 8]

$$G_f \propto \frac{g_{EfF}^2}{M_E^2}, \tag{2.22}$$

where M_E is the mass of the new gauge boson E and g_{EfF} the ETC coupling constant.

The simplest way of ensuring the full gauge group structure is for the technifermions to carry the same colour or lepton quantum numbers as ordinary quarks and leptons. Hence the family of technifermions is extended to include both, coloured techniquarks Q and technileptons L:

$$Q = \begin{pmatrix} U^{a,i} \\ D^{a,i} \end{pmatrix}_{\mathrm{L}},\ U_R^{a,i},\ D_R^{a,i}, \qquad L = \begin{pmatrix} M^i \\ N^i \end{pmatrix}_{\mathrm{L}},\ M_R^i,\ N_R^i. \tag{2.23}$$

Here $a = 1, \ldots, N_{\mathrm{TC}}$ is the Technicolor and $a = 1, 2, 3$ the normal colour index. Right–handed technineutrinos N_{R} are allowed and can obtain masses. The masses of ordinary fermions then arise through loop diagrams like Figure 2.8 (c). They can be estimated to [19, ch. 8]

$$m_f \approx \frac{g_{EfF}^2}{M_E^2}\langle 0|F\bar{F}|0\rangle \approx \frac{g_{EfF}^2}{M_E^2}\mathcal{O}(\Lambda_{\mathrm{TC}}^3) \tag{2.24}$$

The same diagram explains how technipions decay to Standard Model quarks and leptons. As these diagrams are responsible for the fermion masses, the technipions are expected to decay to the heaviest fermion pairs kinematically allowed.

The different mass scales for the three families of quarks could be explained through ETC gauge bosons of different masses. If the ETC group is spontaneously broken down to the Technicolor group in steps at different energy scales (i.e. it is "tumbling" down), different masses for the ETC gauge bosons could be generated:

$$G_{\mathrm{ETC}} \xrightarrow[M_{\mathrm{Ef_1F}}]{} G_{\mathrm{E'TC}} \xrightarrow[M_{\mathrm{Ef_2F}}]{} G_{\mathrm{E''TC}} \xrightarrow[M_{\mathrm{Ef_3F}}]{} G_{\mathrm{TC}}.$$

The breaking of the ETC group at $\Lambda_{\mathrm{ETC}} \approx 100$–$500\,\mathrm{TeV}$ is again assumed to be due to the formation of technifermion condensates. This time it is the ETC interactions which are responsible for the condensation.

2.2.4 Realistic Models

Technicolor and Extended Technicolor models are challenged by a number of phenomenological hurdles. The ETC interactions must also give rise to quark mixing. Hence one would expect ETC interactions to couple quarks of the same charge from different families. To prevent large contributions to these flavour–changing neutral currents (FCNC) the ETC scale must be in the multi TeV range.

Thus, to obtain then the measured quark masses, the technifermion condensate must be enhanced over that expected by naïvely scaling from QCD (see Eq. 2.24). Such an enhancement can occur if the Technicolor gauge coupling α_{TC} runs very slowly – or "walks" – over the large range of energy between Λ_{TC} and Λ_{ETC} [34–38]. This can be obtained when requiring many technifermion doublets, implying that the Technicolor scale and in particular the lightest technivectors may be much lighter than 1 TeV and therefore accessible at present colliders [12, 14, 16]. It should be noted that there is no reliable calculation of electro–weak parameters possible anymore and that therefore precisely measured electro–weak quantities can not directly be used to constrain these models. Also the spectrum of techniparticles will not be QCD–like anymore. For the spin–1 particles like ρ_T and ω_T one expects something like a tower of states extending up to Λ_{ECT}.

For searches for Technicolor particles an effective model is available, which approximates the Technicolor scenario at, for present experiments, accessible energies. This "Technicolor Straw Man Model" is the subject of the next section.

2.3 The Technicolor Straw Man Model

The model which is considered in this search is the so–called Technicolor Straw Man Model (TCSM) [14, 15]. This model is meant to provide reasonable predictions for the low–energy phenomenology of walking ETC models with only a limited number of free parameters, which are summarised in Table 2.3. In the TCSM it is assumed that only the lightest bound states of the lightest technifermion doublet

$$\begin{pmatrix} T_U \\ T_D \end{pmatrix}$$

determine the phenomenology of the model. The electric charges of these technifermions are Q_U and Q_D respectively. The bound states are vector and pseudoscalar mesons, see Table 2.2. The vectors include a spin–one isotriplet $\rho_T^{\pm,0}$ and an isosinglet ω_T. The ρ_T^0 and ω_T are assumed to be mass degenerate in this analysis and in the interpretation of the results. The lightest pseudoscalar bound states, the technipions, also form an isotriplet $\Pi_T^{\pm,0}$ and an isosinglet $\Pi_T^{0\prime}$. However, these are not mass–eigenstates. In the TCSM it is assumed that the technipions mentioned above are simple two state mixtures of the longitudinal weak gauge bosons $W_L^{\pm}$, Z_L - the true Goldstone bosons of dynamical electro–weak symmetry breaking - and of the mass–eigenstate pseudo Goldstone technipions $\pi_T^{\pm}$,

Vectors (Spin 1)	$\rho_T^{\pm,0}$	ω_T
Pseudoscalars (Spin 0)	$\pi_T^{\pm,0}$	$\pi_T^{0\prime}$

Table 2.2: *The particle spectrum of the TCSM.*

π_T^0:

$$|\Pi_T\rangle = \sin\chi|W_L\rangle + \cos\chi|\pi_T\rangle. \tag{2.25}$$

The mixing is described by the angle χ. In a similar way the $\Pi_T^{0\prime}$ is the composition of the mass–eigenstate $\pi_T^{0\prime}$ and other additional technipions neglected in the model, described by the mixing angle χ'. In this analysis the technipion mass–eigenstates $\pi_T^{\pm}, \pi_T^0$ and $\pi_T^{0\prime}$ are assumed to be mass–degenerate and $\chi = \chi'$ as suggested in [14, 15]. These mass–eigenstates will be referred to as technipions in the following.

At LEP the neutral Technicolor vector mesons ρ_T^0, ω_T will be produced in the s–channel process via propagator mixing with SM neutral gauge bosons. An off–shell standard model gauge boson "resonates" here into a Technicolor vector meson with the same electro–weak quantum numbers. This process is depicted in the Feynman diagrams of Figure 2.9. Besides the masses of the technimesons, their production cross–sections and decay branching ratios depend on the following model parameters:

1. The number of Technicolors $\mathrm{N_{TC}}$ of the Technicolor gauge group SU($\mathrm{N_{TC}}$). Here $\mathrm{N_{TC}}$= 4 is chosen as suggested in [14]. $\mathrm{N_{TC}}$ determines the coupling of the ρ_T^0 to $\Pi_T\Pi_T$, which is given by $\alpha_\rho = 2.91(3/\mathrm{N_{TC}})$ from scaling of QCD [14]. The partial decay width $\Gamma(\rho_T^0 \to \pi_T^+\pi_T^-)$ is proportional to α_ρ. It also determines the propagator mixing (*e.g.* between ρ_T^0 and γ which is proportional to $\sqrt{\alpha/\alpha_\rho}$, where α denotes the QED coupling constant).

2. The angle χ defines the mixing between the π_T and $\mathrm{W_L}$ states and is usually related to the number of technifermion doublets, $\mathrm{N_D}$, by the relation $\sin^2\chi = 1/\mathrm{N_D}$. A large value for $\mathrm{N_D}$ is required in order to make the Technicolor coupling rather "walking" than "running" [14]. Here $\mathrm{N_D} = 9$ is assumed, corresponding to $\sin\chi = 1/3$. The technipion decay constant (cf. Eq. 2.21 for one doublet) depends on the number of technifermion doublets and is given by $F_T = 246\,\mathrm{GeV}/\sqrt{\mathrm{N_D}}$ [14] in order to obtain the correct weak gauge boson masses.

3. The sum of the techniquark electric charges in a doublet $Q = Q_U + Q_D$. The decay width of i.e. $\rho_T^0 \to \pi_T^0\gamma$ is proportional to this quantity. Here it is set to be 5/3 as suggested in [14]. In order to avoid anomalies the relation $Q_D = Q_U - 1$ must hold.

4. Mass parameters M_V and M_A which influence the decay widths $\Gamma(\rho_T^0/\omega_T \to G\pi_T)$ where G are the transversely polarised SM gauge bosons. Generally the production cross–sections for these processes decrease when $\mathrm{M_V}$ resp. $\mathrm{M_A}$ are set to higher values. It should be $M_V \approx M_A \approx \mathcal{O}(100\,\mathrm{GeV})$. In this analysis they are assumed to be equal: $M_V = M_A = 200\,\mathrm{GeV}$.

$\mathrm{N_{TC}}$	$\mathrm{N_D}$	$\sin\chi = \sin\chi' = 1/\sqrt{\mathrm{N_D}}$	Q	$M_V = M_A$	$\lvert\epsilon_{\rho\omega}\rvert$	m_{ρ_T}=m_{ω_T}	m_{π_T}=m'_{π_T}
4	9	1/3	5/3	200 GeV	5%	variable	variable

Table 2.3: *The relevant parameters of the TCSM with the constraints and values assumed in this analysis. For the interpretation also a value of* $\mathrm{N_D}$= 2 *is considered.*

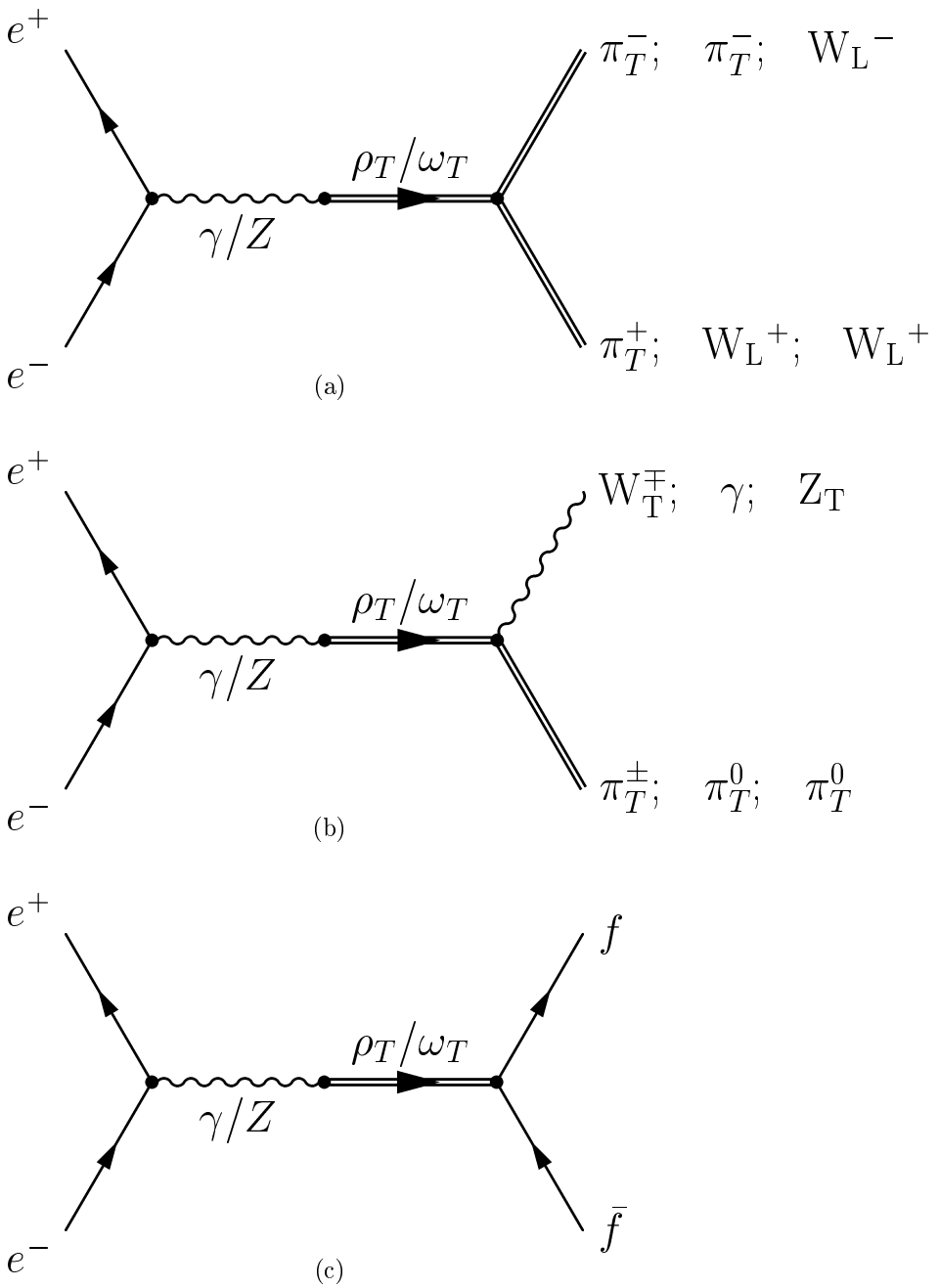

Figure 2.9: *The different Technicolor production processes: (a) decay via the TC interaction, (b) production of a technipion in association with a transversely polarised electro–weak gauge boson, (c) decay to a pair of SM fermions.*

The dominant decay modes of the ρ_T^0 mediated via the Technicolor interaction are

$$\rho_T^0 \longrightarrow \pi_T^+\pi_T^-, \qquad \Gamma \propto \alpha_\rho \cos^4\chi; \tag{2.26}$$

$$\longrightarrow \pi_T \mathrm{W_L}, \qquad \Gamma \propto \alpha_\rho \sin^2\chi \cos^2\chi; \tag{2.27}$$

$$\longrightarrow \mathrm{W_L^+ W_L^-}, \qquad \Gamma \propto \alpha_\rho \sin^4\chi. \tag{2.28}$$

$\mathrm{W_L}$ denotes the longitudinal component of the W boson. The partial widths for these processes are proportional to $\alpha_\rho \cos^4\chi$, $\alpha_\rho \sin^2\chi \cos^2\chi$ and $\alpha_\rho \sin^4\chi$, respectively. In

addition the ρ_T^0 decays into one technipion and a transversely polarised SM gauge boson

$$\rho_T^0 \longrightarrow \pi_T^{\pm} \mathrm{W}_{\mathrm{T}}^{\mp}, \qquad \Gamma \propto \alpha \cos^2\chi / M_A^2; \tag{2.29}$$

$$\longrightarrow \pi_T^0 \gamma, \qquad \Gamma \propto \alpha \cos^2\chi (Q/M_V)^2; \tag{2.30}$$

$$\longrightarrow \pi_T^0 \mathrm{Z}_{\mathrm{T}}, \qquad \Gamma \propto \alpha \cos^2\chi (Q/M_V)^2. \tag{2.31}$$

Here the subscript "T" on the SM gauge bosons means transversely polarised. These decay modes may become dominant if $\cos\chi \approx 1$ and $\rho_T^0 \to \pi_T^+\pi_T^-$ is kinematically forbidden. It should be noted that the decay to the neutral SM gauge bosons depends on the total charge of the technifermion doublet and vanishes for $Q = 0$. The decay to a pair of SM fermions via the electro–weak interaction is also possible:

$$\rho_T^0 \longrightarrow f\bar{f}, \qquad \Gamma \propto \alpha^2/\alpha_\rho. \tag{2.32}$$

Here the Technicolor vector meson resonates back to a Standard Model gauge boson which subsequently decays to a fermion pair.

The dominant decay mode of the ω_T via the Technicolor force is in principle the one into three technipions. However, for large areas of the TCSM parameter space this decay is kinematically forbidden. The isospin–violating ω_T decays into $\pi_T^+\pi_T^-$, $\pi_T \mathrm{W}_{\mathrm{L}}$, $\mathrm{W}_{\mathrm{L}}^+\mathrm{W}_{\mathrm{L}}^-$ are related to the ones for ρ_T^0 by

$$\Gamma(\omega_T \to \pi_T^+\pi_T^-, \pi_T \mathrm{W}_{\mathrm{L}}, \mathrm{W}_{\mathrm{L}}^+\mathrm{W}_{\mathrm{L}}^-) = |\epsilon_{\rho\omega}|^2 \Gamma(\rho_T^0 \to \pi_T^+\pi_T^-, \pi_T \mathrm{W}_{\mathrm{L}}, \mathrm{W}_{\mathrm{L}}^+\mathrm{W}_{\mathrm{L}}^-)$$

where $|\epsilon_{\rho\omega}|$ is the ρ_T^0–ω_T mixing amplitude, which is assumed to be $\approx 5\%$ as in QCD [14]. In addition the ω_T decays into one technipion and a SM gauge boson or a pair of SM fermions via the electro–weak interaction:

$$\omega_T \longrightarrow \pi_T^{\pm} \mathrm{W}_{\mathrm{T}}^{\mp}, \qquad \Gamma \propto \alpha \cos^2\chi / M_V^2; \tag{2.33}$$

$$\longrightarrow \pi_T^0 \gamma, \qquad \Gamma \propto \alpha \cos^2\chi / M_V^2; \tag{2.34}$$

$$\longrightarrow \pi_T^0 \mathrm{Z}_{\mathrm{T}}, \qquad \Gamma \propto \alpha \cos^2\chi / M_V^2; \tag{2.35}$$

$$\longrightarrow f\bar{f}, \qquad \Gamma \propto \alpha^2 Q/\alpha_\rho \tag{2.36}$$

All the different production channels are summarised in Figure 2.9.

In addition to the resonant production via ρ_T^0/ω_T the pair production of charged technipions $\mathrm{e^+e^-} \to \pi_T^+\pi_T^-$, and $\mathrm{e^+e^-} \to \pi_T^{\pm}\mathrm{W}_{\mathrm{L}}^{\mp}$ is also possible via a direct electro-weak coupling of the techniquarks to γ/Z. This production mechanism dominates for $m_{\rho_T/\omega_T} \gg \sqrt{s}$ and depends only on m_{π_T}, $\sqrt{s}$ and $\mathrm{N_D}{=}1/\sin^2\chi$. It is the reason for the $\mathrm{e^+e^-} \to \pi_T^+\pi_T^-$ and $\mathrm{e^+e^-} \to \pi_T^{\pm}\mathrm{W}_{\mathrm{L}}^{\mp}$ cross–sections to stay much larger than the $\mathrm{e^+e^-} \to \pi_T^{\pm}\mathrm{W}_{\mathrm{T}}^{\mp}$ cross–section for large ρ_T^0/ω_T masses, see Figure 2.10 (a). The former cross–sections converge to finite values when $m_{\rho_T/\omega_T} \to \infty$. Their values depending on the $\pi_T^{\pm}$ mass are shown in Figure 2.10 (b).

The technipions π_T^0 and $\pi_T^{\pm}$ decays are induced dominantly by ETC interactions which couple them to quarks and leptons proportional to the mass of the fermions involved in the decay:

$$BR(\pi_T^0 \to f\bar{f}) \;\propto\; m_f^2 \tag{2.37}$$

$$BR(\pi_T^{\pm} \to f\bar{f}') \;\propto\; (m_f + m_{f'})^2 \tag{2.38}$$

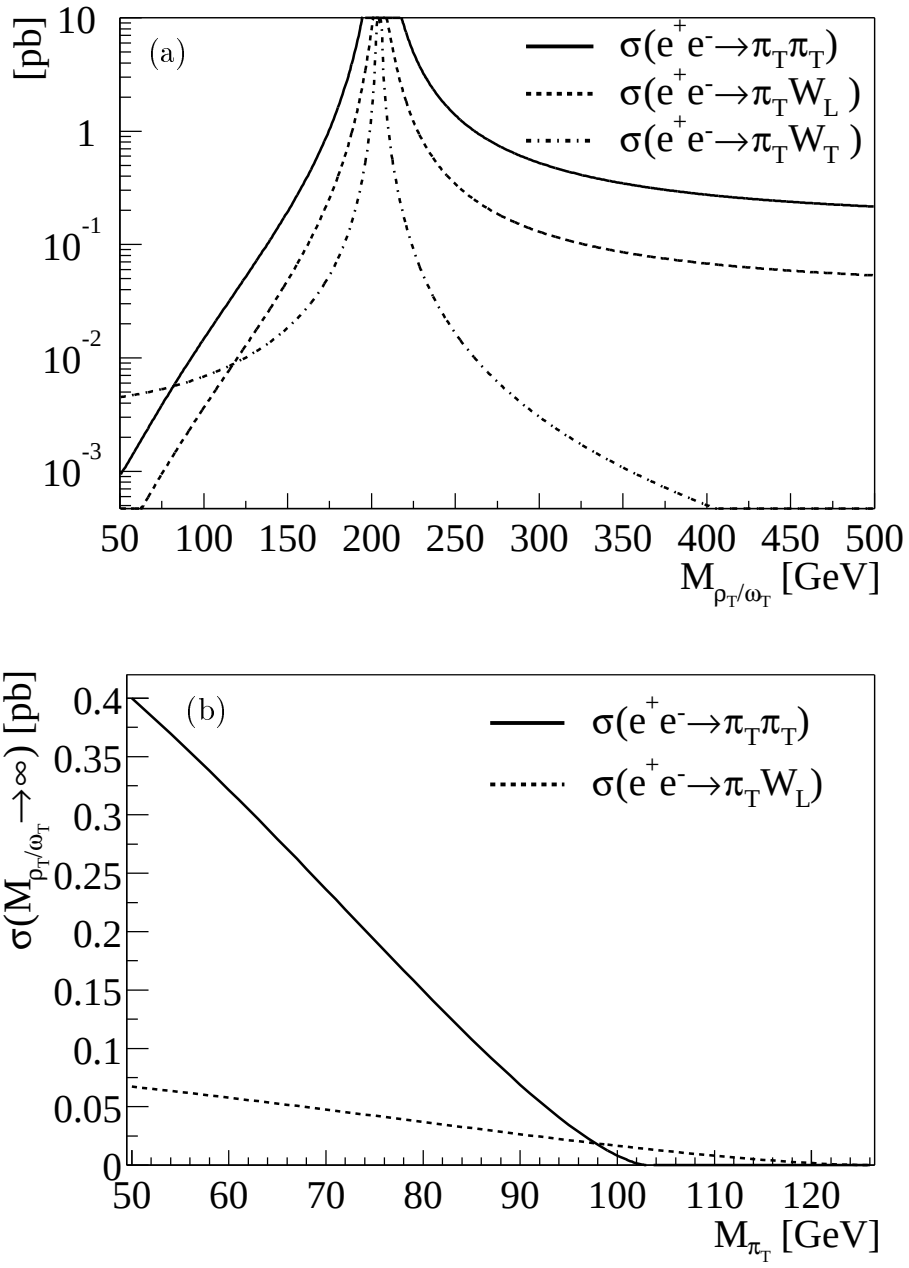

Figure 2.10: *(a) Technicolor production cross–sections for* $\sqrt{s}$*=206* GeV, $m_{\pi_T^{\pm}}$*=80* GeV, N_D*=9, Q=5/3 and* M_V=M_A*=200* GeV. *(b)* m_{π_T} *dependent cross–sections of the* $e^+e^-\to\pi_T^+\pi_T^-$ *and* $e^+e^-\to\pi_T^{\pm}W_L^{\mp}$ *channel for* $m_{\rho_T/\omega_T}\to\infty$. *The remaining parameters are the same as in (a).*

The technipions therefore preferentially decay into the heaviest fermion pairs possible at LEP2 centre–of–mass energies:

$$\pi_T^0 \longrightarrow b\bar{b}, \qquad BR \approx 85\% \tag{2.39}$$

$$\pi_T^- \longrightarrow b\bar{c}, \qquad BR \approx 56\% \tag{2.40}$$

$$\longrightarrow b\bar{u}, \qquad BR \approx 36\%. \tag{2.41}$$

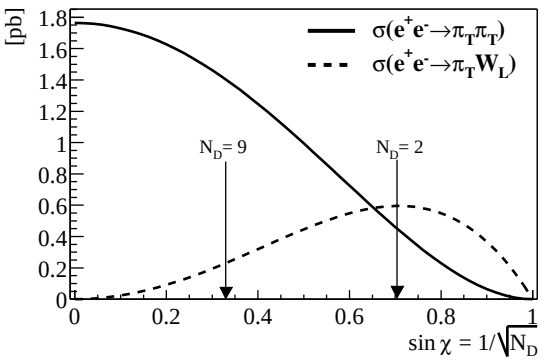

Figure 2.11: *The* $\sin\chi$ *dependence of the production cross–sections for* $e^+e^-\to\pi_T^+\pi_T^-$ *and* $e^+e^-\to\pi_T^\pm W_L^\mp$ *for* $\sqrt{s}$=*206* GeV, m_{ρ_T/ω_T}=*300* GeV, m_{π_T}=*50* GeV, *Q=5/3 and* M_V=*200* GeV.

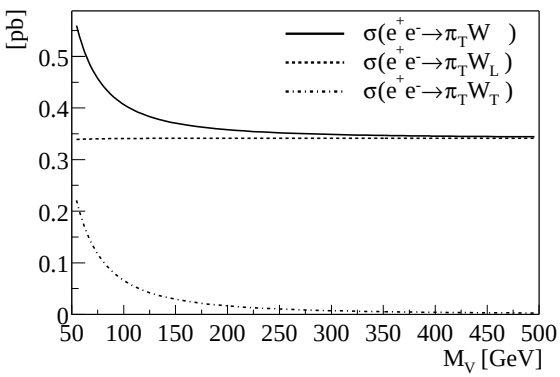

Figure 2.12: *The* $\pi_T^\pm W_T^\mp$ *production cross–section depends on* M_V *contrary to the* $\pi_T^\pm W_L^\mp$ *cross–section. TCSM parameters are* $\sqrt{s}$=*206* GeV, m_{ρ_T/ω_T}=*250* GeV, m_{π_T}=*80* GeV, N_D=*9 and Q=5/3.*

The search presented here considers the production of Technicolor particles in the following reactions:

$$e^+e^- \to \rho_T^0/\omega_T \to \pi_T^+\pi_T^- \to b\bar{q}\bar{b}q',\ \sigma = \sigma(m_{\rho_T/\omega_T}, m_{\pi_T^0}, \chi) \propto \cos^4\chi, \text{ and} \tag{2.42}$$

$$e^+e^- \to \rho_T^0/\omega_T \to \pi_T^\pm W^\mp \to bq\bar{q}'q''. \tag{2.43}$$

The Feynman diagrams of these channels are shown in Figures 5.4 and 5.13 respectively. The production cross–section for $e^+e^-\to\rho_T^0/\omega_T\to\pi_T^+\pi_T^-$ depends on the three TCSM parameters m_{ρ_T/ω_T}, m_{π_T} and $\sin\chi$. For longitudinal polarised W's the production cross–section of Eq. 2.43 depends on the same three parameters but is proportional to $\cos^2\chi\sin^2\chi$. The $\sin\chi$ dependence of these two cross–sections is shown in Figure 2.11. For transverse W's it is proportional to $\cos^2\chi$ and depends additionally on M_V. The latter dependence is shown in Figure 2.12 for the production of a charged technipion and a W. However, as can be seen from Figure 2.10 (a), the cross–sections for the $\pi_T^\pm W_L^\mp$ and $\pi_T^\pm W_T^\mp$ channel differ by several orders of magnitude for $m_{\rho_T} \geq 206$ GeV and the chosen set of TCSM parameters. The contribution of the $\pi_T^\pm W_T^\mp$ production channel to the total $e^+e^-\to\pi_T^\pm W^\mp$ cross–section is small for $M_V \gtrsim 100$ GeV, see Figure 2.12. Therefore only the $\pi_T^\pm W_L^\mp$ production channel is considered further.

Only the case $m_{\rho_T/\omega_T} \geq \sqrt{s}$, where $\sqrt{s}$ is the centre–of–mass energy of the e^+e^-collisions at LEP, is considered here. This is possible due to the large width of the ρ_T^0, *e.g.* $\Gamma_{\rho_T} = 21.2\,\text{GeV}(59.0\,\text{GeV})$ for m_{ρ_T}=250 GeV(400 GeV) and m_{π_T}=80 GeV, N_D=9, Q=5/3 and M_V=200 GeV. In Figure 2.13 the ρ_T^0 resonance is shown in the $e^+e^-\to\rho_T^0\to\pi_T^+\pi_T^-$ channel for m_{ρ_T}=250 GeV. The dashed curve shows the resonance in the case of an infinite ω_T mass. Generally m_{ω_T} influences the ρ_T^0 propagator, which leads to the interference shown as the solid line, when setting $m_{\rho_T}=m_{\omega_T}$ as assumed in this analysis.

For $m_{\rho_T/\omega_T} < \sqrt{s}$ initial state radiation (ISR), where the initial electrons radiate off one or more photons, has to be taken into account. Radiative returns to the ρ_T^0/ω_T pole may be dominant and hence an additional photon is expected in the event topology. This

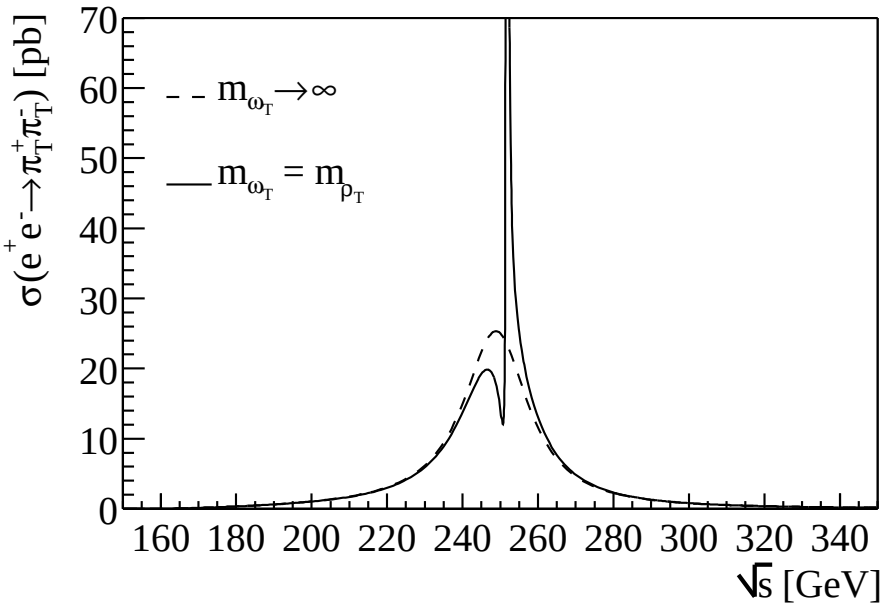

Figure 2.13: *The ρ_T^0 resonance in the $e^+e^- \to \rho_T^0 \to \pi_T^+\pi_T^-$ channel for m_{ρ_T}=250 GeV. The remaining parameters are set to N_D=9, Q=5/3 and M_V=200 GeV. The dashed line shows the ρ_T^0 resonance for $m_{\omega_T} \to \infty$. The solid line shows the appearance of the interference when setting m_{ρ_T}=m_{ω_T} as assumed in this analysis.*

photon might either be detected or escape along the beam pipe. In any case the selection should take the additional photon into account and this was not accomplished in the present analysis. The obtained selection efficiencies may therefore not be valid for signals including radiative returns to the ρ_T^0/ω_T pole. For $m_{\rho_T/\omega_T} \geq \sqrt{s}$ the effects of ISR are included in calculating the signal cross–sections and in generating signal Monte Carlo events.

For the interpretation of the search the non–resonant contribution to the cross–sections is also taken into account, which becomes constant for $m_{\rho_T/\omega_T} \gg \sqrt{s}$, cf. Figure 2.10 (b). This was not incorporated originally in [14–16] but is taken care of in [39], the programme used to calculate the cross–sections.

The channel

$$e^+e^- \to \rho_T^0/\omega_T \to \pi_T^0\gamma \to b\bar{b}\gamma, \quad \sigma = \sigma(m_{\rho_T/\omega_T}, m_{\pi_T^0}, \chi, Q, M_V) \propto \cos^2\chi \tag{2.44}$$

was analysed by Markus Schumacher. It is described together with the $e^+e^- \to \rho_T^0/\omega_T \to \pi_T^+\pi_T^-$ channel in [40] and will not be described further. Nevertheless, the results of this selection will be included in chapter 6.

Chapter 3

The Experiment

The analysis presented here is based on data taken by the OPAL (**O**mni **P**urpose **A**pparatus for **L**EP) detector at LEP (**L**arge **E**lectron **P**ositron collider) in the year 2000. Currently the LEP storage ring is being dismantled to provide space for the new proton–proton collider LHC (**L**arge **H**adron **C**ollider). This chapter describes briefly the LEP storage ring and the OPAL detector. Physics processes of interest are discussed and the last section describes how events are simulated for the OPAL detector.

3.1 The LEP Storage Ring

The LEP storage ring was based at CERN, the "European Organization for Nuclear Research", near Geneva. It was in operation from 1989, until the end of 2000. Bunches of electrons and positrons were accelerated in opposite directions in a circle of approximately 27 km circumference. The electron and positron bunches were brought to collision at four interaction points where the LEP experiments ALEPH, DELPHI, L3 and OPAL were situated, see Figure 3.1.

From the beginning of data taking in the autumn of 1989 and until the summer of 1995, the centre–of–mass energy $\sqrt{s}$ of the collisions was approximately 91 GeV, allowing the on–shell production of the Z boson through electron–positron annihilation. Each experiment collected an integrated luminosity of approximately $176\,\mathrm{pb}^{-1}$ which corresponds to $\approx 4.5 \times 10^6$ hadronic Z decays. This allowed for many high precision tests of the Standard Model. The autumn of 1995 marks the beginning of the so called LEP2 phase. Since then the centre–of–mass energy of the collisions was constantly increased up to $\approx$ 209 GeV. This is the highest centre–of–mass energy ever reached by an electron–positron collider. These high energies made it possible for the first time to produce on–shell pairs of the weak gauge bosons (W pairs: $\sqrt{s} \gtrsim 161\,\mathrm{GeV}$ and Z pairs: $\sqrt{s} \gtrsim 183\,\mathrm{GeV}$) at a lepton collider. One main motivation to reach these high energies was to find the Higgs boson but until the shut–down of LEP none was found. The lower bound on the Higgs mass by direct searches is determined to 114.1 GeV at the 95 % confidence level [1].

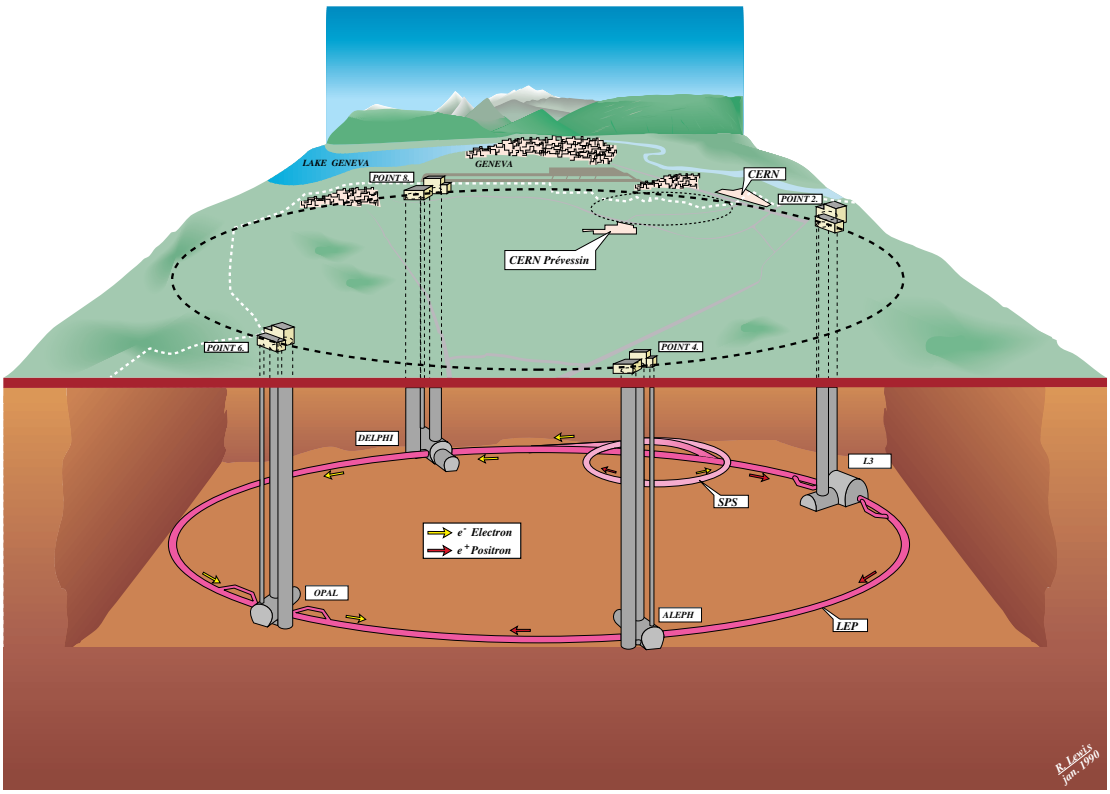

Figure 3.1: *The* LEP *storage ring situated approximately 100 m beneath the earth's surface. The four* LEP *experiments are indicated.*

3.2 The OPAL Detector

The OPAL detector was build to detect and identify all particles produced in an electron–positron collision. One exception are neutrinos, which do not interact with matter in a sufficient way to be detected at OPAL. The detected particles have subsequently to be identified and their four–momentum should be reconstructed. The OPAL detector consists of many components working together to fulfil these tasks. The ones most important for this analysis are described briefly below, a detailed description can be found in [41–44].

The OPAL detector is 12 m long and has a diameter of 10 m. Its total weight is about 3000 t. The fiducial region covers 97 % of the whole solid angle. To describe positions within the OPAL detector the following coordinate system is used. The $+z$ component is determined by the direction of the electron beam within the detector, the origin is placed at the nominal interaction point. The $+x$ axis points to the centre of the circular LEP storage ring and the azimuthal angle ϕ is defined with respect to this axis. The polar angle θ is defined with respect to the $+z$ direction. For an overview of the detector components and the coordinate system see Figure 3.2.

The **tracking system** consists of a silicon microvertex detector (SI) and three drift chambers: the vertex chamber (CV), jet chamber (CJ) and the Z-chamber(CZ). The latter three components are situated inside a pressure vessel holding a pressure of 4 bar. The silicon microvertex detector is placed between an inner beam pipe with a radius of 5.35 cm

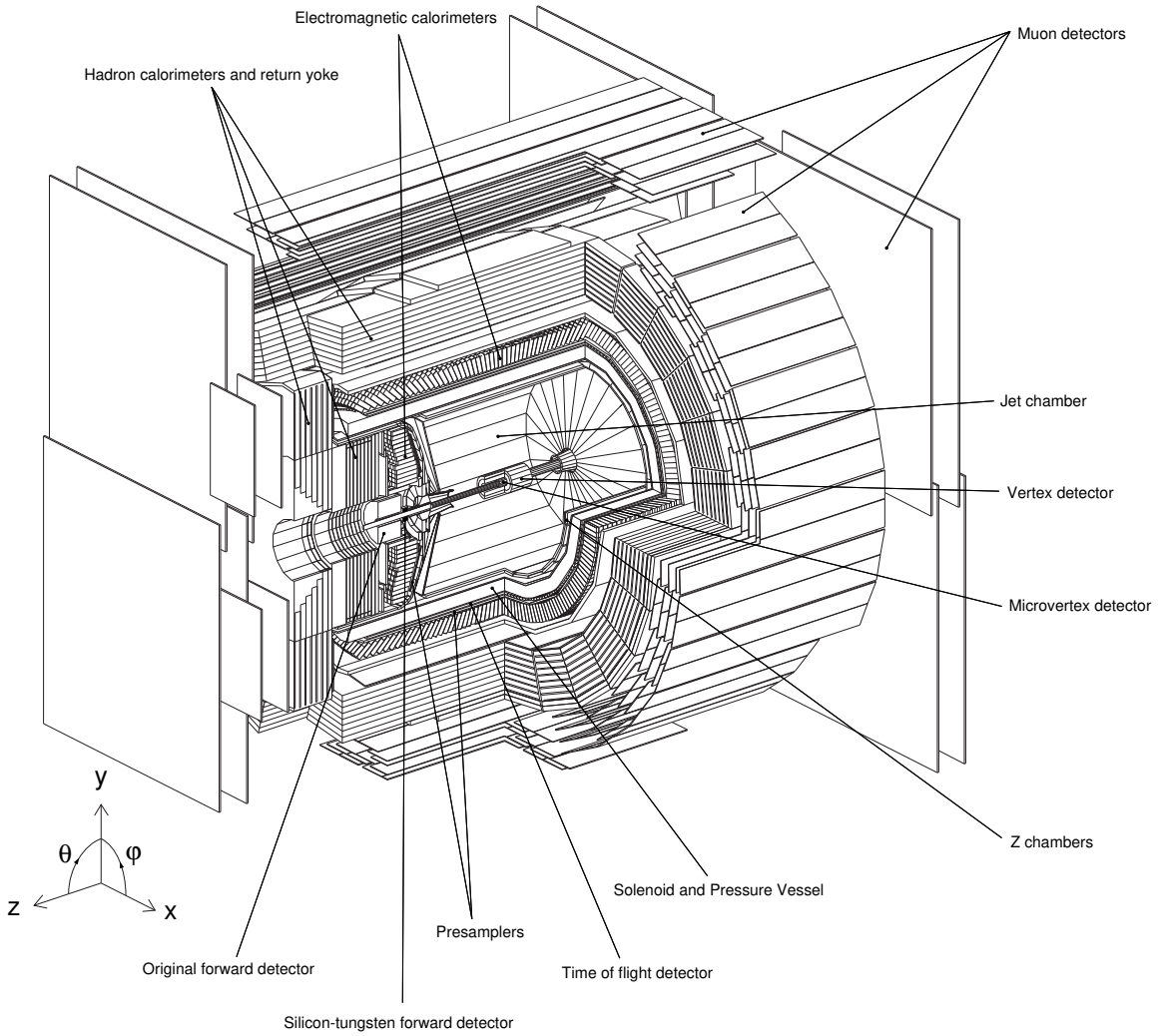

Figure 3.2: *The* OPAL *detector.*

and the inner wall of the pressure vessel which has a radius of 7.8 cm. The whole central detector is inside a solenoid supplying a uniform axial magnetic field of 0.435 T.

- The **silicon microvertex detector (SI)** consists of two barrels of silicon microstrip detectors at radii of 6 cm and 7.5 cm. Each silicon microstrip detector consists of one r–ϕ– and one r–z–waver glued together back to back. Its polar angle coverage for tracks with hits in each of the two layers is $|\cos\theta| < 0.89$. The azimuthal angle coverage for tracks with hits in each layer is 97 %. There are 629 strips per detector at 25 μm pitch and every other strip is read out at 50 μm pitch. This yields in a single hit resulution of $\approx 5\,\mu$m for r–ϕ–direction. The resolution in the z–direction is approximately 12 μm.

  The silicon microvertex detector is especially important for the reconstruction of secondary vertices due to the decay of particles with a lifetime up to $\approx 10^{-13}\,s$. This includes B–hadrons ($\tau \approx 1.5 \times 10^{-12}\,s$ corresponding to a flightlength of ≈ 5 mm at average B–hadron energies at LEP2) which are of special interest in this analysis. The impact parameter (d_0) resolution is measured to be 18 μm in the r–ϕ plane and

24 μm in the z–direction.

- The **vertex detector (CV)** is a cylindrical drift chamber. It is 100 cm long with an outer radius of 23.5 cm and consists of two layers of 36 sectors each. The inner layer contains the axial sectors, each containing a plane of 12 sense wires strung parallel to the beam direction. The outer layer contains the stereo sectors each containing a plane of 6 sense wires inclined at a stereo angle of 4°. A precise measurement of the drift time of electrons produced by a charged particle to the axial sector sense wires allows to calculate the r–ϕ–coordinate of a hit. This yields in a r–ϕ–resolution of about 50 μm. The z–coordinate is measured by combining the drift time information from axial and stereo wires. The obtained z–resolution is $\approx$ 700 μm. Due to an accident in 1998 only 21 of the 36 sectors containing the stereo wires were in operation since then.

- The **jet–chamber (CJ)** is a cylindrical drift chamber of length 400 cm with an outer radius of 185 cm and inner radius of 25 cm. The chamber consists of 24 identical sectors each containing a sense wire plane of 159 wires strung parallel to the beam direction. The coordinates of wire hits in the r–ϕ–plane are determined from a measurement of the drift time, yielding an average resolution of ≈ 130 μm for a single track. For jets with a high track density this resolution decreases significantly. The z coordinate is measured using a charge division technique, resulting in a resolution of ≈ 6 cm.

  Tracks of charged particles are bent due to the magnetic field. The transversal momentum of a charged particle can be determined by measuring the curvature of its track. This yields in a relative resolution for a charged particles transversal momentum of

  $$\frac{\sigma_{p_T}}{p_T} = \sqrt{(0.02)^2 + (0.0015(\mathrm{GeV}^{-1})p_T)^2}$$

  Summing the charges of all hits belonging to a track allows the calculation of a particles specific energy loss, $\mathrm{d}E/\mathrm{d}x$. This information can subsequently be used for particle identification. If all 159 wires receive a signal from a particle, the obtained relative resolution is

  $$\frac{\sigma_{\mathrm{d}E/\mathrm{d}x}}{\mathrm{d}E/\mathrm{d}x} = 3.8\,\%.$$

- The **z–chambers (CZ)** provide a precise measurement of the z coordinate of tracks as they leave the jet chamber. They consist of a layer of 24 drift chambers 400 cm long, 50 cm wide and 5.9 cm thick covering 94 % of the azimuthal angle and the polar angle range $|\cos\theta| < 0.72$. Each chamber is divided in z into 8 cells of 50 cm×50 cm, with every cell containing 6 sense wires. A z–coordinate resolution of ≈ 300 μm is reached.

For the detector components described in the following a rough distinction between the barrel (B) region ($|\cos\theta| \lesssim 0.72$) and the end–cap (E) region ($|\cos\theta| \gtrsim 0.72$) is usually made.

- The **time–of–flight (TOF)** system consists of plastic scintillation counters providing a time resolution of approximately 300 ps in the barrel and of ≈ 3 ns in

the end–cap region. It is mainly used to trigger on events and to suppress events originating from cosmic radiation.

- The **presamplers (PB) and (PE)** consist in the barrel region of four layers of streamer chambers and of multiwire proportional chambers in the end–caps. They are used to measure the charged multiplicity of clusters before they enter the electro–magnetic calorimeter. The central detector and the solenoid correspond to approximately two electro–magnetic radiation lengths. Therefore many charged particles create a shower before they enter the electro–magnetic calorimeter. The charged multiplicity of a cluster is proportional to the deposited energy and the energy measurement in the electro–magnetic calorimeter can be corrected accordingly.

- The **electro–magnetic calorimeter** consists in the barrel region (**EB**) of 9940 lead–glass blocks with a length corresponding to 24.6 radiation lengths and a cross–section of $10 \times 10\,\mathrm{cm}^2$. In order to maximise detection efficiency, the longitudinal axis of each block is angled to point at the interaction region. In the end–cap region (**EE**) it consists of 1132 lead–glass blocks with a length corresponding to 22 radiation lengths and a cross–section of $9.4 \times 9.4\,\mathrm{cm}^2$.

  The thickness of the lead–glass blocks ensures that electrons, positrons and photons deposit almost all of their energy in the electro–magnetic calorimeter. The deposited energy is determined by measuring the Čerenkov light emitted by relativistic electrons in the electro–magnetic shower passing through the lead glass. The light output is proportional to the deposited energy and is measured by photo–tubes at the base of each block. The relative energy resolution, taking into account the energy loss due to the central detector and the solenoid, is given by:

$$\frac{\sigma_E}{E} = \sqrt{(0.03)^2 + (0.16)^2(\mathrm{GeV})/E}.$$

- The **hadron calorimeter** is built in three sections, the barrel (**HB**), the end–caps (**HE**) and the pole-tips (**HP**), aiming at detecting all hadronically interacting particles. It consists of alternating layers of iron plates which also serve as return yoke for the magnetic flux and streamer chambers. Together with the electro–magnetic calorimeter it provides a thickness of more than seven hadronic radiation lengths. Therefore almost all hadronic energy of an event is deposited in the calorimeters. Only 0.1 % of all pions pass through the hadronic calorimeter, which makes it an efficient muon filter. The energy resolution is approximately $120\,\%/\sqrt{E/(\mathrm{GeV})}$.

- The **muon–chambers (MB) and (ME)** form the outermost layer of the OPAL detector. They aim at identifying muons in an unambiguous way, since almost all other particles are filtered out by the material in front of the muon–chambers. In the barrel region the muon–chambers consist of 110 drift chambers mounted in four layers. The azimuthal and axial resolution is 1–2 mm. In the end–caps they consist of 2×2 layers of perpendicular streamer chambers. The obtained resolution is again of the order of millimetres.

To calculate the event rates expected from a certain process the precise knowledge of the luminosity is essential. At OPAL the luminosity is measured utilising the theoretically

well understood process of Bhabha–scattering under small angles. To detect the Bhabha–electrons two detector systems in the extreme forward–direction are used:

- The **forward detector (FD)** is placed in the end–cap region and consists of a system of drift–chambers, proportional counters and a lead–scintillator–sandwich calorimeter. The whole system measures the luminosity to about 0.4 %.
- The **silicon tungsten detector (SW)** is a sampling calorimeter specially designed to measure the luminosity at high precision. It detects Bhabha–electrons emitted under polar angles between 25 and 59 mrad. The obtained resolution in the luminosity measurement is about 0.2 %.

The tracks of charged particles in the uniform magnetic field are helices. These can be described by five parameters in an unambiguous way. At OPAL the following **track parameters** are used:

- $|\kappa| = \frac{1}{2\rho}$: ρ is the curvature of the track projected in the r–ϕ–plane.
- ϕ_0: azimuthal angle of the track's tangent at the point of closest approach (p.c.a.) to the origin in the r–ϕ–plane.
- d_0: the impact parameter, defined as the distance between the p.c.a. and the origin.
- z_0: the z–coordinate at the p.c.a.
- $\cot\theta$: cotangent of the track's polar angle.

3.3 Physics Processes at LEP2

The search for Technicolor production requires a precise knowledge of all Standard Model processes occurring at LEP2. These SM processes need to be suppressed over several orders of magnitude in order to detect a signal from Technicolor production. The dominant processes occurring as background in this analysis are described below together with their event topology which discriminates them from the signal process, see section 5.2.

3.3.1 Two–Photon–Processes

The two–photon–processes have the largest event rate of all processes occurring at LEP2. Each of the initial leptons radiates off a photon which subsequently interact via a fermion loop, see Figure 3.3. The initial electron and positron are usually scattered under small angles and often escape undetected along the beam pipe. Two–photon–processes are characterised by small visible energy and multiplicity. Since the rate at which photons are radiated off the initial leptons is inversely proportional to the photon's energy, often only one photon is high–energetic. Hence the total longitudinal momentum parallel to the beam pipe is unbalanced and the main part of the detected energy is concentrated in one half of the detector. These clear signatures make it possible to suppress the two–photon–background efficiently despite its large cross–section of $\mathcal{O}(10\,\mathrm{nb}^{-1})$.

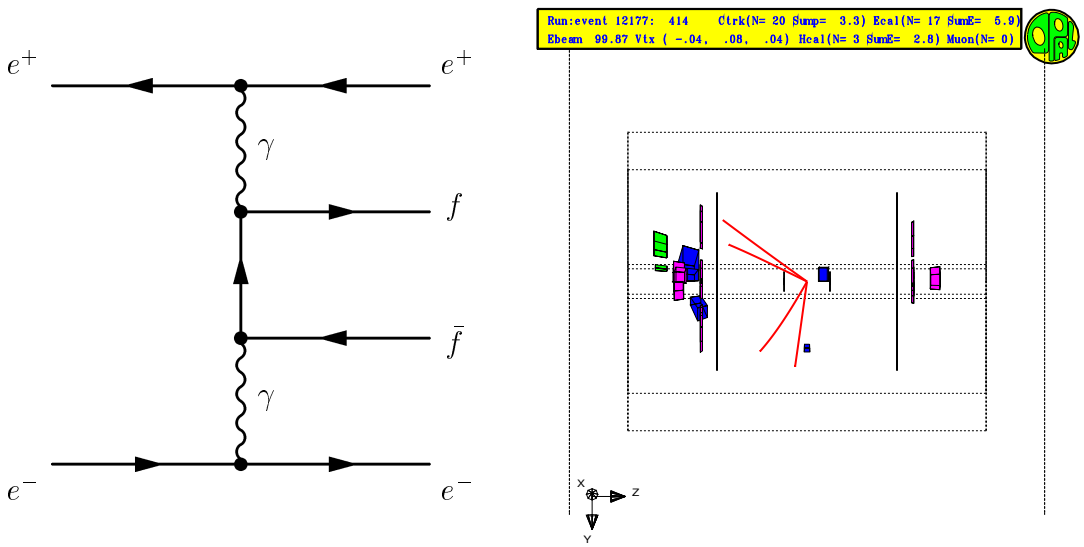

Figure 3.3: *The two–photon–process: The Feynman graph and a typical event detected by* OPAL *is shown.*

3.3.2 Two–Fermion–Processes

Two–fermion–processes describe the annihilation of an electron–positron pair into a neutral gauge boson γ or Z which subsequently decays into a pair of fermions. The production of a single Z boson is in roughly 90 % of all cases accompanied by a photon radiated off one of the initial leptons, see Figure 3.4. The energy of this photon is given

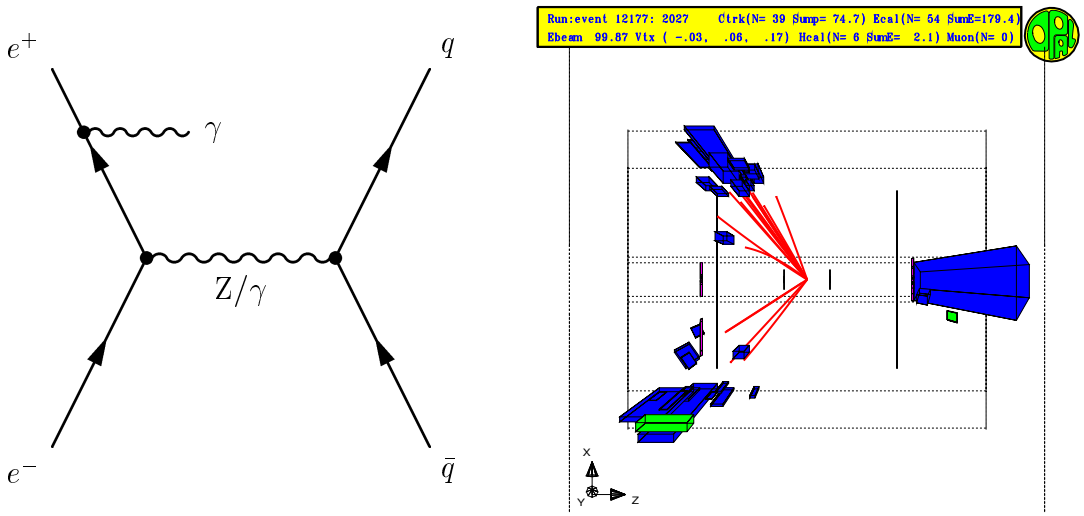

Figure 3.4: *A hadronic radiative return event. The Feynman graph and a typical event detected by* OPAL *are shown. The radiated off photon is detected in the electro–magnetic calorimeter and clearly visible as the large energy deposition on the right side of the event display.*

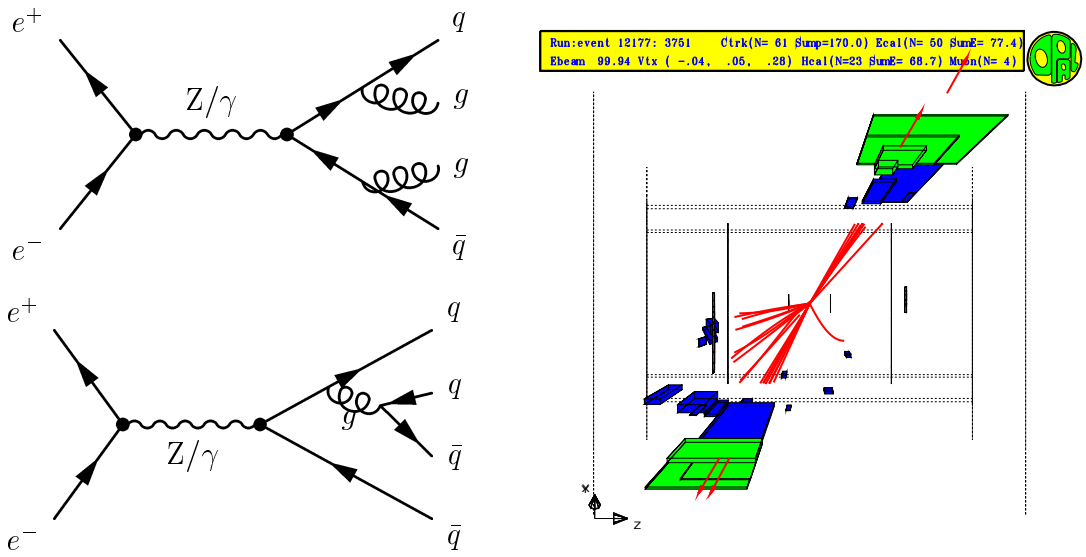

Figure 3.5: *Two possible Feynman diagrams showing hadronic two–fermion–processes giving rise to a four–jet final state. The event–display shows a hadronic two–fermion–event. The lower jet is split into two presumably due to gluon radiation.*

by $E_\gamma = (s - m_Z^2)/(2\sqrt{s})$ and the effective centre–of–mass energy of the electron–positron system is reduced to the Z mass. The photon is most probably radiated off under small angles and often escapes undetected along the beam pipe resulting in an unbalanced total longitudinal momentum. These events are also referred to as *radiative returns* to the Z pole.

Since the branching ratio of the produced gauge boson to quarks is dominant, approximately 70 % for the Z and 56 % for the photon, most two–fermion–events result in a hadronic final state. The final state quarks may radiate off one or more gluons which themselves may split into quark–antiquark or gluon pairs, see Figure 3.5. Thus two–fermion–events can result in a four–jet topology fairly similar to the signal topology. Hence they are an important background in this analysis. On the other hand the special event characteristic helps to separate this background efficiently from the signal. Radiative returns to the Z pole can be suppressed by a cut on the effective centre–of–mass energy $\sqrt{s'}$. The decay branching ratio of the Z boson to a pair of b–quarks, of which at least one is expected in a signal event, is relatively small (15 %) and so is the gluon splitting ratio to a pair of b–quarks ($\mathcal{O}(0.1\,\%)$). Therefore the application of b–quark identification techniques helps to reduce this background.

3.3.3 Four–Fermion–Processes

Four–fermion–processes include all electro–weak processes with four fermions in the final state with the exception of two–photon–events described above. Figure 3.6 shows a typical four–fermion–event detected by OPAL, and a sample of Feynman graphs for important processes is shown in Figure 3.7.

The cases where a pair of electro–weak gauge bosons is produced which subsequently

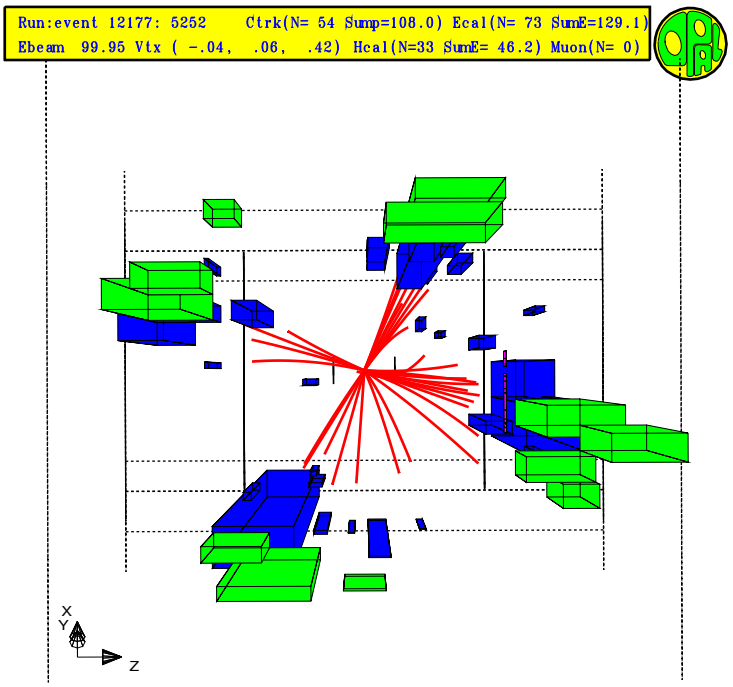

Figure 3.6: *A four–fermion–event detected by* OPAL. *Each of the four final state quarks produces a jet which are clearly separated in the detector.*

decay into pairs of quarks provide the main background for this analysis. Their event kinematics may be indistinguishable from the one expected from signal events, especially in the search for charged technipions with masses around 80 GeV and 91 GeV, the $W^{\pm}$ and Z masses.

However, the branching ratio of $\pi_T^- \rightarrow b\bar{q}$ is expected to be approximately 92 %, cf. section 2.3, whereas the $W^- \rightarrow b\bar{q}$ branching ratio is very small since the mixing of the third quark family with the other two is highly suppressed by the CKM–matrix, and the $Z \rightarrow \bar{b}b$ branching ratio is only about 15 %. Therefore the application of b–quark identification techniques helps again to suppress this background significantly.

Events with single leptons in the final state can be rejected by requiring a high track multiplicity in the event with more than one track per jet.

3.4 Simulation of Events

The simulation of the expected Standard Model background and the expected signal events is crucial for a search for new particles. A possible discovery is based on comparing the observed event rates with the ones expected from Standard Model processes alone (background–only hypothesis), and with the ones expected for the additional contribution of a signal (signal–plus–background hypothesis). For details see section 6.1. Thus a precise modelling of the physics processes and the detector response is crucial for obtaining reliable results.

The simulation process is divided into two steps:

1. **Monte Carlo (MC) generators** provide four–vectors of all particles expected in

an event of the process under consideration. The probability for a certain event topology is calculated from the differential cross–section of the process. Furthermore, applying MC–integration techniques allows the calculation of the total cross–section for a certain process. If quarks occur in the final state of a process the MC generator also provides algorithms to describe their fragmentation into hadrons.

In this analysis the following Monte Carlo generators are used:

- The charged technipion production is simulated with PYTHIA [45]. It allows the calculation of the different processes of the TCSM where the TCSM parameters can be chosen freely.
- $e^+e^- \to q\bar{q}(\gamma)$ events are simulated with KK2F [46], where fragmentation and hadronisation are handled by PYTHIA.
- Four–fermion–events are simulated with grc4f [47, 48], where fragmentation is handled by PYTHIA (string fragmentation). For a cross–check also samples with cluster fragmentation by HERWIG [49] are used.

2. The **detector–simulation** simulates the propagation of particles through the detector. Their interaction with matter, such as the ionisation of the gas in the drift–chambers, the formation of showers in the calorimeters, scattering of particles, etc., is determined. Based on the four–vectors provided by the Monte Carlo simulation the response of the different detector components is estimated to best knowledge. The simulation allows the study of the influence of the imperfections of the detector on the results obtained by a measurement. For OPAL a full detector simulation is provided by the GOPAL programme [50]. It is based on the GEANT programme–library [51]. The output data format of the GOPAL programme matches exactly the one provided by the event reconstruction software. This ensures that measured and Monte Carlo data can be treated in exactly the same manner.

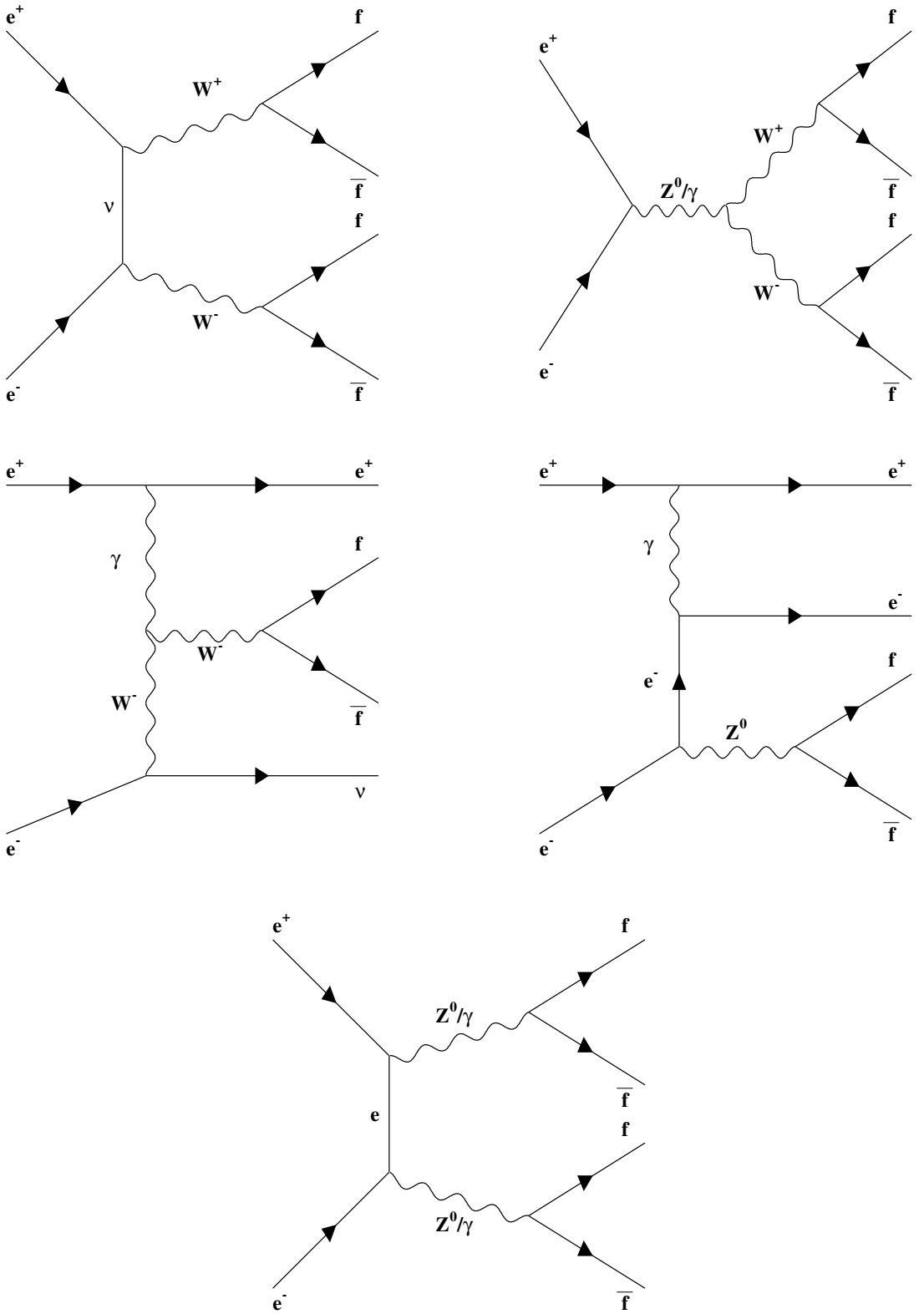

Figure 3.7: *Feynman diagrams of important four–fermion–processes: The top row shows* $W^{\pm}$ *pair production where the left graph shows the production via the t–channel and the right graph the s–channel. The middle row shows single production of weak gauge bosons. At the bottom the pair production of neutral electro–weak gauge bosons is shown.*

Chapter 4

The Event Reconstruction

Measurements with the OPAL detector provide tracks reconstructed by the tracking–system and the energy depositions in the electro–magnetic and hadron calorimeter. From this information the particles involved in the event have to be reconstructed. Quarks produced in the process hadronise into a bunch of particles, usually referred to as *jets*. The particle and jet reconstruction of an event is described in the first part of this chapter. The second part describes the identification of b–quarks (*"b–tagging"*).

4.1 Reconstruction of Event Kinematics

4.1.1 Reconstruction of Particle Energies and Momenta

All tracks reconstructed by the tracking–system and all clusters in the electro–magnetic or hadron calorimeter are treated equivalently as *energy–flow objects* at the beginning of the event reconstruction. Charged particles usually produce hits both in the jet–chambers and in the calorimeters. Naïve summation of all energy–flow objects in an event would therefore lead to overestimating the total energy deposition. To avoid double–counting of energy depositions originating from charged particles, a correction is applied to the energy measurement of the calorimeters. The algorithm described in the following is used at OPAL (matching track algorithm (MT) [52–54]).

All tracks measured by the tracking–system are extrapolated to the inner boundaries of the calorimeters. Clusters in the calorimeters with no tracks pointing to them are referred to as unassociated clusters and treated as massless photons. The energy measurement for clusters with associated tracks is corrected as described in the following.

For each track the expected energy deposition in the calorimeter is estimated depending on the momentum and polar angle of the track and possibly particle identification information as measured by the tracking–system. If the measured energy deposition in the calorimeter is larger than the estimated one, the energy of the calorimeter energy–flow object is decreased by the estimated energy and the object is subsequently treated as a photon. If the measured energy deposition in the calorimeter is smaller than the estimated one, the energy deposition is erased from the list of energy–flow objects. All remaining energy–flow objects are treated as *particles* in the following. The four–momentum of neutral particles is determined under the hypothesis of a massless photon, for tracks the pion mass is assumed.

4.1.2 Jet–Reconstruction

The combination of particles to jets is accomplished with an algorithm [55, 56] based on the idea of the Durham [57–60] and Jade [61] algorithm. In a first step the formation of jets is established using the Durham algorithm:

All particles of an event are interpreted as pseudo–jets. For each pair of pseudo–jets the "distance" y_{ik} is calculated in the Durham–metric:

$$y_{ik} = \frac{2\min\{E_i^2, E_k^2\}}{E_{\text{vis}}^2}(1 - \cos\theta_{ik}). \tag{4.1}$$

E_i is the energy of pseudo–jet i, E_{vis} is the visible energy of the event, and θ_{ik} is the solid angle between the pseudo–jets i and k. The two pseudo–jets having the smallest distance y_{ik} are merged into one new pseudo–jet n, where the four–vector of the new pseudo–jet is determined by $p_n^\mu = p_i^\mu + p_k^\mu$. This procedure is repeated until the desired number of jets is found. In this analysis the events are forced into four jets.

In a second step the momenta and energies of the four jets α, $\alpha = 1, \ldots, 4$, found by the Durham algorithm are recalculated using the Jade–metric for the distance:

$$y_{i\alpha}^{\text{J}} = \frac{E_i E_\alpha}{E_{\text{vis}}^2}(1 - \cos\theta_{i\alpha}). \tag{4.2}$$

For each particle the distances $y_{i\alpha}^{\text{J}}$ to all four jets is calculated and the particle is assigned to the "nearest" jet. When all particles are assigned, the momenta and energies of the four jets are recalculated from the energies and momenta of the particles assigned to a jet. This reassignment of the tracks increases the overall energy and momentum resolution of the jets.

If the event is forced into n jets usually the Durham measure $y_{n,n-1}$ is used to describe the probability of an event to have an n–jet topology. It is defined as

$$y_{n,n-1} = \min(y_{ik}), \quad \text{for } i \neq k, \quad \text{and } i, k = 1, \ldots, n, \tag{4.3}$$

i.e. as the minimum Durham measure between any two of the n jets. In this analysis y_{43} is used as a measure for the consistency of an event with the four–jet hypothesis. This variable helps to reject two–fermion–events since there the smallest distance between any two jets is usually smaller than for four–fermion–events.

4.1.3 Kinematic Fits

The jet energies and momenta are determined based on the four–vectors of all particles assigned to the jet. Neutrinos produced in the process of hadronisation are not taken into account. Also, depending on the region of the detector, some tracks or energy depositions may be measured poorly. To increase the energy and momentum resolution for the primary final state fermions, the jet momenta are constrained to boundary conditions motivated by an assumed event topology. Several event topology hypotheses can be tested and the fit returns a χ^2–probability for the event to fulfil the assumed boundary conditions.

In the kinematic fit the three–momenta $\vec{p}_i$ of the jets are varied within the errors of their measurement to fulfil the assumed boundary conditions $f(p_i^\mu) = 0$. The invariant

jet masses are fixed to the initial values and the jet energies are varied accordingly. The best estimate for the corrected jet momenta $\vec{p}_i'$ is obtained by minimising the quantity

$$\chi^2 = \sum_i (\vec{p}_i - \vec{p}_i')^t \; V^{-1}(\vec{p}_i) \; (\vec{p}_i - \vec{p}_i') \tag{4.4}$$

while taking the boundary conditions for the $\vec{p}_i'$ into account. $V(\vec{p}_i)$ is the covariance matrix of the measured momenta $\vec{p}_i$. The three–momenta are parametrised in $1/|\vec{p}|$, θ and ϕ since Monte Carlo studies show that the errors are approximately Gaussian in these variables.

The result of the fit is a set of new jet–momenta which perfectly match the boundary conditions. The measure of the fit quality under a certain boundary condition hypothesis is the χ^2–probability obtained. It is defined as

$$P_{\chi^2}(N_{\mathrm{dof}}) = \int_{\chi^2}^{\infty} \frac{x^{N_{\mathrm{dof}}/2-1} e^{-x/2}}{2^{N_{\mathrm{dof}}/2}\Gamma(N_{\mathrm{dof}}/2)} \mathrm{d}x. \tag{4.5}$$

N_{dof} is the number of degrees of freedom (dof) of the fit. It is

$$N_{\mathrm{dof}} = N_{\mathrm{measured}} - N_{\mathrm{fit}} + N_{\mathrm{constraints}}, \tag{4.6}$$

where N_{measured} is the number of measured parameters, N_{fit} the number of parameters to be fitted, and $N_{\mathrm{constraints}}$ the number of parameters constrained by the boundary conditions.

The distribution of $P_{\chi^2}(N_{\mathrm{dof}})$ for a large number of fits is flat for events which match the assumed boundary condition hypothesis and if the errors of the measured jet parameters are modelled correctly and distributed according to a Gaussian distribution. Events which do not or only partly fulfil the boundary conditions cluster at small values for $P_{\chi^2}(N_{\mathrm{dof}})$. Therefore the χ^2–fit–probability can be used to discriminate signal from background.

In this analysis the following kinematic fits are used:

- *4–C fit:* This **4**–**C**onstraints fit requires energy and momentum conservation in the event. The boundary conditions are

$$\sum_{i=1}^{4} E_i = \sqrt{s} \quad \text{and} \quad \sum_{i=1}^{4} \vec{p}_i = \vec{0}. \tag{4.7}$$

  Events with undetected initial state radiation or badly reconstructed events yield a low χ^2–fit–probability.

- *$\sqrt{s'}$–fit:* Energy and momentum conservation is required under the hypothesis of one or more photons being radiated off in the initial state. This fit aims at reconstructing the effective centre–of–mass energy.

- *5–C same–mass fit:* The fit, in addition to the energy–momentum constraint, tests the hypothesis that the four jets originate from the decay of two initial bosons which have the same mass. The invariant mass of pairs of jets is constrained to be the same respectively. This is done for all possible jet–combinations and the combination which yields the highest χ^2–fit–probability is selected. The same–mass fit is used in the search for charged technipion pair production.

- *5–C $\mathrm{W}^{\pm}$–mass fit:* The fit tests the hypothesis that the four jets originate from a $\mathrm{W}^{\pm}$ boson and another boson of unconstrained mass. It is used in the search for a charged technipion produced in association with a $\mathrm{W}^{\pm}$ boson.

4.2 Identification of b–Quarks

Crucial for the search for Technicolor production is the identification of B–hadrons originating from the hadronisation of primary b–quarks in the final state. A tool (LB package) has been developed to find B–hadrons within jets. Based on the information obtained, a *b–likelihood* $\mathcal{B}$ is assigned to each jet, quantifying the likelihood of the jet originating from an initial b–quark. In the following the LB package will be described briefly. For more details see [55, 62–64].

Several characteristics of b–jets discriminate them against other jets. The algorithm used to determine the b–likelihood of a jet combines the output of several specialised algorithms which are sensitive to a subsets of these characteristics in turn. The important characteristics of b–jets and the algorithms sensitive to these are described below.

4.2.1 The Lifetime Likelihood $\mathcal{L}_{lt}$

B–hadrons have a mean lifetime of $\tau \approx 1.5 \times 10^{-12}\,s$. Therefore they might fly up to approximately 5 mm in the detector before they decay. This results in a *secondary decay–vertex* within the jet and is a clear signature for B–hadrons. The measured flight length of B–hadrons is often elongated by tertiary decay–vertices due to the decay of charmed hadrons occurring as decay products of the B–hadron. The track resolution of OPAL is often not sufficient to separate these vertices and instead a vertex half way between them is found. Due to the high mass of B–hadrons ($m_B \gtrsim 5.3\,\mathrm{GeV}$) the secondary vertex also has an increased track multiplicity.

The outcomes of two independent algorithms contribute to the lifetime likelihood, quantifying the b–likelihood of a jet with respect to the mentioned characteristics. The general aspects of the likelihood method are discussed in detail in section 5.3.

- To identify secondary vertices in a jet it is first divided into sub–jets using the cone–algorithm [65–68]. Cones with small opening angles are constructed within a jet holding only subsets of all tracks. The sample of tracks in the found sub–jets are enriched with tracks originating from B–decays. To further suppress tracks originating from the fragmentation of the initial quark, the tracks are ordered by an order parameter. This order parameter is the likelihood of a track not to originate from the primary vertex and is obtained by an artificial neural network algorithm. The input parameters for this neural network are the track parameters in the r–ϕ– and r–z–plane, the transverse momentum of the track with respect to the cone axis, and the polar angle of the track. Secondary vertices are then reconstructed from the six tracks with the highest order parameter. If fewer than six tracks are assigned to a sub–jet, all found tracks are used.

  First an initial secondary vertex is constructed with the so called *tear–down* algorithm. A secondary vertex is fitted to the selected tracks and the track contributing dominantly to the χ^2 obtained by the fit is removed. This is repeated until only two tracks are left or all remaining tracks contribute with less than 5 to the χ^2 of the fit.

  In a second step all tracks of the jet are ordered by their geometrical distance to the vertex reconstructed by the tear–down algorithm. The nearest track is now

included in the reconstruction of the secondary vertex. If it contributes with less than 5 to the χ^2 of the fit, the old vertex is replaced with the new one. This is repeated until the nearest track contributes with more than 5 to the χ^2 of the fit (*build–up algorithm*).

From the distance of the reconstructed secondary vertex to the primary interaction point, the decay length significance $|l/\sigma_l|$ is calculated. The uncertainties of the position of the primary interaction point and of the secondary vertex contribute to the decay length uncertainty σ_l. To test the robustness of the fit, the reduced decay length significance is also calculated. Here the track with the highest order parameter is not used in the tear–down algorithm. This helps to discriminate badly reconstructed tracks which wrongly gain a very high order parameter.

- Not in every jet containing B–hadrons is a secondary vertex found by the algorithm described above. To gain a high b–jet identification nonetheless, an additional quantity is formed based on the impact parameter significances of all tracks in a jet. The impact parameter significance is defined as the absolute value of the impact parameter divided by its uncertainty. In the r–ϕ–plane it is defined as $|d_0/\sigma_{d_0}|$ and in the r–z–plane as $|z_0/\sigma_{z_0}|$. The impact parameter's significance in the r–ϕ– and r–z–plane serve as the two input variables for the impact parameter likelihood.

  Also the reduced impact parameter significance, where the track with the highest significance is ignored, is calculated as a cross–check.

The obtained decay length significances and impact parameter likelihoods are combined with the help of an artificial neural network into a single discriminating variable, the lifetime likelihood $\mathcal{L}_{lt}$. This variable serves as one of the input parameters for the final b–likelihood.

4.2.2 The Lepton Likelihood $\mathcal{L}_{p_t}$

Approximately 21 % of all B–hadrons decay semileptonically. The leptons originating from such semileptonic B–decays usually have a large transverse momentum with respect to the initial direction of the B–hadrons due to the large B–hadron mass.

The leptons are identified by the OPAL standard selection [69]. Electrons are required to have a minimal momentum of 2 GeV, muons of 3 GeV.. Since the initial b–quark and B–hadron directions are unknown, only the transverse momentum with respect to the jet axis can be calculated. However, the latter direction approximately coincides with the primary B–hadron direction since the B–hadron usually carries a large fraction of the total jet momentum. The transverse momenta for each lepton flavour are the inputs for the lepton likelihood $\mathcal{L}_{le}$.

Leptons are found only in approximately 6 % of the b–jets. Therefore the influence of $\mathcal{L}_{p_t}$ on the total b–likelihood is generally small. Nevertheless, if a lepton is identified the influence of the lepton likelihood increases significantly.

4.2.3 The Jet–Kinematic Likelihood $\mathcal{L}_{kin}$

The jets originating from b–quarks have an average higher track multiplicity due to the large B–hadron mass. Also the transverse momentum of the tracks with respect to the jet

axis is larger, i.e. b–jets are fanned out wider than jets originating from lighter quarks. An artificial neural network has been trained to be sensitive to these kinematic jet–characteristics. Input variables are the number of energy–flow objects in a cone of 0.4 rad opening angle around the jet axis, the angle between the jet axis and the sphericity axis of all tracks in the cone calculated in the rest frame of the jet, and the C–parameter for all energy–flow objects in a cone of 1.5 rad opening angle around the jet axis, again calculated in the rest frame of the jet. The sphericity axis is the eigenvector corresponding to the largest eigenvalue of the normalised momentum–tensor defined in section 5.2. The C–parameter is also defined therein.

The output of the neural network is the so called kinematic likelihood $\mathcal{L}_{kin}$. It has the lowest influence on the combined b–likelihood.

4.2.4 The Combined b–Likelihood $\mathcal{B}$

The three different likelihood values obtained by the algorithms described above are combined into a single variable with the help of the likelihood method, cf. section 5.3. The probability density functions $f_q^{\mathcal{L}_x}$ for three classes of quark flavours, $q = \mathrm{uds}, \mathrm{c}, \mathrm{b}$, and the three input variables $\mathcal{L}_x = \mathcal{L}_{lt}, \mathcal{L}_{p_t}, \mathcal{L}_{kin}$ are obtained from Monte Carlo samples produced at a centre–of–mass energy of $\sqrt{s} = m_Z$. The normalised b–likelihood of a jet, $\mathcal{B}$, is then given by

$$\mathcal{B} = \frac{w_b \mathcal{L}_b}{w_b \mathcal{L}_b + w_c \mathcal{L}_c + w_{uds} \mathcal{L}_{uds}}, \tag{4.8}$$

where

$$\mathcal{L}_q = f_q^{\mathcal{L}_{lt}} \cdot f_q^{\mathcal{L}_{p_t}} \cdot f_q^{\mathcal{L}_{kin}}. \tag{4.9}$$

The weight factors w_q determine the weights of the different quark flavours in the likelihood. In this analysis, all w_q are set to unity.

A comparison of the year 2000 calibration data, taken at $\sqrt{s} = m_Z$, and Monte Carlo is shown in Figure 4.1 (a). The agreement is good. Figure 4.1 (b) shows the performance of the b–identification method: if only jets with a b–likelihood larger than a certain value are selected, the curve describes the impurity of the sample compared to the selection efficiency of b–jets. If for example a cut on $\mathcal{B}$ is chosen such that 40 % of all b–jets are selected, the fraction of non–b–jets in the sample is roughly 4 %.

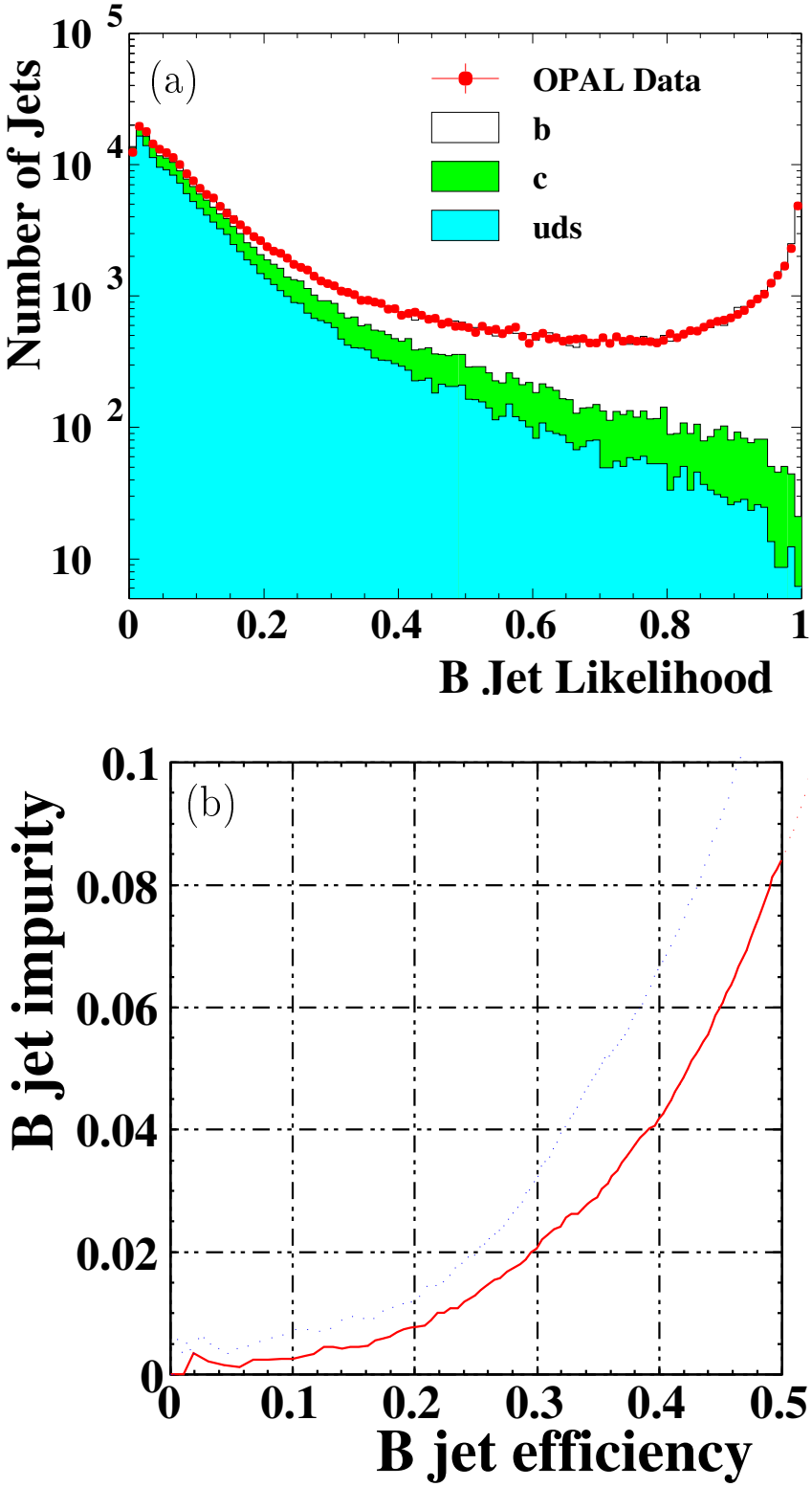

Figure 4.1: *(a) The distribution of the b–likelihood of jets is shown for the calibration data of the year 2000 compared to* $e^+e^- \to Z \to q\bar{q}$ *Monte Carlo. The light grey (turquoise) histogram shows the distribution for the u–,d–, and s–quarks, the dark grey (green) histogram for c–quarks and the open histogram for b–quarks. The dots with error bars (red) are* OPAL *data. Figure taken from [70].*
(b) The impurity over efficiency curve for the b–identification method. Figure taken from [62].

Chapter 5

The Selections

In this chapter the search for Technicolor production in the OPAL data of the year 2000 is described. In the first part the data set and Monte Carlo samples are summarised. The second part describes the search for $e^+e^- \to \rho_T^0/\omega_T \to \pi_T^+\pi_T^- \to b\bar{q}\bar{b}q'$ and $e^+e^- \to \rho_T^0/\omega_T \to \pi_T^+ W_L^- \to \bar{b}q\bar{q}'q''$ production respectively.

5.1 Data Set and Monte Carlo Samples

5.1.1 The Data Set

The search for Technicolor production is carried out on the OPAL data of the year 2000 at $\sqrt{s} \approx$ 200–209 GeV, corresponding to an integrated luminosity of 209.4 pb^{-1}. The distribution of the centre–of–mass energies for multihadronic events [71, *see also next section*] is shown in Figure 5.1. The luminosity weighted average centre–of–mass energy is 206.1 GeV.

5.1.2 Signal Monte Carlo Samples

Signal Monte Carlo (MC) samples are produced with PYTHIA [45] including the extension to produce Technicolor processes described in [16]. All samples are produced at a centre–of–mass energy of $\sqrt{s}$=206 GeV.

In the search for $e^+e^- \to \rho_T^0/\omega_T \to \pi_T^+\pi_T^- \to b\bar{q}\bar{b}q'$ production MC samples are produced for charged technipion masses ranging from 50 GeV up to 102 GeV, close to the kinematic limit of technipion pair production. Between 50 GeV and 90 GeV they are produced in steps of 5 GeV, between 90 GeV and 102 GeV in steps of 1 GeV. 5000 events are simulated in each MC sample.

For the $e^+e^- \to \rho_T^0/\omega_T \to \pi_T^+ W_L^- \to \bar{b}q\bar{q}'q''$ search channel MC samples for charged technipion masses ranging from 50 GeV up to 125 GeV, close to the kinematic limit, are used. Generally steps of 10 GeV separate individual MC samples, but for charged technipion masses around 80 GeV and close to the kinematic limit smaller steps are used to gain a better understanding of the selection efficiencies in these regions. 1000 events are simulated in each MC sample.

A summary of all signal MC samples used in this analysis is shown in Table 5.1.

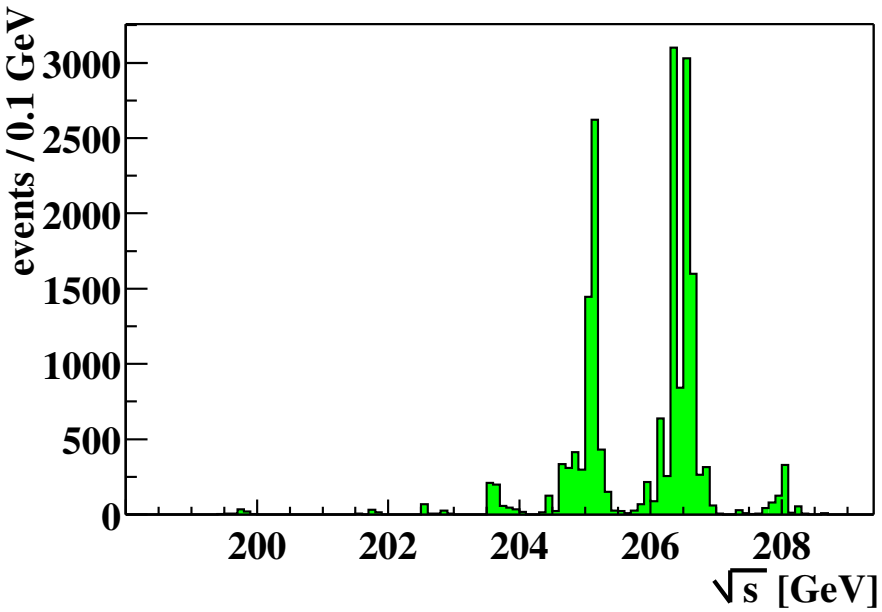

Figure 5.1: *The centre–of–mass energy distribution for multihadronic events detected with the* OPAL *detector in the year 2000. The luminosity weighted average centre–of–mass energy is 206.1* GeV.

5.1.3 Standard Model Background Monte Carlo Samples

The important Standard Model background processes for this analysis are described in detail in section 3.3. Two–photon– and leptonic two–fermion–processes are known to have only a negligible contribution to the total expected SM background after the preselection [72]. Therefore only four–fermion– and hadronic two–fermion–processes are considered further.

In the $e^+e^- \to \rho_T^0/\omega_T \to \pi_T^+\pi_T^- \to b\bar{q}\bar{b}q'$ search channel all Standard Model background MC samples are produced at a centre–of–mass energy of $\sqrt{s}$=206 GeV. The different samples are summarised in Table 5.2. The 4–fermion sample with two leptons in the final state ($qqll$) contains all lepton flavours except electron pairs. Those are handled in the separate $eeqq$–sample. The four–vectors for each process are produced by the Monte Carlo generators quoted in the second column. The fragmentation and hadronisation process is usually handled by PYTHIA [45], except for MC run no. 10962. Here the same

$\mathbf{e^+e^- \to \rho_T^0/\omega_T \to \pi_T^+\pi_T^- \to b\bar{q}\bar{b}q'}$	
$m_{\pi_T^\pm}$ [GeV]	50,55,60,65,70,75,80,85,90,91,92,93,94,95,96,97,98,99,100,101,102
number of events	5000
$\mathbf{e^+e^- \to \rho_T^0/\omega_T \to \pi_T^+ W_L^- \to \bar{b}q\bar{q}'q''}$	
$m_{\pi_T^\pm}$ [GeV]	50,60,70,75,78,80,82,85,90,100,110,115,120,122,124,125
number of events	1000

Table 5.1: *Summary of signal MC samples produced with PYTHIA for each search channel respectively.*

process (final state)	generator	N_{events}	$\mathcal{L}$ [pb^{-1}]	$\sqrt{s}$ [GeV]	OPAL run no.
2–fermion ($q\bar{q}(\gamma)$)	KK2F [46]	250000	3146	206	5193
4–fermion ($qqqq$)	grc4f [47, 48]	44870	5000	206	10071
4–fermion ($llqq$)	grc4f	47015	5000	206	10070
4–fermion ($eeqq$)	grc4f	191143	5000	206	10075
4–fermion ($eeee$)	grc4f	84535	5000	206	10072
4–fermion ($ee\mu\mu$)	grc4f	58125	5000	206	10073
4–fermion ($ee\tau\tau$)	grc4f	8701	5000	206	10074
4–fermion ($qqqq$)	grc4f	44870	5000	206	10962

Table 5.2: *Summary of Standard Model background MC samples used in the* $e^+e^- \to \rho_T^0/\omega_T \to \pi_T^+\pi_T^- \to b\bar{q}\bar{b}q'$ *and* $e^+e^- \to \rho_T^0/\omega_T \to \pi_T^+ W_L^- \to \bar{b}q\bar{q}'q''$ *search channels. The luminosity quoted for each MC sample corresponds to the number of events in the sample* (N_{events}) *assuming the cross–section for the process under consideration. For the sample in the last row cluster fragmentation (HERWIG) is used instead of to the standard string fragmentation (PYTHIA).*

four–vectors as in run no. 10071 are used, but cluster fragmentation by HERWIG [49] is applied.

As will be shown in section 5.5, additional MC samples produced at a higher centre–of–mass energy are needed in the search for $e^+e^- \to \rho_T^0/\omega_T \to \pi_T^+\pi_T^- \to b\bar{q}\bar{b}q'$ production. Therefore the most important Standard Model background Monte Carlo samples are also produced at a centre–of–mass energy of $\sqrt{s}$=208 GeV. They are summarised in Table 5.3. The MC samples for the same process produced at $\sqrt{s}$=206 GeVand 208 GeV are combined according to the luminosity of data events with $\sqrt{s} \leq 206$ GeV ($\mathcal{L} = 72.5\,\text{pb}^{-1}$) and $\sqrt{s} > 206$ GeV ($\mathcal{L} = 136.9\,\text{pb}^{-1}$).

process (final state)	generator	N_{events}	$\mathcal{L}$ [pb^{-1}]	$\sqrt{s}$ [GeV]	OPAL run no.
2–fermion ($q\bar{q}(\gamma)$)	KK2F	250000	3149	208	5191
4–fermion ($qqqq$)	grc4f	44831	5000	208	10347

Table 5.3: *Summary of additional Standard Model background MC samples used in the* $e^+e^- \to \rho_T^0/\omega_T \to \pi_T^+ W_L^- \to \bar{b}q\bar{q}'q''$ *search channel.*

5.2 Preselection

Each selection is divided into two steps:

1. In the preselection, events with a topology well distinct from the signal topology are rejected. Cuts are applied to variables which are sensitive to the general event topology. In addition quality cuts on the event reconstruction are applied to ensure a good reconstruction standard of the selected events.

2. In a second step the events selected in the preselection are fed into a likelihood selection in order to further exploit the fine differences between the signal and the SM background.

Signal events from both search channels have a similar topology: four quarks in the final state hadronise into four well separated jets and the visible energy is large. Therefore the preselection described in this section is nearly the same for both search channels.

The main background originates from $q\bar{q}(\gamma)$ events with hard gluon emission and from four–fermion processes, such as $e^+e^- \to W^+W^- \to q\bar{q}'q''\bar{q}'''$ or $e^+e^- \to ZZ \to q\bar{q}q'\bar{q}'$ (cf. section 3.3). The preselection aims at significantly reducing this SM background while keeping most of the signal events. It is based on the following cuts:

1. The event must qualify as a multi–hadronic final state as described in [71]. A minimum of five well reconstructed tracks and a minimum of seven clusters in the electro–magnetic calorimeter are required. The visible energy has to be larger than 14 % of the total energy. Further the energy should be balanced, i.e. a maximum of 75 % of the measured energy is allowed in one hemisphere of the detector. With these cuts the largest part of the 2–photon–events (cf. section 3.3) is removed.

2. The effective centre–of–mass energy $\sqrt{s'}$, i.e. the collision energy after removing the contribution of initial state radiation (ISR), is required to be at least $0.82 \times \sqrt{s}$. This rejects events with high energy initial state radiation such as radiative returns to the Z–pole.

   The effective centre–of–mass energy is computed in two different ways [73]. The first method assumes that the photon is radiated off in a rather large angle with respect to the beam pipe so that it is detected in the electro–magnetic calorimeter. The largest energy deposition in the electro–magnetic calorimeter without any track pointing to it, E_γ, is assumed to be the ISR photon and the effective centre–of–mass energy is computed as $\sqrt{s'} = \sqrt{(s - E_\gamma)^2 - |\vec{p_\gamma}|^2}$. The second method assumes the photon to escape undetected along the beam–pipe. A kinematic fit under this assumption is applied to the event, resulting in an alternative value. $\sqrt{s'}$ is then taken to be the smaller of the two computed values.

3. The events are reconstructed into four jets using the Durham algorithm [57–60]. The jet resolution parameter y_{43} has to be larger than 0.003. When the event is forced into four jets, y_{43} is the smallest Durham–distance between any two jets, cf. section 4.1.2. In $q\bar{q}(\gamma)$ events, this distance is usually relatively small since two jets originate from gluons radiated off the initial fermions or result from a hard gluon which subsequently splits into a pair of quarks. In four–fermion events, the

jets originate from the four initial fermions and the event is more spheric, i.e. y_{43} should be larger. This cut aims at reducing the $q\bar{q}(\gamma)$ background.

4. Each jet must contain at least two tracks. This increases the required minimum number of reconstructed tracks per event to eight. This cut aims at reducing four–fermion background with leptons in the final state. It is also a quality cut for the b–tagging since at least two tracks per jet are needed to define a secondary vertex, cf. 4.2.1.

5. A 4–C fit (cf. section 4.1.3) requiring energy and momentum conservation must converge and yield a χ^2–probability larger than 10^{-5}. This rejects events with large missing energy and ensures a good reconstruction quality for the events considered further. Secondly a 5–C fit is applied. Besides energy and momentum conservation an additional constraint is introduced, corresponding to the event topology of the signal.

   - $\underline{\mathrm{e^+e^-}\to\rho_T^0/\omega_T\to\pi_T^+\pi_T^-}$: The charged technipions have the same mass. Hence the 5–C fit constrains two di–jets to have the same invariant mass. Since the assignment of the jets to the technipions is unknown, the fit is applied to the 3 possible jet pairing combinations, see Table 5.4. At least for one of these combinations the fit is required to converge and yield a χ^2 probability larger than 10^{-5}. The di–jet combination yielding the highest χ^2 probability is used to reconstruct the invariant masses of the $\pi_T^\pm$ from the invariant di–jet masses.
   - $\underline{\mathrm{e^+e^-}\to\rho_T^0/\omega_T\to\pi_T^\pm\mathrm{W}^\mp}$: Two jets originate from the $\mathrm{W}^\pm$, the remaining two from the $\pi_T^\pm$. Here the 5–C fit constrains one invariant di–jet mass to the $\mathrm{W}^\pm$ mass, the other di–jet mass remains unconstrained. It is applied to all six di–jet combinations possible, see Table 5.9. The assignment of jets to the bosons is accomplished with a likelihood method and is described in section 5.5.1. The 5–C fit for the obtained di–jet combination should yield a χ^2 probability larger than 10^{-5}.

6. The C event shape parameter C_{par} [74, 75] is a measure for the sphericity of an event. It is required to be larger than 0.45. C_{par} has values close to 1 for spherical events and lower values otherwise. Hence this variable is used to reduce further the $q\bar{q}(\gamma)$ background. It is calculated as a combination of the eigenvalues of the normalised momentum–tensor [75]

$$\Theta_{ij} = \frac{\sum_{a=1}^{N} p_i^a p_j^a / |\vec{p^a}|}{\sum_{a=1}^{N} |\vec{p^a}|},$$

π_{T}^a	π_{T}^b
(1 2)	(3 4)
(1 3)	(2 4)
(1 4)	(2 3)

Table 5.4: *The three possibilities for assigning the jets (numbered from 1,...,4) to the charged technipions in the channel* $\mathrm{e^+e^-}\to\rho_T^0/\omega_T\to\pi_T^+\pi_T^-\to b\bar{q}\bar{b}q'$.

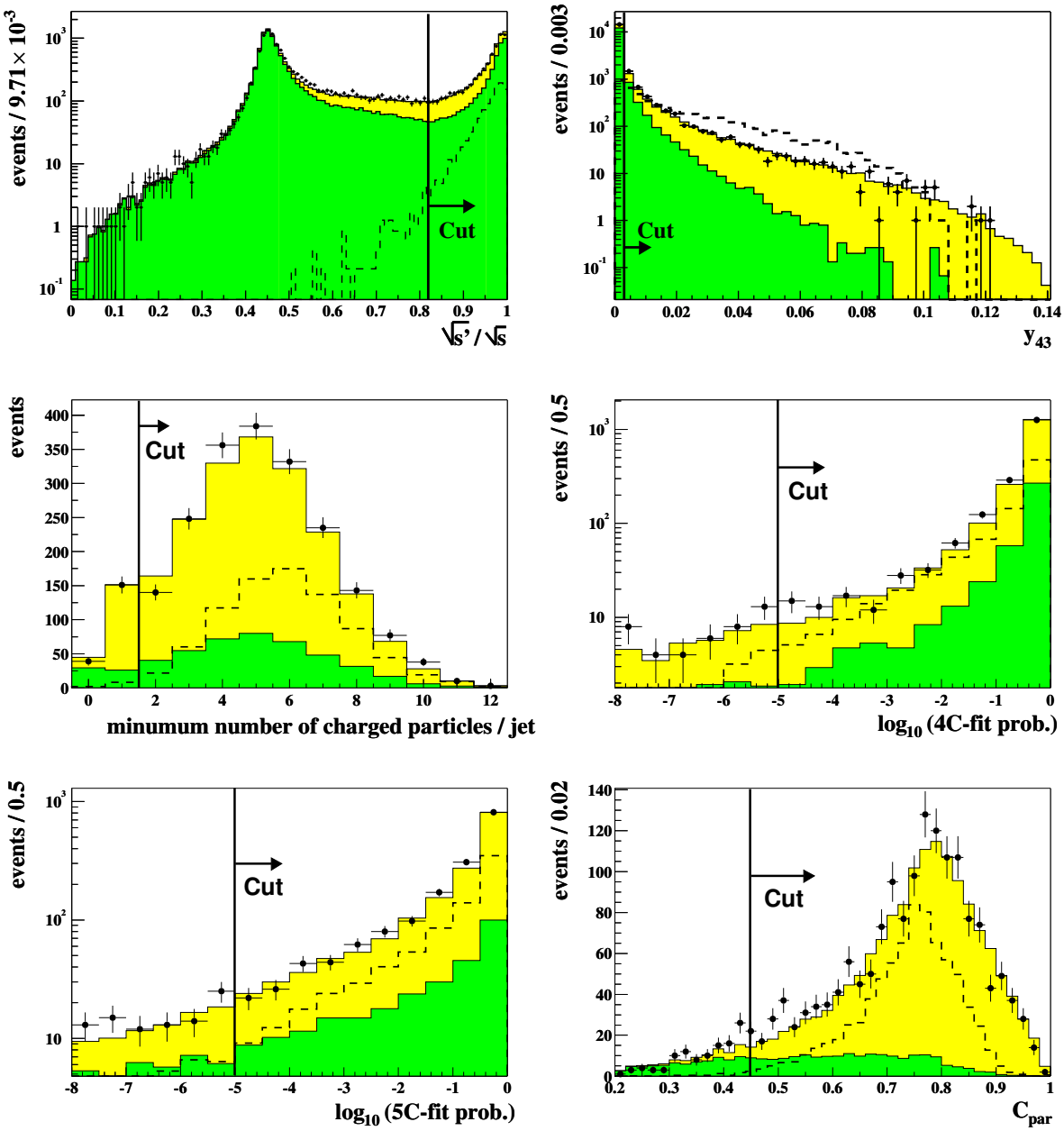

Figure 5.2: *Distributions of the preselection variables used in the search for* $e^+e^- \to \rho_T^0/\omega_T \to \pi_T^+\pi_T^-$. *The points with error bars are data, the dark grey (green) histograms are* $q\bar{q}(\gamma)$ *background on top of which four–fermion background is added in light grey (yellow). The distributions from background Monte Carlo are normalised to the data luminosity of* $209.4\,\mathrm{pb}^{-1}$. *Included is a signal distribution for* $m_{\pi_T} = 70\,\mathrm{GeV}$ *and an assumed cross–section of* $5\,\mathrm{pb}$*(dashed).*

where N is the total number of particles in the event, $i, j = 1, 2, 3$ and p_i^a is the i^{th} component of the three–momentum vector of particle a. C_{par} is defined as a combination of the three eigenvalues e_1, e_2, e_3 with $(e_1 < e_2 < e_3)$ of this tensor:

$$C_{\mathrm{par}} = 3(e_1e_2 + e_2e_3 + e_3e_1)$$

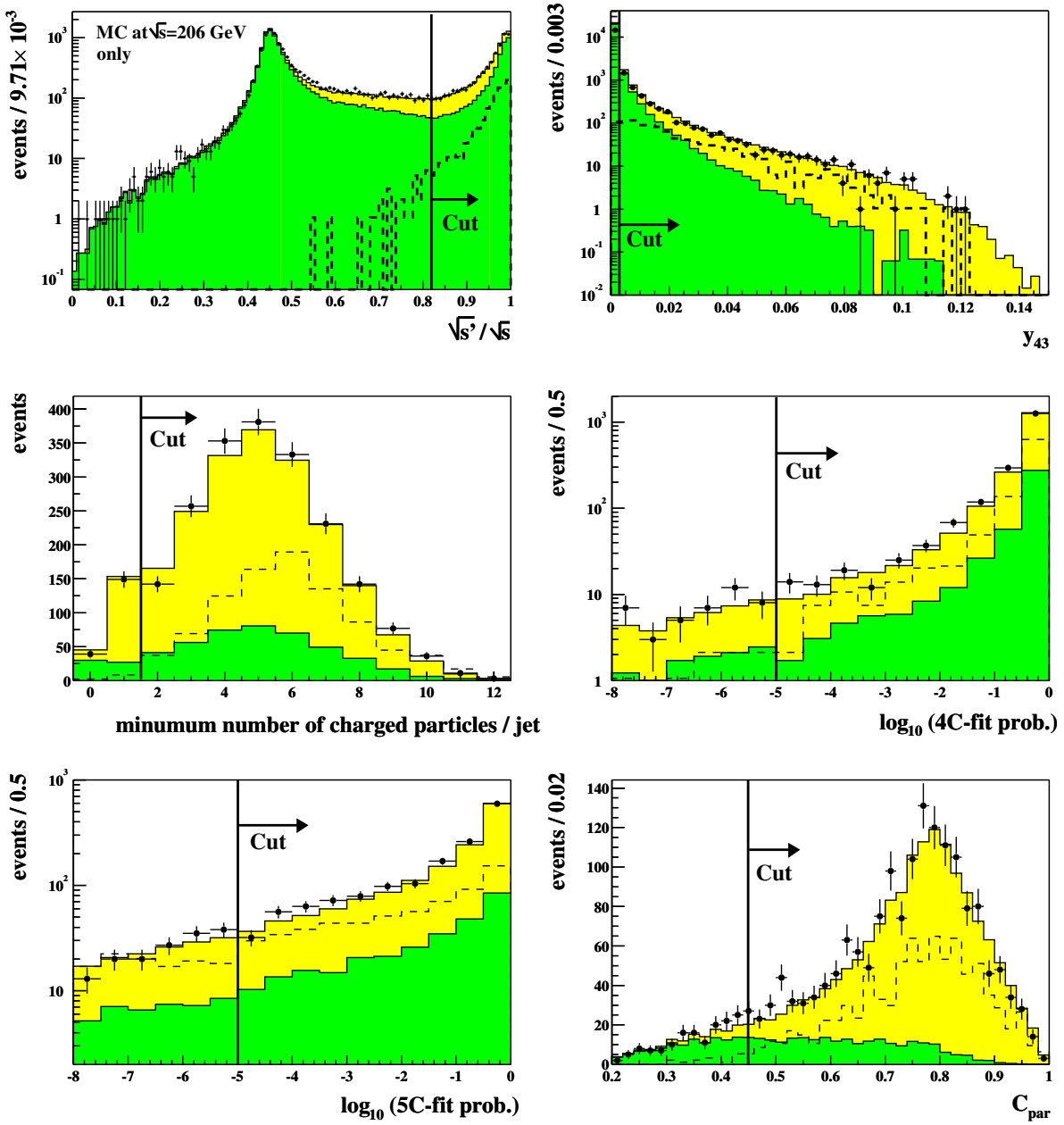

Figure 5.3: *Distributions of the preselection variables used in the search for* $e^+e^- \to \rho_T^0/\omega_T \to \pi_T^\pm W_L^\mp$. *The points with error bars are data, the dark grey (green) histograms are* $q\bar{q}(\gamma)$ *background on top of which four–fermion background is added in light grey (yellow). The distributions from background Monte Carlo are normalised to the total data luminosity of 209.4* pb^{-1}. *Included is a signal distribution for* m_{π_T} = *70* GeV *and an assumed cross–section of 5* pb *(dashed).*

Figures 5.2 and 5.3 show the distributions of the events for the preselection variables in the $e^+e^- \to \rho_T^0/\omega_T \to \pi_T^+\pi_T^-$ and $e^+e^- \to \rho_T^0/\omega_T \to \pi_T^+ W_L^- \to \bar{b}q\bar{q}'q''$ channel respectively. The applied cuts are indicated. The Standard Model background MC for $\sqrt{s'}/\sqrt{s}$ shown in Figure 5.3 is produced at a centre–of–mass energy of 206 GeV only and is not mixed

Cut	Data	Total bkg.	$q\bar{q}(\gamma)$	4-fermi.	Efficiency [%]
(1)	18498	18003.8	13862.8	4141.0	99.9
(2)	6258	6239.8	3888.4	2351.4	98.8
(3)	2154	2108.4	476.7	1631.7	80.2
(4)	1966	1907.6	420.4	1487.2	77.5
(5)	1664	1602.0	276.9	1325.1	70.7
(6)	1539	1488.2	188.8	1299.4	70.0

Table 5.5: *The* $e^+e^- \to \rho_T^0/\omega_T \to \pi_T^+\pi_T^-$ *channel: number of events after each cut for data and expected SM background, normalised to the data luminosity of 209.4* pb^{-1}*. The last column shows the signal selection efficiency for* $\pi_T^+\pi_T^- \to b\bar{q}\bar{b}q'$ *at* $m_{\pi_T} = 70\,\mathrm{GeV}$*.*

Cut	Data	Total bkg.	$q\bar{q}(\gamma)$	4-fermi.	$\pi_T^\pm \mathrm{W}_\mathrm{L}^\mp$ Eff. [%]
(1)	18498	18051.2	13910.9	4140.3	100.0
(2)	6258	6241.6	3893.8	2347.8	97.8
(3)	2154	2103.5	473.8	1629.7	81.2
(4)	1966	1906.1	417.8	1488.3	80.0
(5)	1784	1723.4	348.7	1374.7	74.6
(6)	1614	1567.1	221.1	1346.0	73.4

Table 5.6: *The* $e^+e^- \to \rho_T^0/\omega_T \to \pi_T^\pm \mathrm{W}_\mathrm{L}^\mp$ *channel: number of events after each cut for data and expected SM background, normalised to the data luminosity of 209.4* pb^{-1}*. The last column shows the signal selection efficiencies for* $\pi_T^+ \mathrm{W}_\mathrm{L}^- \to \bar{b}q\bar{q}'q''$ *at* $m_{\pi_T} = 70\,\mathrm{GeV}$*.*

with MC produced at $\sqrt{s} = 208\,\mathrm{GeV}$ as for the remaining plots. This is due to technical reasons. Using mixed MC here as well does not change the picture significantly. The overall agreement of the data with the Standard Model background Monte Carlo in all preselection variables of the two search channels is good.

Table 5.5 and Table 5.6 show the number of selected events after each cut for both search channels. An overall but statistically not significant enhancement in the data can be noted. The preselection cuts are the same for both channels up to cut (4). Hence there are no differences in the number of selected data events up to this cut. Deviations in the expected Standard Model background up to cut (4) are due to different compositions of the MC samples. The difference between the number of selected data events and the expectation from Standard Model background after cut (1) are due to two–photon–events which have been neglected in the SM background simulation. They are reduced to a negligible level after cut (2). The statistical error on the Standard Model background predictions after the last cut is $\mathcal{O}(0.1\,\%)$. The statistical errors on the selection efficiencies are $\mathcal{O}(1\,\%)$.

5.3 The Likelihood Method

The shapes of the distributions used to distinguish between the Standard Model background and a possible signal are not very discriminative. Applying cuts on these observables would not lead to a satisfactory suppression of the Standard Model background whilst keeping the signal selection efficiency reasonably high. The likelihood method

helps to improve this ratio. Here all observables are combined into a single discriminating variable, the likelihood.

In a first step n event classes are defined. For each of the m observables x_i used to distinguish between the n classes, the normalised probability density functions

$$f_i^j(x_i), \qquad \text{where } i = 1, \ldots, m \text{ and } j = 1, \ldots, n \tag{5.1}$$

have to be determined. The probability that an event belongs to class j when measuring the value x_i for variable i is then given by

$$p_i^j(x_i) = \frac{f_i^j(x_i)}{\sum_{k=1}^{n} f_i^k(x_i)}. \tag{5.2}$$

The *likelihood* $\mathcal{L}$ that an event belongs to class j when measuring m variables $x_1, \ldots, x_m$ is then given by the normalised product of the probabilities Eq. 5.2 over all m variables:

$$\mathcal{L}^j = \frac{\prod_{l=1}^{m} p_l^j(x_l)}{\sum_{k=1}^{n} \prod_{l=1}^{m} p_l^k(x_l)}. \tag{5.3}$$

The likelihood has values in the range 0,...,1. It is a measure for the probability that an event belongs to class j. Events belonging to this class cluster at relatively high values close to 1 for the likelihood $\mathcal{L}^j$. The events belonging to other classes have lower likelihood values.

In this analysis three event classes are defined: (1) the signal class, (2) hadronic four–fermion background, and (3) $q\bar{q}(\gamma)$ background. The introduction of two classes for the Standard Model background is appropriate since the distributions in the considered variables are quite different for two– and four–fermion backgrounds. This distinction improves the performance of the likelihood method.

The normalised probability density functions $f_i^j(x_i)$ for variable i and class j are obtained from Monte Carlo simulation of events belonging to the three defined classes respectively.

5.4 Search in the $e^+e^- \to \rho_T^0/\omega_T \to \pi_T^+\pi_T^-$ Channel

This section describes the search for charged technipion pair production in the $e^+e^- \to \rho_T^0/\omega_T \to \pi_T^+\pi_T^- \to b\bar{q}\bar{b}q'$ channel. The corresponding Feynman diagram is shown in Figure 5.4.

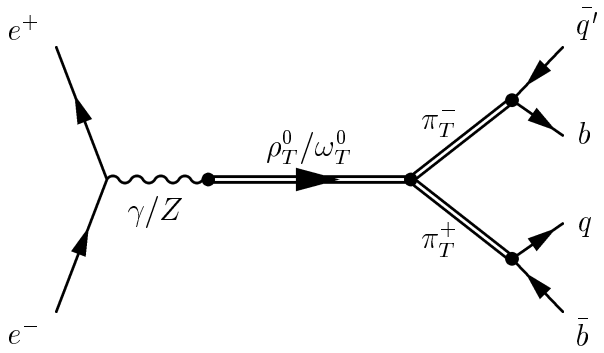

Figure 5.4: *The Feynman diagram of the* $e^+e^- \to \rho_T^0/\omega_T \to \pi_T^+\pi_T^- \to b\bar{q}\bar{b}q'$ *channel.*

The process is characterised by four well separated jets and large visible energy. Two b–quarks hadronising into b–jets discriminate the signal topology from most of the Standard Model background. A typical candidate event detected by OPAL is displayed in Figure 5.5.

The two di–jets originating from the two charged technipions respectively have to have the same invariant mass. This information is utilised in the 5–C kinematic fit which determines the assignment of the four jets to the technipions as described in section 5.2.

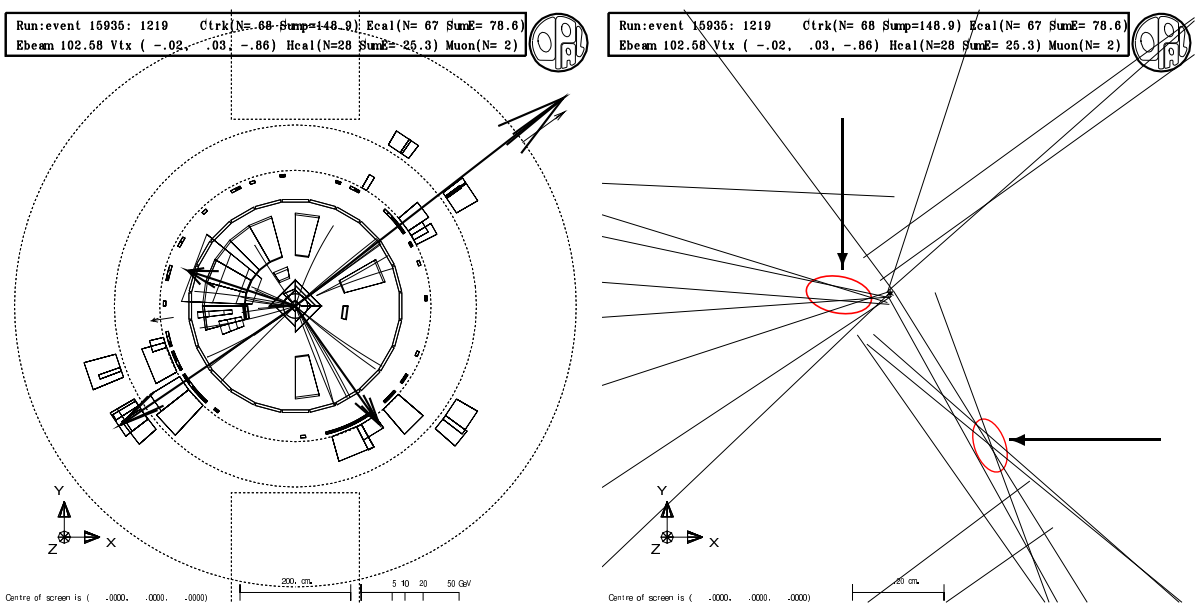

Figure 5.5: *A candidate event in the year 2000 data detected by* OPAL. *Four well separated jets are visible. The jet momenta constrained by the 4–C fit are superimposed as large arrows in the event display. The close–up picture of the interaction–point shows secondary vertices in two of the four jets (arrows). This is a typical indication for b–jets.*

The angular distribution of the produced scalar charged technipions is characterised by

$$\frac{d\sigma}{d\cos\theta} \propto \sin^2\theta, . \tag{5.4}$$

Contrary to this the $W^\pm W^\mp$ background is forward–peaked in $\cos\theta_{W^-}$.

5.4.1 Likelihood Selection

The likelihood selection is based on the following six variables:

1. The cosine of the di–jet production angle $\cos(\theta_{di-jet})$ multiplied by the di–jet charge, Q_{di-jet}. It aims at distinguishing the signal from SM background by the different production–angle distributions as described in the previous section. The di–jet charge is computed as suggested in [72]: first a measure for the total jet charge is calculated for each jet j, $j = 1, \ldots, 4$:

$$Q_j = \frac{\sum_{i=1}^{N} q^i \sqrt{p_{\mathrm{L}}^i}}{\sum_{i=1}^{N} \sqrt{p_{\mathrm{L}}^i}}.$$

   N is the number of tracks in jet j, p_{L}^i is the momentum of track i parallel to the jet direction and q^i is its reconstructed electric charge. These quantities are summed up for each di–jet. The one with the larger value is assigned a di–jet charge of $+1$, the other of -1.

2. The cosine of the polar angle of the thrust axis $\cos(\theta_{thrust})$. It is calculated as described in [45]. The momentum components parallel to a direction $\vec{n}$ of all particles are summed up. The direction $\vec{n}$ which maximises this sum is defined as the thrust axis of the event. As the previous variable $\cos(\theta_{thrust})$ utilises the different angular distributions for boson pair production.

3. The cosine of the smallest angle between all possible combinations of two jets $\cos\alpha_{min}$. This variable is intended to separate the $q\bar{q}(\gamma)$ background. Here the four–jet topology is due to hard gluon emission of the final quarks. The probability of a quark radiating off a gluon is largest for gluon emission under small angles. Hence the smallest angle between any two jets is expected to be smaller than for signal events.

4. The difference between the largest and smallest jet energy $E_{max} - E_{min}$ after the 4–C fit. This variable has its largest separation power for charged technipions production close to the kinematic threshold. Here the jet energies are determined by the masses of the bosons since they are produced approximately at rest. Lighter bosons have a larger Lorenz boost and therefore a wider spectrum of jet energies is expected. Hence $E_{max} - E_{min}$ has smaller values for technipions produced close to the kinematic limit and larger values for the production of lighter SM bosons or $q\bar{q}(\gamma)$ events.

5. The b–likelihood, see section 4.2, of the jet with the higher energy of the two jets with the highest b–likelihoods (b–likelihood 1). The two jets with the highest b–likelihoods are selected and subsequently ordered by their energy. This ordering by energy minimises the correlation between the two b–likelihood variables.

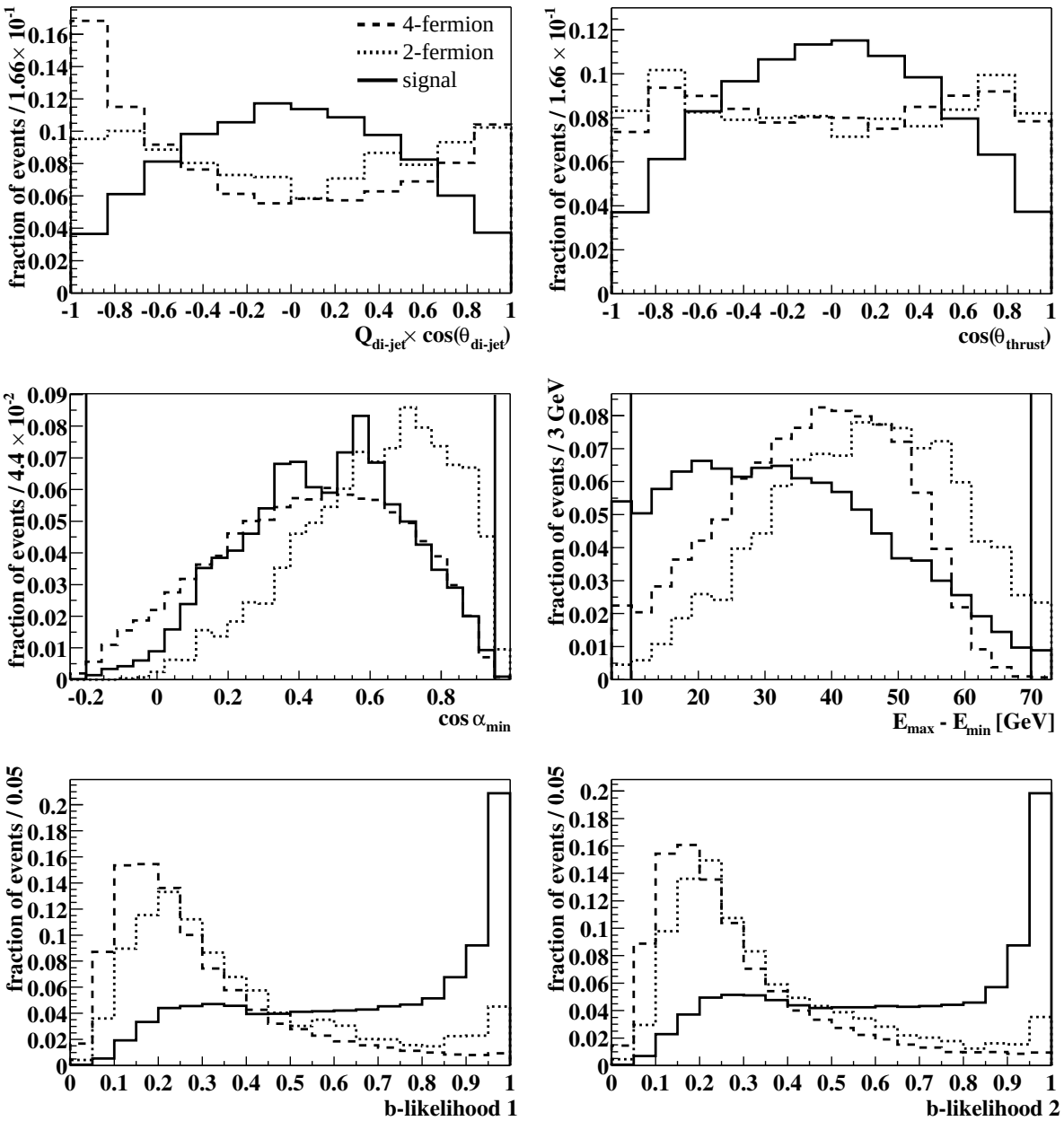

Figure 5.6: *The probability density functions for the six likelihood variables used in the* $e^+e^- \to \rho_T^0/\omega_T \to \pi_T^+\pi_T^-$ *selection. All distributions are normalised to unity. The three classes defined are four–fermion background (dashed),* $q\bar{q}(\gamma)$ *background (dotted), and the signal class (line). The signal distributions are averaged over the whole range of charged technipion masses from 50* GeV *up to 102* GeV*. Vertical lines in the histograms separate under– and overflow bins if they have non–vanishing contents.*

6. The b likelihood of the jet with the lower energy of the two jets with the highest b–likelihoods (b–likelihood 2).

The normalised probability density functions for the three classes and the six variables are shown in Figure 5.6. Since the mass of the charged technipion is unknown, the signal probability density functions are averaged over the whole mass range. The variables

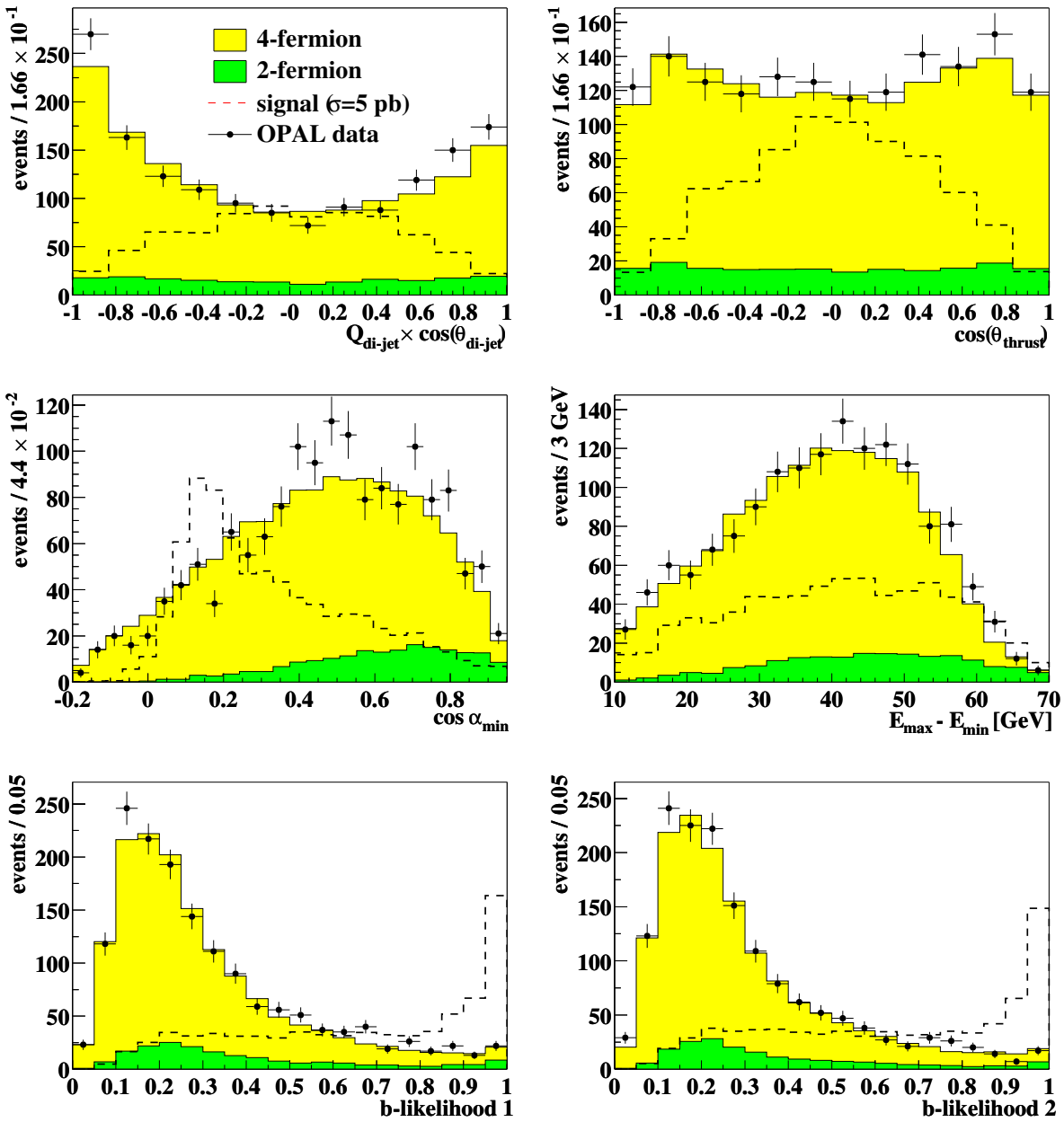

Figure 5.7: *Distributions of the six likelihood variables used in the search for* $\pi_T^+\pi_T^- \to b\bar{q}\bar{b}q'$. *The points with error bars are data, the dark grey (green) histograms are* $q\bar{q}(\gamma)$ *background on top of which four–fermion background is added in light grey (yellow). The distributions from background Monte Carlo are normalised to the data luminosity of* $209.4\,\mathrm{pb}^{-1}$. *Included is a signal distribution for* $m_{\pi_T} = 70\,\mathrm{GeV}$ *and an assumed cross–section of* $5\,\mathrm{pb}$ *(dashed).*

with the highest discriminative power are the two b–likelihood variables. Since they are ordered by the jet energies their correlation is small. The correlation between $Q_{di-jet} \times \cos(\theta_{di-jet})$ and $\cos(\theta_{thrust})$ is quite strong for small charged technipion masses, as shown in Figure 5.8. Here the two technipions have a large Lorenz boost and the emitted jets have smaller solid angles between them. The thrust axis coincides with the initial charged

technipion direction. Heavier $\pi_T^{\pm}$'s are produced nearly at rest and the whole event is more spheric. The thrust axis then does not necessarily coincide with the momentum vector of the produced technipions. No further significant correlations are observed between any other pair of likelihood variables. The di–jet charge calculation incorporated in $Q_{di-jet} \times \cos(\theta_{di-jet})$ is responsible for the asymmetry in the four–fermion background distribution for this variable.

Figure 5.7 shows the comparison between the OPAL data of the year 2000 and Monte Carlo in the six likelihood variables. The expected distributions for a signal with an assumed charged technipion mass of 70 GeV and a cross–section of 5 pb is also included. The overall data – Monte Carlo agreement is reasonably good taking the statistical errors of the data into account. Nevertheless, a shift between data and Monte Carlo description is adherent in $Q_{di-jet} \times \cos(\theta_{di-jet})$, and for $\cos(\alpha_{min})$ between 0.4 and 0.8 some larger deviations must be noted. The influence of these deviations on the Standard Model background expectation and the signal selection efficiency is treated as a systematic uncertainty and is further discussed in the next section.

The resulting likelihood distribution for the signal class is shown in Figure 5.9. Again the Monte Carlo distributions are normalised to the data luminosity. Good agreement between data and expected Standard Model background is observed. A signal for $m_{\pi_T^{\pm}}$=70 GeV with a cross–section of 0.5 pb corresponding to $m_{\rho_T/\omega_T} \approx 350$ GeV and the other TCSM parameters chosen as in Table 2.3 is assumed.

Events with a signal likelihood of larger than 0.7 are selected as candidate events. This leads to the following number of events expected resp. selected:

$\mathcal{L} > 0.7$				
data	total background	$q\bar{q}(\gamma)$ bgnd.	4–f ZZ bgnd.	4–f WW bgnd.
65	63.6 ± 1.8	14.9	22.0	26.7

The error quoted for the total expected Standard Model background is the statistical error only. The background is dominated by Standard Model four–fermion events, where the productions via $W^{\pm}$ or Z pairs contribute roughly equally. No significant enhancement of data events over background expected from the Standard Model is observed. Therefore

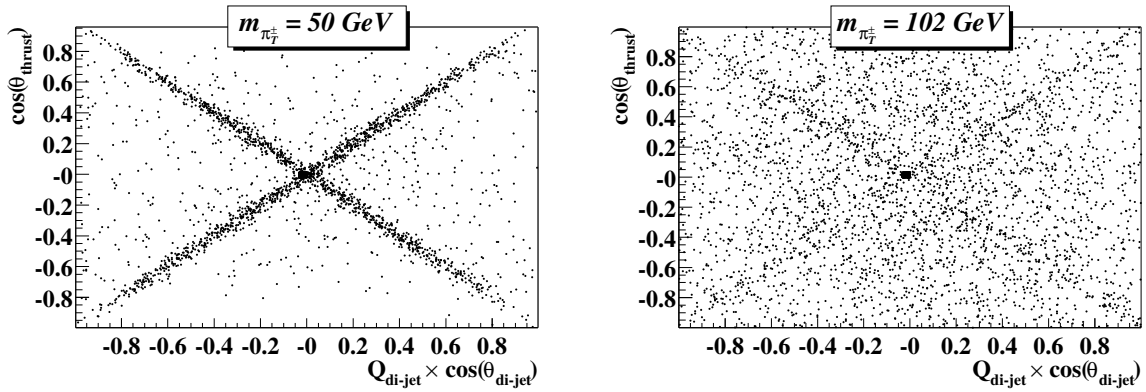

Figure 5.8: *The correlation between $Q_{di-jet} \times \cos(\theta_{di-jet})$ and $\cos(\theta_{thrust})$. It is strong for small technipion masses but almost vanishes when the technipions are produced close to the kinematic limit.*

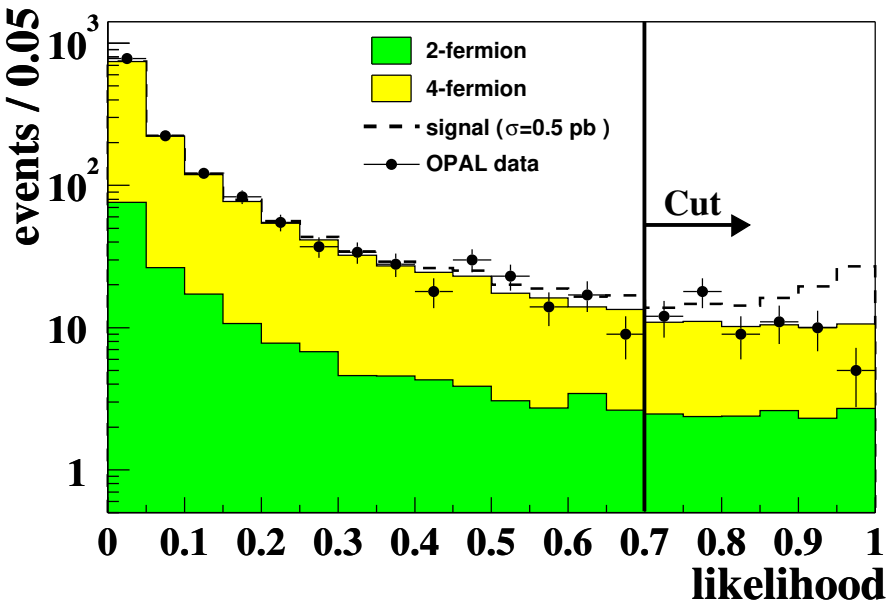

Figure 5.9: *The signal likelihood distribution in the* $e^+e^- \to \rho_T^0/\omega_T \to \pi_T^+\pi_T^- \to b\bar{q}\bar{b}q'$ *search channel. The points with error bars are data, the dark grey histogram (green) is* $q\bar{q}(\gamma)$ *background and the light grey (yellow) histogram is four–fermion background. The dashed line added on top of the SM background shows a signal distribution for* $m_{\pi_T} = 70\,GeV$ *and an assumed cross–section of 0.5 pb. All Monte Carlo distributions are normalised to the integrated luminosity of the data, 209.4* pb^{-1}.

the hypothesis of no technipion production is assumed further. The cut on the likelihood is determined by optimising the expected exclusion limit (see section 6.1.3) for charged technipion pair production. The expected cross–section times branching ratio (BR) limits for different cuts on the signal class likelihood are shown in Figure 5.10.

The selection efficiencies for different charged technipion masses are shown in Figure 5.11 (a). They range from 30 % for m_{π_T}=50 GeV up to 52 % for m_{π_T}=102 GeV. Since only a limited number of MC samples for different technipion masses is available, the selection efficiency is interpolated with a polynomial. The increase of the selection efficiency for higher $\pi_T^\pm$ masses is due to the increase of separation power for some of the likelihood variables with increasing m_{π_T}. Especially $E_{max} - E_{min}$ is designed for charged technipions produced at the kinematic limit, and the correlation between $Q_{di-jet} \times \cos(\theta_{di-jet})$ and $\cos(\theta_{thrust})$ vanishes.

The masses of hypothetical technipions in the selected events are reconstructed as the invariant di–jet mass, obtained by the 5–C kinematic fit. Hence the correct assignment of the four jets to the charged technipions is essential. The fraction of selected signal Monte Carlo events where the jets are correctly assigned is further referred to as the *jet–combination efficiency*. These efficiencies are shown in Figure 5.11 (b). An overall jet–combination efficiency of larger than 74 % is realised.

Figure 5.12 shows the reconstructed mass distribution for selected events. Also in the mass distribution no significant deviations of data compared to Standard Model background is manifest. The included signal distribution corresponds to m_{π_T}=70 GeV and a ρ_T^0/ω_T mass of 350 GeV. The dominant four–fermion background clusters at reconstructed

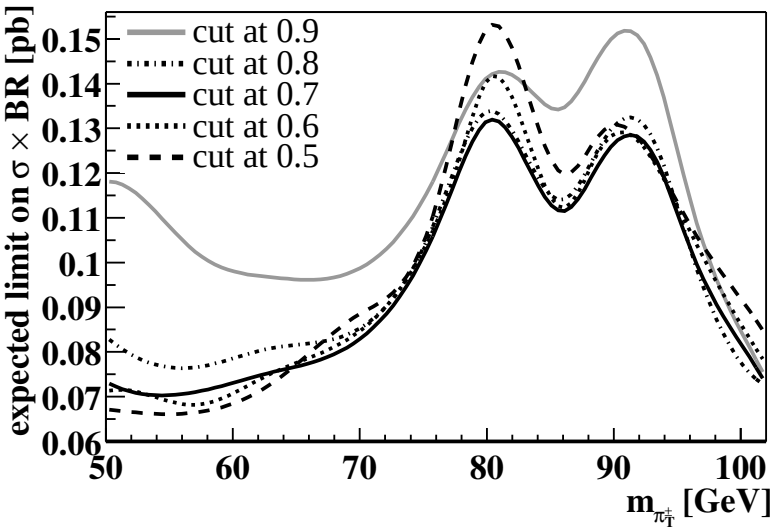

Figure 5.10: *Expected* $\sigma(e^+e^- \to \rho_T^0/\omega_T \to \pi_T^+\pi_T^- \to b\bar{q}\bar{b}q')$ *exclusion limits for different cuts on the signal likelihood.*

masses around the $W^{\pm}$ mass of $\approx 80\,\text{GeV}$ and around the Z mass of $\approx 91\,\text{GeV}$. Here the kinematic 5–C fit assigns the jets correctly to the weak gauge bosons. The tails to lower and higher masses in the four–fermion background distribution are due to combinatorial background where the assignment of jets to bosons is wrong. The $q\bar{q}(\gamma)$ background distribution is rather flat as expected, since the assumption of two initial bosons in the 5–C fit is not valid.

Since no excess in the data over the expected Standard Model background is observed, these mass distributions are used to derive limits on the production cross–section times branching ratio and to exclude areas in the TCSM parameter space as described in section 6.2.

5.4.2 Systematic Uncertainties

In this section influences on selection efficiencies and background predictions from uncertainties in the modelling of physics processes are discussed. Different sources of uncertainties are examined separately.

Modelling of pre– and likelihood–selection variables

Discrepancies between data and background MC prediction in the topological variables used in the selection process are studied here. Handling these deviations as systematic uncertainties assumes that they are not due to a signal modifying the distributions. This assumption is justified since the expected signal over background ratio is small even after the last preselection cut.

To examine the influence of deviations in the preselection variables, the mean values of the data ($\langle\text{data}\rangle$) and Monte Carlo ($\langle\text{MC}\rangle$) distributions are calculated. The selection process is repeated where in turn each preselection variable is scaled with the factor $\langle\text{data}\rangle/\langle\text{MC}\rangle$ for the MC events. Differences in the Standard Model background prediction

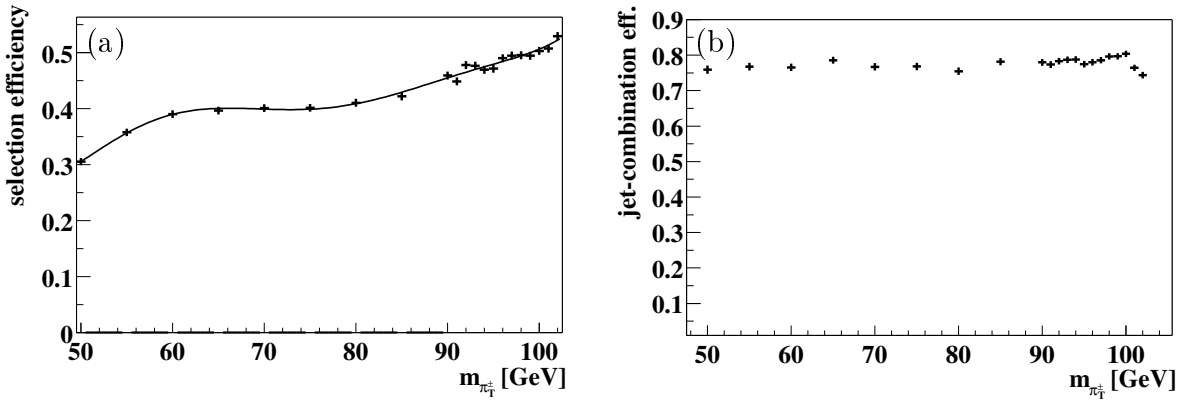

Figure 5.11: *(a) Selection efficiencies in the* $e^+e^- \to \rho_T^0/\omega_T \to \pi_T^+\pi_T^- \to b\bar{q}\bar{b}q'$ *search channel for charged technipion masses where MC samples are available. The selection efficiency is interpolated with a polynomial. (b) Jet–combination efficiencies for selected events in the* $e^+e^- \to \rho_T^0/\omega_T \to \pi_T^+\pi_T^- \to b\bar{q}\bar{b}q'$ *channel at different charged technipion masses.*

and the signal selection efficiency when calculated with or without the scaling factor are interpreted as systematic uncertainties. The values obtained are listed in Table 5.7.

Correcting for a shift in the mean values of distributions does not handle larger local variations correctly, e.g. as observed for $\cos(\alpha_{min})$. The scaling procedure is also not a correct method to compensate for a shift in non–linear variables such as i.e. $Q_{di-jet} \times \cos(\theta_{di-jet})$. Therefore the variables used in the likelihood selection are treated in a different way. Here the Standard Model background MC distributions are reweighted to reproduce the shape of the data distributions perfectly. The obtained weights are subsequently used to also reweight the signal distributions. The total number of MC events is conserved in the process. This reweighting is applied for each variable in turn, and the resulting differences in the selection efficiency and the expected background with or without reweighting are taken as the systematic uncertainty. The results are also listed in Table 5.7.

Only the contributions from $Q_{di-jet} \times \cos(\theta_{di-jet})$ and $E_{max} - E_{min}$ are large enough to contribute significantly to the total systematic uncertainty. The deviations observed in $\cos(\alpha_{min})$ have only a negligible effect due to the low separation power of this variable.

The influences of the kinematic fit probability and b–likelihood variables are studied separately below.

Track reconstruction

The track reconstruction quality has a large influence on the identification of secondary vertices resulting from B–hadron decays and is thus essential for this analysis. If the quality of the track reconstruction is overestimated in the detector simulation, fewer jets originating from light quarks will be wrongly identified as b–jets in the MC. This will enhance the number of b–jets identified in the data compared to the MC. Thus, a signal could be faked. On the other hand, an underestimation of the track reconstruction quality could lead to a signal being ignored. The most important track parameters for

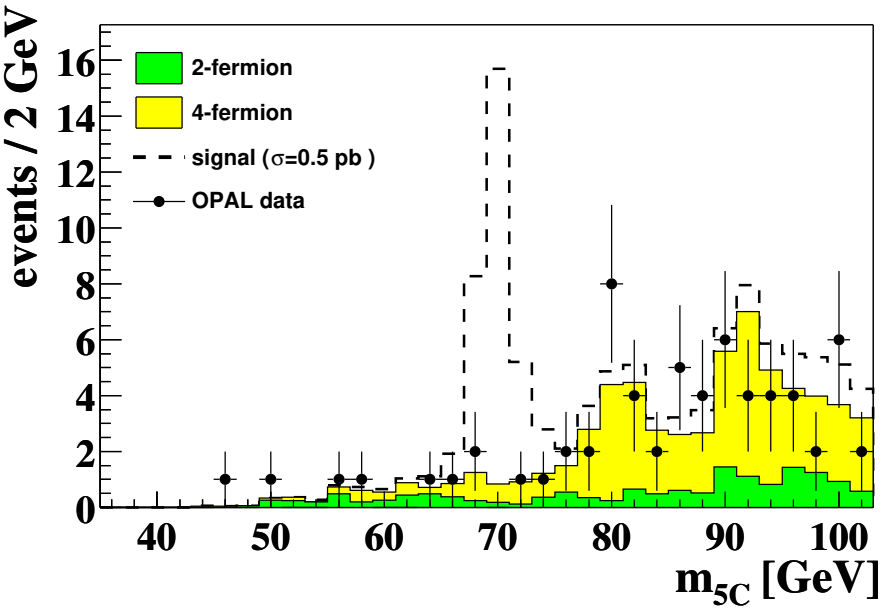

Figure 5.12: *The invariant 5–C fit di-jet mass distribution after the likelihood selection in the* $e^+e^- \to \rho_T^0/\omega_T \to \pi_T^+\pi_T^- \to b\bar{q}\bar{b}q'$ *search channel. The points with error bars are data, the dark grey (green) histogram is* $q\bar{q}(\gamma)$ *background and the light grey (yellow) histogram is four–fermion background. The dashed line added on top of the SM background shows a signal distribution for* $m_{\pi_T} = 70\,\mathrm{GeV}$ *and an assumed cross–section of 0.5* pb*. All Monte Carlo distributions are normalised to the integrated luminosity of the data, 209.4* pb^{-1}*.*

the reconstruction of secondary vertices are d_0, z_0 and ϕ_0, see section 3.2. To study their influence on the result of the analysis the resolution for these three track parameters is varied within $\pm 5\,\%$. It is known from calibration data that the detector simulation describes these track parameters better than the assumed errors [76].

Efficiency of the silicon microvertex detector (SI)

The number of hits in the silicon microvertex detector assigned to a track has a large influence on the reconstruction quality of the track. The errors on the track parameters usually decrease with the number of hits. Thus, mismodelling of the number of hits in the microvertex detector might again spoil the correct simulation of jets originating from b–quarks as described in the previous paragraph. To incorporate the known error [77] on the efficiency of the microvertex detector into a systematic uncertainty, the analysis is repeated with ignoring a fraction of hits in the SI according to the error on the SI efficiency.

Simulation of B– and D–hadrons

Important parameters for the simulation of B–hadrons are their energy spectrum and decay multiplicity. A shift in the assumed energy spectrum to higher energies will lead to a larger average decay length. A larger decay multiplicity makes it easier to reconstruct secondary vertices. Thus, both parameters have an influence on the identification of b–

variable	⟨data⟩	⟨MC⟩	bgnd.	eff.
$\sqrt{s'}/\sqrt{s}$	0.6641	0.6664	0.1 %	0.1 %
y_{43}	4.438×10^{-3}	4.486×10^{-3}	0.1 %	0.2 %
$C_{\rm par}$	0.7167	0.7267	0.3 %	0.2 %
$Q_{di-jet} \times \cos(\theta_{di-jet})$	–	–	4.2 %	4.7 %
$\cos(\theta_{thrust})$	–	–	0.1 %	0.1 %
$\cos(\alpha_{min})$	–	–	0.7 %	0.9 %
$E_{max} - E_{min}$	–	–	0.4 %	2.2 %

Table 5.7: *The systematic uncertainties resulting from improper modelling of the MC description for the variables used in the* $e^+e^- \to \rho_T^0/\omega_T \to \pi_T^+\pi_T^-$ *selection. For the preselection variables the mean value of the corresponding distributions are stated for data and background MC respectively. The resulting relative systematic uncertainties on the Standard Model background (bgnd.) and the signal selection efficiency (eff.) are listed in the last two columns.*

jets. To quantify these influences, their values are varied within the errors quoted for their measurements [78].

This variation is also done for the energy spectrum of D–hadrons. Since they might be wrongly identified as B–hadrons, their modelling also has an influence on the selection.

Kinematic fits

The modelling of the energy and angular resolution of the reconstructed jets in the applied kinematic fits have an influence on their χ^2–probability. Mismodelling in these quantities may lead to wrongly reconstructed jet energies and incorrect χ^2–probability distributions. To estimate the influence of the assumed error on the jet energy, it is varied within 7 %. The errors on the jet parameters ϕ and θ are varied within 4 % [77].

Monte Carlo generators

To quantify the influence of different fragmentation schemes, cluster fragmentation [49] has been applied to the four–fermion background MC sample instead of the standard string fragmentation implemented in [45]. The difference to the standard algorithm is assigned as a systematic error on the Standard Model background prediction.

The uncertainty in the total four–fermion cross–section is taken to be 2.0 % [79].

Total systematic uncertainty

The results of the systematic studies described above are summarised in Table 5.8. The sources of uncertainties are assumed to be independent and therefore the different contributions are added quadratically.

The total systematic uncertainty on the predicted Standard Model background is 10.8 % and on the signal selection efficiency 5.8 %. The largest contribution for the signal efficiency comes from improper modelling of the variables used in the likelihood selection. For the background the uncertainties in the track reconstruction have the strongest

influence. The statistical uncertainties are also quoted but are much smaller than the systematic ones.

source	selection eff.	background
modelling of variables	5.3 %	4.3 %
track reconstruction	2.1 %	7.4 %
SI efficiency	0.8 %	4.8 %
modelling of B–/D–hadrons	0.9 %	1.4 %
kinematic fits	0.3 %	2.2 %
MC generators	–	3.6 %
total syst.	5.8 %	10.8 %
MC statistic	1.5 %	2.8 %

Table 5.8: *Summary of systematic uncertainties in the* $e^+e^- \to \rho_T^0/\omega_T \to \pi_T^+\pi_T^-$ *search channel. The values are the relative uncertainties. In the last line the statistical error due to limited MC samples are also quoted.*

5.5 Search in the $e^+e^- \to \rho_T^0/\omega_T \to \pi_T^\pm W_L^\mp$ Channel

In this section the search for charged technipions produced in association with charged weak gauge bosons is described. Only hadronic decays of the $W^\pm$ bosons are considered in the following. The corresponding Feynman diagram is shown in Figure 5.13.

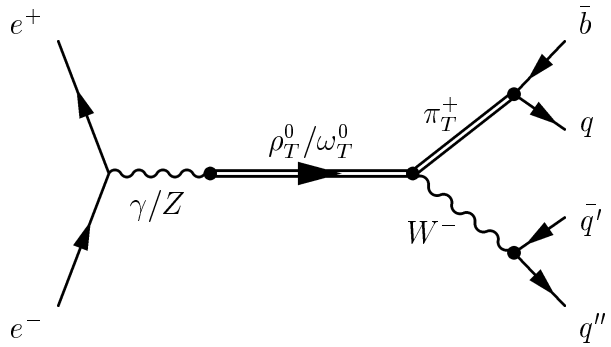

Figure 5.13: *The Feynman diagram of the* $e^+e^- \to \rho_T^0/\omega_T \to \pi_T^+ W_L^- \to \bar{b}q\bar{q}'q''$ *channel.*

As in the $e^+e^- \to \rho_T^0/\omega_T \to \pi_T^+\pi_T^- \to b\bar{q}\bar{b}q'$ channel, the process is characterised by four well separated jets and large visible energy. In contrast to the previous channel, only one of the jets originates from a b–quark. This statement is true when neglecting the very small fraction of $W^+ \to \bar{b}c$ decays. A typical candidate event detected by OPAL is displayed in Figure 5.14.

The two jets originating from the $W^\pm$ have an invariant mass of $\approx 81\,\text{GeV}$. This information is used in the 5–C kinematic fit where one invariant di–jet mass is constrained

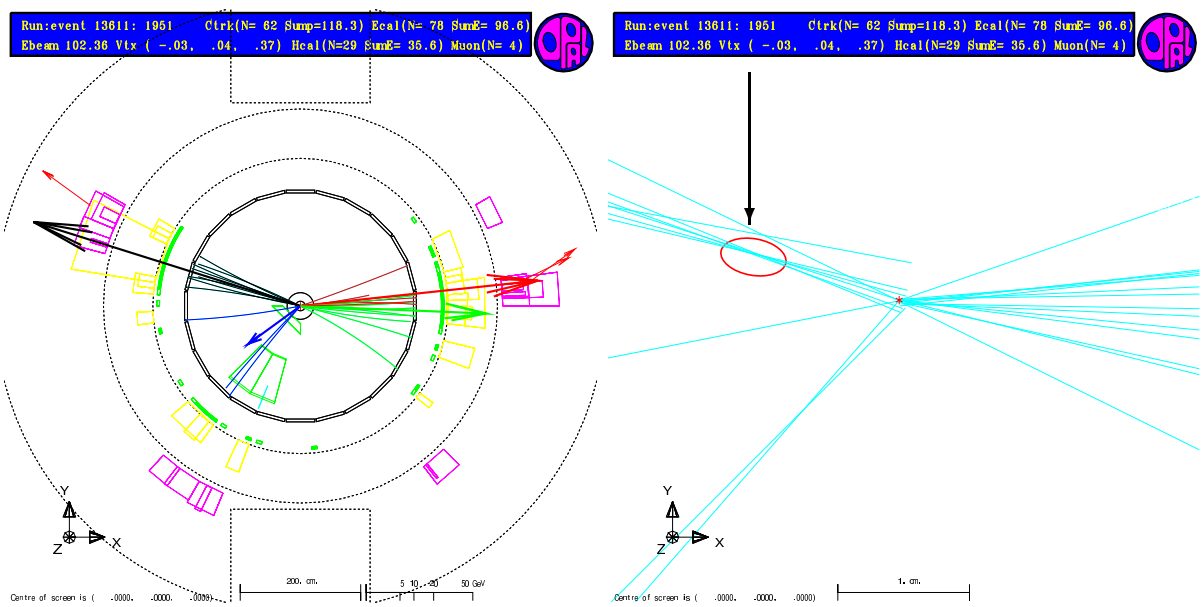

Figure 5.14: *A candidate event in the year 2000 data detected by* OPAL. *The four jets are well separated in space. This can be seen when taking also the z–component of the jets momenta into account. The close–up picture of the interaction–point shows a secondary vertex in one of the four jets (arrow).*

to the $W^{\pm}$ mass. The assignment of jets to bosons is accomplished with a likelihood method described in the next section. The invariant mass of the jet pair not assigned to the $W^{\pm}$ is then interpreted as the mass of the hypothetical charged technipion. The angular distribution of the produced initial bosons is the same as in the $e^+e^- \to \rho_T^0/\omega_T \to \pi_T^+\pi_T^- \to b\bar{q}\bar{b}q'$ channel, characterised by Eq. 5.4.

5.5.1 Jet Pairing

The assignment of the four jets to the $\pi_T^{\pm}$ and $W^{\pm}$ respectively is accomplished with a likelihood method distinguishing between two classes: 1. the correct and 2. all wrong assignments of the jets to the bosons. Six jet combinations are possible which are listed in Table 5.9. Two input variables are used to calculate a likelihood $\mathcal{L}_{JC}$ for a certain assignment of jets to bosons. They utilise two characteristic properties of the signal topology:

- The two jets originating from the $W^{\pm}$ have an invariant di–jet mass of $\approx$ 81 GeV. A 5–C kinematic fit is applied constraining these two jets to have an invariant di–jet mass of m_W. The logarithm of the χ^2–fit probability serves as the first input variable.

- The b–quark adherent in the signal topology is assumed to originate from the charged technipion. Combinations where the jet with the highest b–likelihood is assigned to the $W^{\pm}$ should therefore be disfavoured. A quantity $\mathcal{R}$ is formed to describe this requirement mathematically:

$$\begin{aligned}\mathcal{R} &= \max\{\mathcal{B}(\pi_{jet\ 1}), \mathcal{B}(\pi_{jet\ 2})\} \times (1 - \min\{\mathcal{B}(\pi_{jet\ 1}), \mathcal{B}(\pi_{jet\ 2})\}) \\ &\quad \times (1 - \mathcal{B}(W_{jet\ 1})) \times (1 - \mathcal{B}(W_{jet\ 2})).\end{aligned}$$

  Here $\mathcal{B}(X_{jet\ i})$ is the b–likelihood of jet i associated with the boson X. $\mathcal{R}$ has its maximal value when the jet with the highest b–likelihood is assigned to the charged technipion.

The probability density functions used to calculate the likelihood for each of the six jet combinations are shown in Figure 5.15.

$\mathcal{L}_{JC}$ is calculated for each of these combinations. The combination which yields the highest value in $\mathcal{L}_{JC}$ is assumed further when calculating the input variables for the likelihood selection described in the next section.

$W^{\pm}$	$\pi_T^{\pm}$
(12)	(34)
(13)	(24)
(14)	(32)
(34)	(12)
(24)	(13)
(23)	(14)

Table 5.9: *The six possibilities for assigning the jets (numbered from* $1, \ldots, 4$*) to the charged technipion and the* $W^{\pm}$ *in the* $e^+e^- \to \rho_T^0/\omega_T \to \pi_T^+ W_L^- \to \bar{b}q\bar{q}'q''$ *channel.*

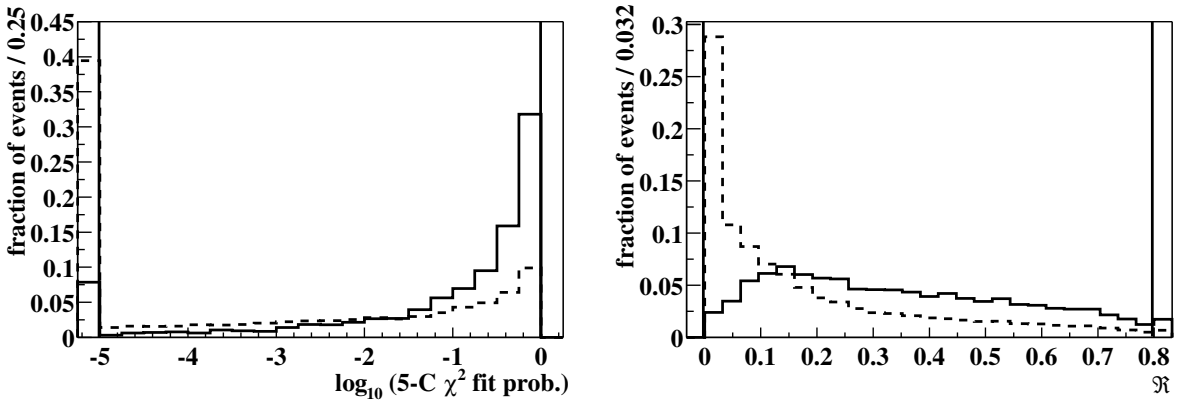

Figure 5.15: *The normalised probability density functions for the two variables used to determine the correct assignment of the jets to the bosons in the* $e^+e^- \to \rho_T^0/\omega_T \to \pi_T^\pm W_L^- \to \bar{b}q\bar{q}'q''$ *channel. The probability density functions for the correct assignment are drawn as solid lines whereas the ones for wrong combinations are dashed. Vertical lines in the histograms separate the under– and overflow bins.*

5.5.2 Likelihood Selection

The likelihood selection used in the $e^+e^- \to \rho_T^0/\omega_T \to \pi_T^+ W_L^- \to \bar{b}q\bar{q}'q''$ channel is based on four variables. The first three are the same as in the $e^+e^- \to \rho_T^0/\omega_T \to \pi_T^+\pi_T^- \to b\bar{q}\bar{b}q'$ channel and are described in section 5.4.1.

1. The cosine of the di–jet production angle $\cos(\theta_{di-jet})$ multiplied by the di–jet charge, Q_{di-jet}. The grouping of the four jets into two di–jets is accomplished with the likelihood method described in the previous section.

2. The cosine of the polar angle of the thrust axis $\cos(\theta_{thrust})$.

3. The b–likelihood of the jet with the highest b–likelihood in the event.

4. The WW matrix element as calculated in [80]. Here the value of the matrix element for $W^+W^- \to u\bar{d}\bar{u}d$ is calculated from the reconstructed jet momenta. Energy and momentum conservation is ensured by using the jet momenta after the 4–C fit as input.

The normalised probability density functions for the signal and the two background classes are shown in Figure 5.16. The signal probability density functions are averaged over the whole range of charged technipion masses considered in this search channel. As in the previous channel, the b–likelihood variable has the highest discriminative power.

Figure 5.17 shows the comparison between the OPAL data of the year 2000 and the Monte Carlo prediction in the four likelihood variables. The expected distributions for a signal with an assumed charged technipion mass of 100 GeV and a cross–section of 5 pb are also included. Good agreement between data and Monte Carlo is observed.

The resulting likelihood distribution for the signal class is shown in Figure 5.18. The Monte Carlo distributions are normalised to the data luminosity. A signal for $m_{\pi_T^\pm} = 100\,\text{GeV}$ with a cross–section of 1 pb is included. The agreement between data

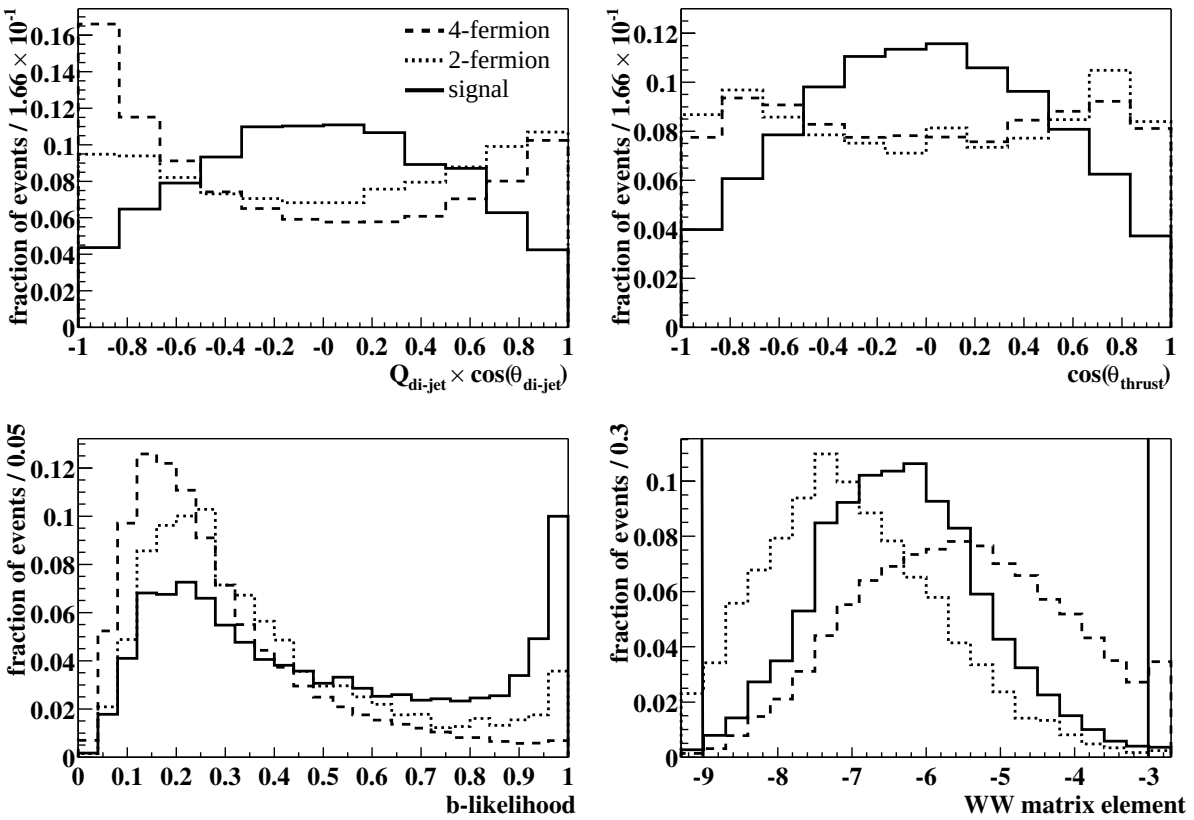

Figure 5.16: *The probability density functions for the four likelihood variables used in the* $e^+e^- \to \rho_T^0/\omega_T \to \pi_T^+ W_L^- \to \bar{b}q\bar{q}'q''$ *selection. All distributions are normalised to unity. The three classes defined are four–fermion background (dashed),* $q\bar{q}(\gamma)$ *background (dotted), and the signal class (line). The signal distributions are averaged over the whole range of charged technipion masses from 50* GeV *up to 125* GeV*. Vertical lines in the histograms separate under– and overflow bins if they have non–vanishing contents.*

and Monte Carlo in the likelihood distribution is good and no obvious signal is manifest.

Events with a signal likelihood of larger than 0.55 are selected as candidate events. This cut on the likelihood is determined by optimising the expected exclusion limit for an $e^+e^- \to \rho_T^0/\omega_T \to \pi_T^+ W_L^- \to \bar{b}q\bar{q}'q''$ signal. Expected exclusion limits for different cuts on the signal likelihood are shown in Figure 5.19. They are obtained with the method described in section 6.1.3.

When applying the cut on the signal likelihood, the following number of events is expected and selected respectively:

$\mathcal{L} > 0.55$				
data	total background	$q\bar{q}(\gamma)$ bgnd.	4–f ZZ bgnd.	4–f WW bgnd.
138	127.2 ± 1.9	29.0	26.2	72.0

The error on the total expected Standard Model background is purely statistical. The background is dominated by four–fermion events where the production via a pair of $W^\pm$ bosons dominates. This is expected due to the signal–like topology of these events.

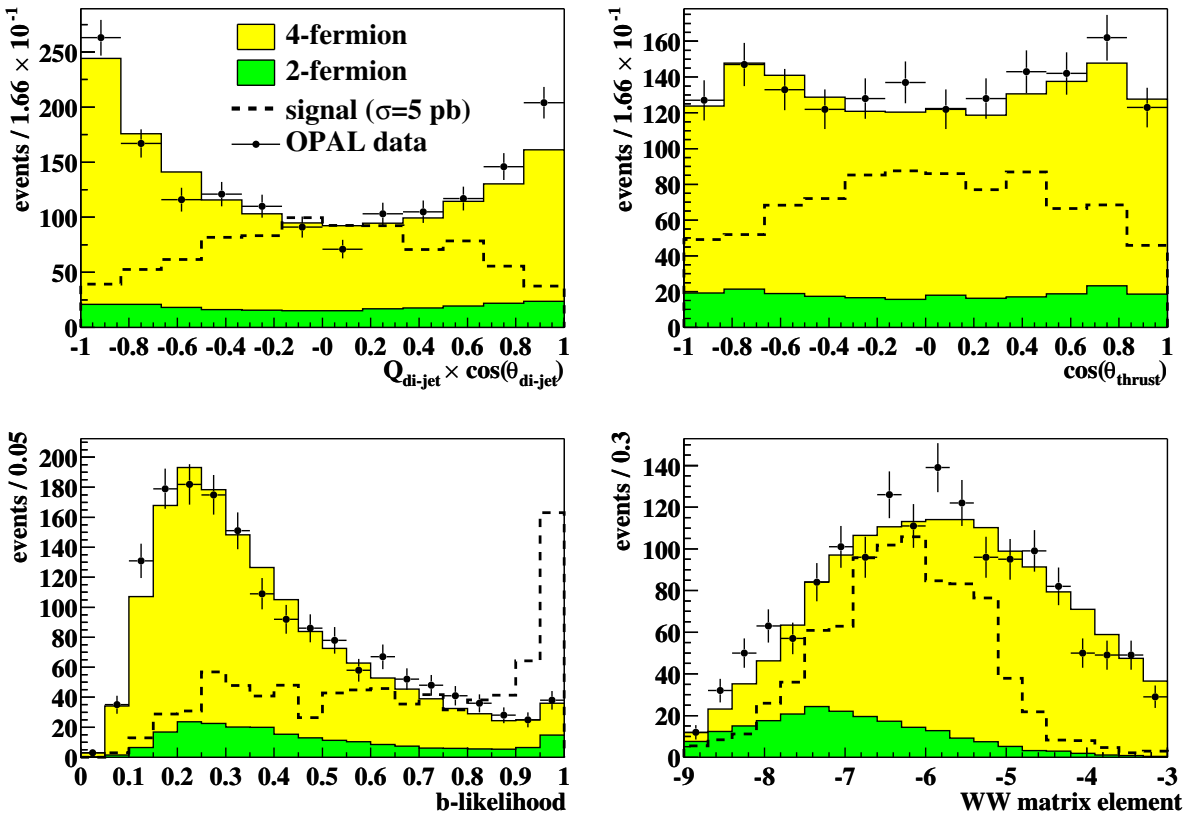

Figure 5.17: *Distributions of the four likelihood variables used in the search for* $e^+e^- \to \rho_T^0/\omega_T \to \pi_T^+ W_L^- \to \bar{b}q\bar{q}'q''$. *The points with error bars are data, the dark grey (green) histograms are* $q\bar{q}(\gamma)$ *background on top of which four–fermion background is added in light grey (yellow). The distributions from background Monte Carlo are normalised to the data luminosity of 209.4* pb^{-1}. *Included is a signal distribution for* m_{π_T} *= 100* GeV *and an assumed cross–section of 5* pb *(dashed).*

The selection efficiencies for different charged technipion masses are shown in Figure 5.20 (a). They are interpolated with a spline to assure the correct modelling of the decrease in selection efficiency around the mass of the $W^\pm$. Here the signal has a topology which is very similar to the Standard Model background originating from a pair of $W^\pm$ bosons. Especially the WW matrix element's discriminative power decreases. The jet–combination efficiencies for different charged technipion masses are shown in Figure 5.20 (b).

Figure 5.21 shows the reconstructed mass distribution for selected events. Also in the mass distribution no significant deviations between data and expected Standard Model background are visible. A signal distribution, corresponding to $m_{\pi_T} = 100$ GeV and an assumed cross–section of 1 pb is also included.

The four–fermion background clusters dominantly at reconstructed masses around the $W^\pm$ mass with only small contributions from events with reconstructed masses around the Z mass. The tails to lower and higher masses in the four–fermion background distribution are due to combinatorial background where the assignment of jets to bosons is wrong. As in the $e^+e^- \to \rho_T^0/\omega_T \to \pi_T^+\pi_T^- \to b\bar{q}\bar{b}q'$ search channel, the $q\bar{q}(\gamma)$ reconstructed mass distribution is rather flat.

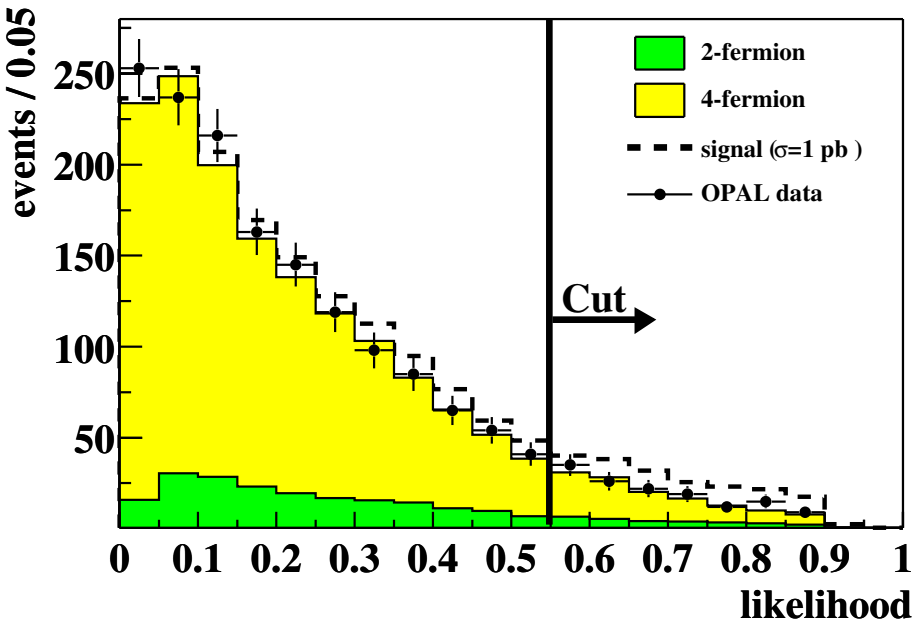

Figure 5.18: *The signal likelihood distribution in the* $e^+e^- \to \rho_T^0/\omega_T \to \pi_T^+ W_L^- \to \bar{b}q\bar{q}'q''$ *search channel. The points with error bars are data, the dark grey histogram (green) is* $q\bar{q}(\gamma)$ *background and the light grey (yellow) histogram is four–fermion background. The dashed line added on top of the SM background shows a signal distribution for* $m_{\pi_T} = 100\,GeV$ *and an assumed cross–section of 1 pb. All Monte Carlo distributions are normalised to the integrated luminosity of the data,* $209.4\,pb^{-1}$.

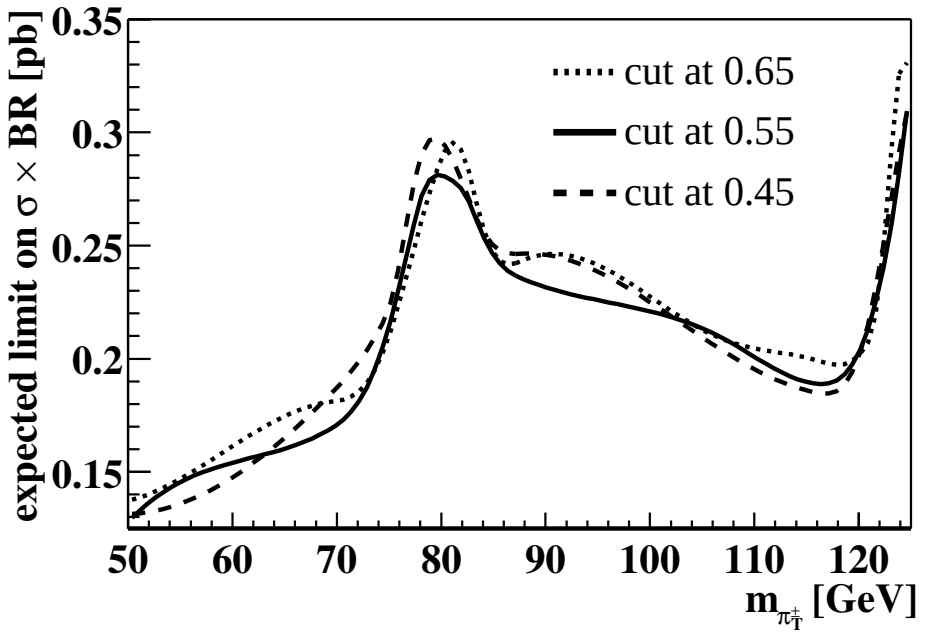

Figure 5.19: *Expected* $\sigma(e^+e^- \to \rho_T^0/\omega_T \to \pi_T^+ W_L^- \to \bar{b}q\bar{q}'q'')$ *exclusion limits for different cuts on the signal likelihood.*

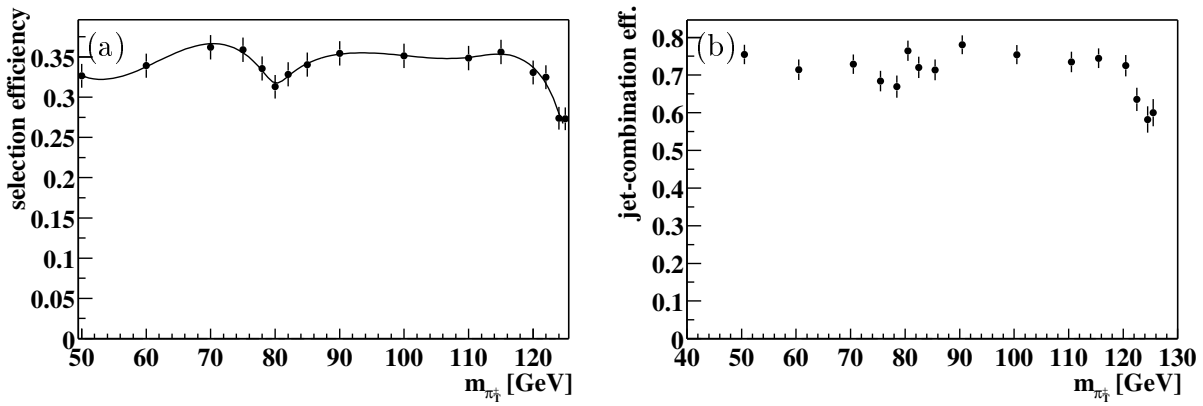

Figure 5.20: *(a) Selection efficiencies in the* $e^+e^- \to \rho_T^0/\omega_T \to \pi_T^+ W_L^- \to \bar{b}q\bar{q}'q''$ *search channel for charged technipion masses where MC samples are available. The selection efficiency is interpolated with a spline. (b) Jet–combination efficiencies for selected events in the* $e^+e^- \to \rho_T^0/\omega_T \to \pi_T^+ W_L^- \to \bar{b}q\bar{q}'q''$ *channel at different charged technipion masses.*

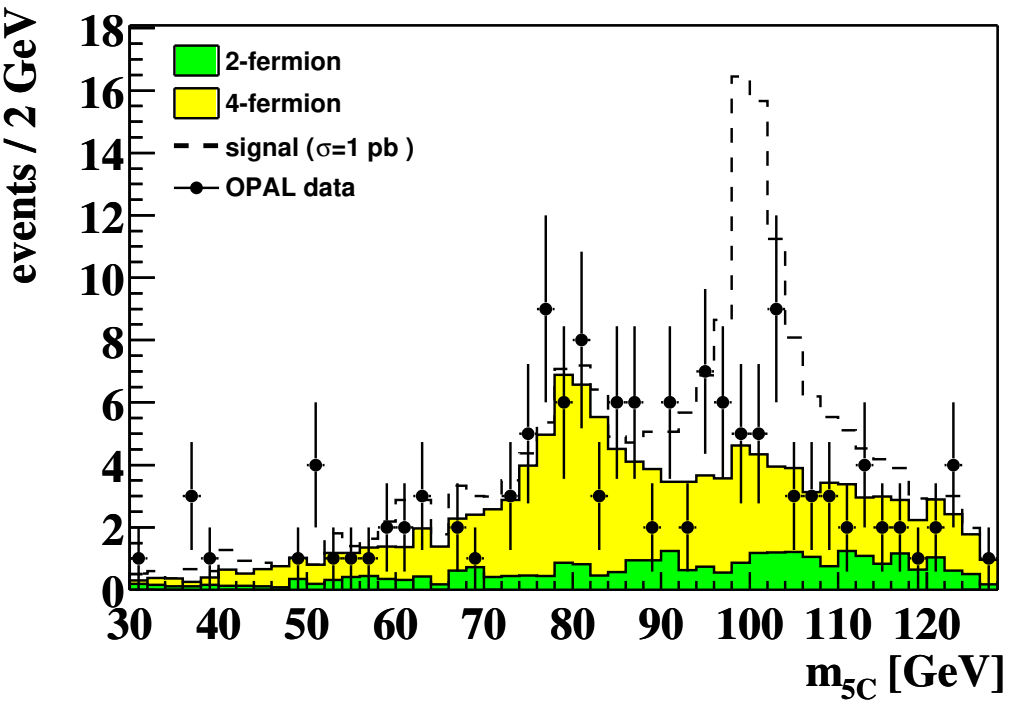

Figure 5.21: *The invariant 5–C fit di–jet mass distribution after the likelihood selection in the* $e^+e^- \to \rho_T^0/\omega_T \to \pi_T^+ W_L^- \to \bar{b}q\bar{q}'q''$ *search channel. The points with error bars are data, the dark grey (green) histogram is* $q\bar{q}(\gamma)$ *background and the light grey (yellow) histogram is four–fermion background. The dashed line added on top of the SM background shows a signal distribution for* $m_{\pi_T} = 100\,\text{GeV}$ *and an assumed cross–section of* 1 pb. *All Monte Carlo distributions are normalised to the integrated luminosity of the data,* $209.4\,pb^{-1}$.

variable	⟨data⟩	⟨MC⟩	bgnd.	eff.
$\sqrt{s'}/\sqrt{s}$	0.6641	0.6664	0.1 %	0.0 %
y_{43}	4.438×10^{-3}	3.791×10^{-3}	2.9 %	2.2 %
C_{par}	0.7041	0.7127	0.5 %	0.3 %
$Q_{di-jet} \times \cos(\theta_{di-jet})$	–	–	4.0 %	3.9 %
$\cos(\theta_{thrust})$	–	–	1.6 %	1.4 %
WW matrix element	–	–	0.7 %	0.4 %

Table 5.10: *Systematic uncertainties resulting from improper modelling of the MC description for the variables used in the* $\mathrm{e^+e^-} \to \rho_T^0/\omega_T \to \pi_T^{\pm}\mathrm{W_L^{\mp}}$ *selection. For the preselection variables the mean value of the corresponding distributions are stated for data and background MC respectively. The resulting relative systematic uncertainties on the Standard Model background (bgnd.) and the signal selection efficiency (eff.) are listed in the last two columns.*

source	selection eff.	background
modelling of variables	4.7 %	5.3 %
track reconstruction	1.8 %	5.4 %
SI efficiency	1.5 %	1.1 %
modelling of B–/D–hadrons	1.4 %	0.5 %
kinematic fits	0.9 %	1.5 %
MC generators	–	2.9 %
total syst.	5.5 %	8.3 %
MC statistic	1.5 %	1.5 %

Table 5.11: *Summary of systematic uncertainties in the* $\mathrm{e^+e^-} \to \rho_T^0/\omega_T \to \pi_T^{\pm}\mathrm{W_L^{\mp}}$ *search channel. The values are the relative uncertainties. In the last line the statistical error due to limited MC samples are also quoted.*

The event in the highest mass bin is the reason why Standard Model Monte Carlo has to be produced also at $\sqrt{s} = 208\,\mathrm{GeV}$ to estimate the expected background in this bin. The obtained background prediction turns out to be consistent with the one observed event.

Again the reconstructed mass distributions are used to set limits on the production cross–section and to exclude regions in the TCSM parameter space, cf. section 6.2.

5.5.3 Systematic Uncertainties

The same sources of systematic uncertainties as exploited in the $\mathrm{e^+e^-} \to \rho_T^0/\omega_T \to \pi_T^+\pi_T^- \to b\bar{q}\bar{b}q'$ channel are considered here. For the description of the individual errors see section 5.4.2. The systematic uncertainties from the modelling of the pre– and likelihood selection variables are summarised in Table 5.10.

Table 5.11 lists all considered systematic uncertainties. The total systematic uncertainty sums up to 8.3% for the expected Standard Model background and to 5.5% for the signal selection efficiency. For the signal selection efficiency the uncertainty due to

the modelling of the topological variables used in the selection process has the largest influence. The largest contribution to the background comes in equal parts from the modelling of the topological variables and the uncertainties in the track reconstruction. The statistical uncertainties are small compared to the systematic ones.

Chapter 6

Interpretation of Results

The non–observation of any excess in the searches for Technicolor production allows limits to be set on the cross–section $\times$ branching ratio for the processes under consideration. These are interpreted in the framework of the TCSM in order to exclude regions in the $(m_{\rho_T/\omega_T}, m_{\pi_T})$ plane.

The first part of this chapter describes how limits at a certain confidence level (CL) are obtained with the method described in [81]. The second part describes the interpretation of the obtained cross–section $\times$ branching ratio limits within the Technicolor Straw Man Model.

6.1 Limit Calculation

This section describes how an exclusion limit is obtained at a desired confidence level (CL). In the first part the general idea of confidence levels for a simple counting experiment is introduced. The profit of introducing a test statistic when combining several counting experiments is clarified. How systematic uncertainties on the background– and signal expectation influence the observed exclusion limit and how these influences are handled in this analysis is described in the last part of this section.

6.1.1 Confidence Levels

The concept of an exclusion limit at a certain confidence level (CL) is introduced here for a simple counting experiment. The output of such an experiment is three numbers:

- b: the predicted number of background events.
- $s+b$: the predicted number of events which would be observed if a signal is present in addition to the expected background.
- d: the observed number of events.

If a certain number of events d is observed in the experiment, the task is to decide whether this outcome favours the presence of a signal (the signal–plus–background hypothesis, s+b) or the background–only hypothesis, b. If the background–only hypothesis is favoured,

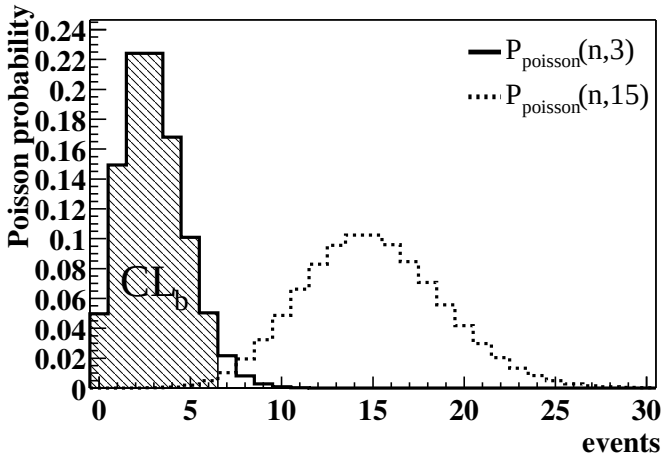

Figure 6.1: *The Poisson distributions for the expected number of observed events for the signal– plus background hypothesis ($P_{\mathrm{Poisson}}(n, 15)$) and the background–only hypothesis ($P_{\mathrm{Poisson}}(n, 3)$). The shaded area corresponds to* $\mathrm{CL_b}$.

as it is the case for the two searches described in this analysis, the confidence level at which the signal hypothesis can be excluded is of essential interest.

Under the assumption of no signal present in the data, the outcomes n of many (N $\rightarrow \infty$) counting experiments are distributed according to the Poisson statistic with a mean expected number of observed events b:

$$P_{\mathrm{Poisson}}(n, b) = \frac{e^{-b}\ b^n}{n!}. \tag{6.1}$$

If on the other hand a signal is present, n would be distributed according to a Poisson distribution with a mean expected number of observed events $s + b$:

$$P_{\mathrm{Poisson}}(n, s+b) = \frac{e^{-(s+b)}\ (s+b)^n}{n!}. \tag{6.2}$$

These two Poisson distributions are shown in Figure 6.1. Here $b = 3$ and $s + b = 15$ are assumed. Additionally it is assumed that $d^{\mathrm{obs}} = 6$ was measured in a certain counting experiment. At what confidence level can the signal–plus–background $(s + b)$ hypothesis be excluded?

Two quantities, $\mathrm{CL_b}$ and $\mathrm{CL_{s+b}}$, are defined as follows:

$$\mathrm{CL_b} = \sum_{n=0}^{d^{\mathrm{obs}}} P_{\mathrm{Poisson}}(n, b) \tag{6.3}$$

$$\mathrm{CL_{s+b}} = \sum_{n=0}^{d^{\mathrm{obs}}} P_{\mathrm{Poisson}}(n, s+b). \tag{6.4}$$

$\mathrm{CL_b}$ is the fraction of experiments which would result in the same or fewer events observed than d^{obs} if the background–only hypothesis is true. In the same manner $\mathrm{CL_{s+b}}$ represents the fraction of experiments which would result in the same or fewer observed events than d^{obs} if the signal–plus–background hypothesis is true [81]:

$$\mathrm{CL_b} = P_b(n \leq d^{\mathrm{obs}}) \tag{6.5}$$

$$\mathrm{CL_{s+b}} = P_{s+b}(n \leq d^{\mathrm{obs}}). \tag{6.6}$$

To quantify the confidence at which a signal can be excluded, commonly the number CL_s is defined as [81]:

$$CL_s = \frac{CL_{s+b}}{CL_b}. \tag{6.7}$$

A signal is then said to be excluded with a confidence of $1 - CL_s$. The example given above yields an exclusion of the signal hypothesis at the 99.2 % CL. If the mean expected number of events for the $s + b$ hypothesis depends on one or more parameters (such as cross–sections, branching ratios, etc...) usually the exclusion limit for these parameters is quoted at the 95 % CL, i.e. the set of parameters is quoted for which $1 - CL_s = 95\,\%$.

6.1.2 Combining Search Channels, Test Statistic

Interpreting the results obtained for each search channel, described in the sections 5.4.1 and 5.5.2, as simple counting experiments would not exploit all accessible information. Especially the obtained reconstructed mass distributions for the expected signal and background distributions (see Figures 5.12 and 5.21) help to discriminate the background–only from the signal–plus–background hypothesis significantly. The signal–plus–background hypothesis for charged technipions at different masses can be distinguished by the position of the peak in the expected signal mass distribution. To utilise this information, each bin in the mass distribution is considered as a counting experiment on its own. The combination of the channels is accomplished with the help of a test statistic as suggested in [81].

A test statistic Q is a quantity which discriminates signal–like outcomes from background–like ones. An optimal choice for the test statistic is the likelihood ratio defined as [81]:

$$Q(n) = \frac{P_{\text{Poisson}}(n, s+b)}{P_{\text{Poisson}}(n, b)} = \frac{e^{-s}(s+b)^n}{b^n}, \tag{6.8}$$

where b and s are the best estimates for the expected number of background and signal events respectively. The test statistic is an observable of an experiment. Once b and s are determined, usually by Monte Carlo techniques, Q depends only on the number of observed events n.

Instead of considering the Poisson distribution of observed events when calculating the exclusion limit, the distributions in Q are used. For technical reasons usually the distributions are calculated in $-2\ln(Q)$. The test statistic distributions for the example given in the last section are shown in Figure 6.2.

CL_b, CL_{s+b} and CL_s are redefined with respect to the test statistic Q. If the distribution of Q is given by $pdf_b(Q)$ for the background–only hypothesis and by pdf_{s+b} for the signal–plus–background hypothesis, then:

$$CL_b = \sum_{Q \le Q^{\text{obs}}} pdf_b(Q) \tag{6.9}$$

$$CL_{s+b} = \sum_{Q \le Q^{\text{obs}}} pdf_{s+b}(Q). \tag{6.10}$$

For the example considered above $-2\ln(Q^{\text{obs}}) \approx 4.69$ and the signal–plus–background hypothesis can be excluded again at the $1 - CL_s = 1 - (CL_{s+b}/CL_b) = 99.2\,\%$ confidence level.

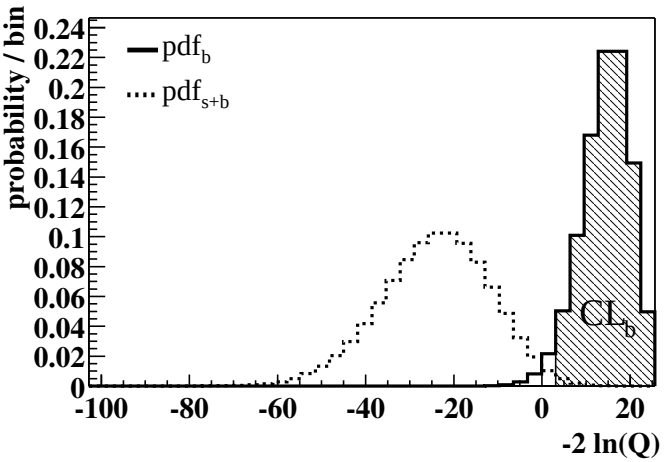

Figure 6.2: *The probability distributions for observing a test statistic Q for the example given in section 6.1.1. It is* $-2\ln(Q^{\mathrm{obs}}) \approx 4.69$ *and the shaded area again corresponds to* $\mathrm{CL_b}$, *cf. Figure 6.1.*

The benefit of introducing the likelihood ratio as a test statistic becomes clear when combining several search channels. It has the property that the joint test statistic for the outcome of many channels is the product of the test statistics of each channel separately:

$$Q^{\mathrm{tot}} = \prod_{i=1}^{N_{\mathrm{chan}}} Q_i. \tag{6.11}$$

Here N_{chan} is the total number of channels and Q_i is defined according to Eq. 6.8:

$$Q_i(n_i) = \frac{e^{-s_i}(s_i + b_i)^{n_i}}{b_i^{n_i}}. \tag{6.12}$$

When calculating the logarithm of Eq. 6.11 one obtains:

$$\ln(Q^{\mathrm{tot}}) = -s_{\mathrm{tot}} + \sum_{i=1}^{N_{\mathrm{chan}}} n_i \ln\left(1 + \frac{s_i}{b_i}\right), \tag{6.13}$$

i.e. the observed number of events in each channel is weighted with the signal over background ratio in this channel. When interpreting each bin in the reconstructed mass distribution as an individual counting experiment the bins under the mass peak expected from a signal gain a higher weight compared to bins far from this region of interest. Hence the sensitivity of the combined test statistic is adjusted to the considered charged technipion mass hypothesis.

6.1.3 Expected Exclusion Limit

The expected exclusion limit states how many signal events can be expected to be excluded at the 95 % CL assuming that no signal is present in the data. In this analysis a Monte Carlo approach is used to calculate pdf_b and pdf_{s+b} as implemented in [82]. pdf_b is approximated by evaluating Eq. 6.13 $N_{\mathrm{MC}} = 100000$ times. Each time the assumed number of "observed" events in each channel $n_i,\ i = 1, \ldots, N_{chan}$ is taken from an ensemble

of hypothetical outcomes $\{n_j\}_i$, $j = 1, \ldots, N_{\mathrm{MC}}$, where the n_j are distributed according to a Poisson distribution with a mean expected number of b_i events, $P_{\mathrm{Poisson}}(n_i, b_i)$. pdf_{s+b} is computed accordingly. The median of pdf_b is then assumed to be the test statistic corresponding to the number of events which would be observed if no signal is present in the data. $\mathrm{CL_s}$ and $\mathrm{CL_{s+b}}$ are calculated according to Eq. 6.9 and Eq. 6.10 with $Q^{\mathrm{obs}}_{\mathrm{exp}} = \mathrm{median}(pdf_b)$.

In the two search channels considered in this analysis, the expected total number of signal events depends on the production cross–section in each channel and on the branching ratios to the considered final states. Therefore limits are quoted for the cross–section × branching ratio at the 95 % CL. Figures 5.10 and 5.19 show expected exclusion limits for different cuts on the signal likelihood distribution and the analyses are optimised using the expected cross–section × branching ratio exclusion limit as a figure of merit.

6.1.4 Handling of Systematic Uncertainties

The influence of uncertainties in the expected number of signal and background events is incorporated in the computation of the exclusion limits [82]. Since the test statistic is an observable, the uncertainties do not affect the observed test statistic Q^{obs}. Nevertheless, the distributions of the test statistics under the assumption of the background–only and signal–plus–background hypothesis, pdf_b and pdf_{s+b} are affected. The mean expected number of events governing the Poisson distribution of the test samples $\{n_j\}_i$ is not precisely known due to the systematic uncertainties. Therefore the mean expected values are varied within the systematic errors assuming a Gaussian distribution. Influences from different sources of uncertainties are treated independently. Full correlation is assumed for the influence of each source of uncertainty for the whole set of bins in the mass distributions. Also the effect one source of uncertainty has on the signal and background expectation is assumed to be fully correlated.

6.2 Exclusion Limits

The observed and expected cross–section × branching ratio exclusion limits at the 95 % CL are shown in Figure 6.3 (a) for the $\mathrm{e^+e^-} \to \rho_T^0/\omega_T \to \pi_T^+\pi_T^- \to b\bar{q}\bar{b}q'$ and in Figure 6.3 (b) for the $\mathrm{e^+e^-} \to \rho_T^0/\omega_T \to \pi_T^+\mathrm{W_L^-} \to \bar{b}q\bar{q}'q''$ search channel. The 1σ– and 2σ–bands around the median expected exclusion limit correspond to the exclusion limits one would expect if $Q^{\mathrm{obs}}_{\mathrm{exp}} = \mathrm{median}(pdf_b)$ fluctuates one resp. two standard deviations upwards resp. downwards. All background and signal mass distributions have been smoothed [83] before being used in the limit calculation. The structures in the observed exclusion limits are due to candidate events in the data. As explained in the previous section, candidate events having a mass of approximately the assumed technipion mass gain a higher weight when evaluating the observed test statistic. Hence regions under the expected signal mass peak with more candidate events than predicted by the expected Standard Model background result in a worse exclusion limit and vice versa.

In the $\mathrm{e^+e^-} \to \rho_T^0/\omega_T \to \pi_T^+\pi_T^- \to b\bar{q}\bar{b}q'$ search channel, cross–section × branching ratios larger than approximately 100 fb can be excluded except for charged technipion masses around the $\mathrm{W^\pm}$ and Z mass. Here the expected Standard Model background is

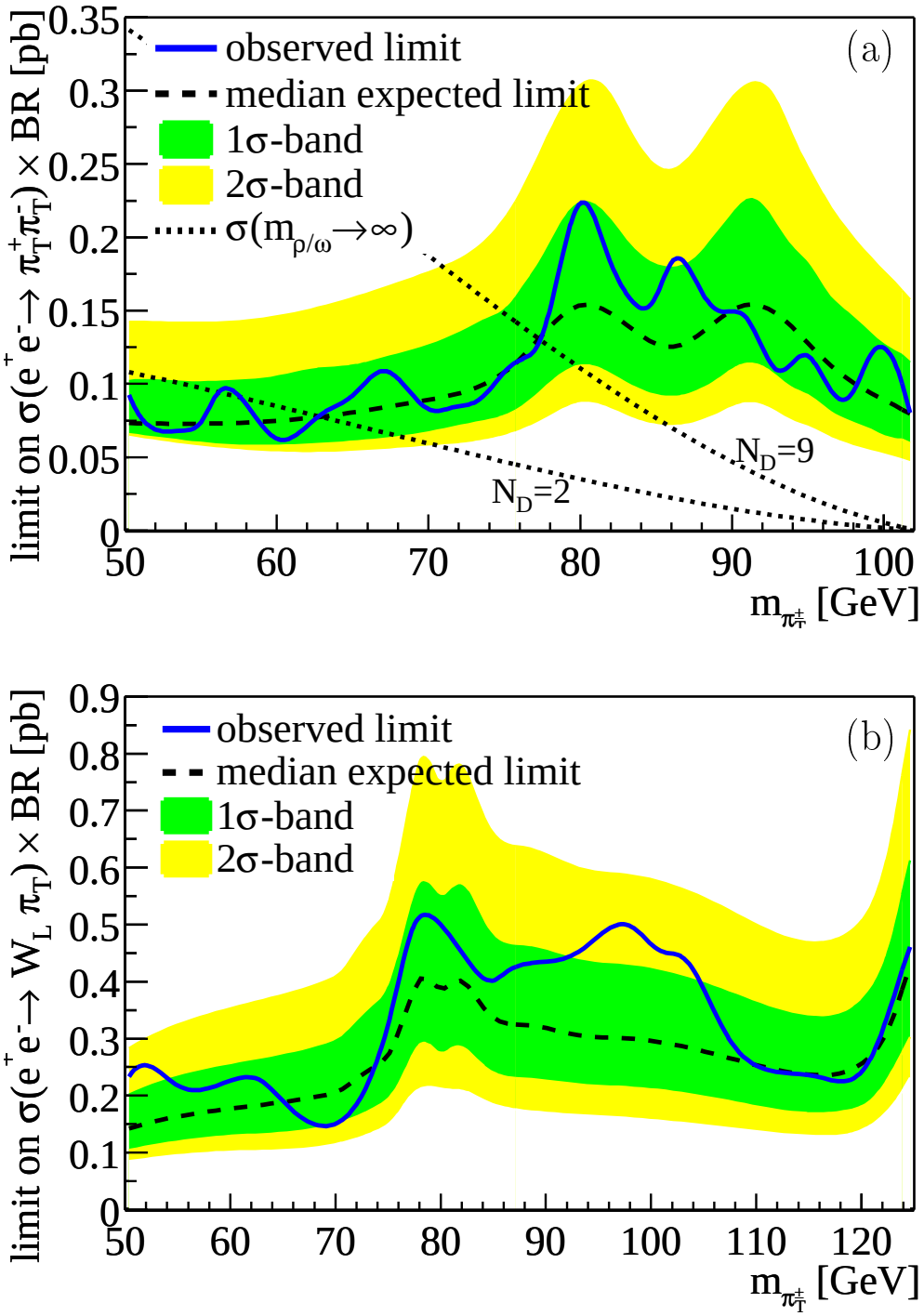

Figure 6.3: *The 95 % CL upper limit on the cross–section for (a)* $e^+e^- \to \rho_T^0/\omega_T \to \pi_T^+\pi_T^- \to b\bar{q}\bar{b}q'$ *and (b)* $e^+e^- \to \rho_T^0/\omega_T \to \pi_T^+ W_L^- \to \bar{b}q\bar{q}'q''$ *production. The solid (blue) curve shows the cross–section limit obtained from the data as a function of the* π_T *mass. The dashed curve shows the median expected limit for the background–only hypothesis. The dark and light grey (green and yellow) bands show the 1–*σ *and 2–*σ *error bands on the median expected limit.*
The cross–sections for the $e^+e^- \to \rho_T^0/\omega_T \to \pi_T^+\pi_T^- \to b\bar{q}\bar{b}q'$ *process with* $m_{\rho_T/\omega_T} \to \infty$ *are included in the upper plot for* N_D*=2 and* N_D*=9 as the dotted lines.*

harder to suppress and an overall upper limit on the cross–section × branching ratio is set to 225 fb. The observed limit stays within the 1σ–band of the median expected limit for all charged technipion masses.

In the $e^+e^- \to \rho_T^0/\omega_T \to \pi_T^+ W_L^- \to \bar{b}q\bar{q}'q''$ search channel the expected Standard Model background is harder to suppress than in the $e^+e^- \to \rho_T^0/\omega_T \to \pi_T^+\pi_T^- \to b\bar{q}\bar{b}q'$ search channel. This results in larger upper limits on the cross–section × branching ratios. An overall upper limit is set to 520 fb. For reconstructed technipion masses between 94 GeV and 104 GeV slightly more events are observed than expected from Standard Model background, cf. Figure 5.21. This results in the deviation of the observed limit from the median expected one in this mass range. Nevertheless, the observed limit always stays within two standard deviations of the median expected limit assuming the background–only hypothesis.

It has been checked that the selection efficiencies of the analyses do not depend on m_{ρ_T/ω_T}. Hence the obtained exclusion limits can be translated directly into excluded regions in the (m_{ρ_T/ω_T}, m_{π_T}) plane, assuming a certain set of TCSM parameters. The ones assumed here are given in Table 2.3. All values for m_{ρ_T/ω_T} and m_{π_T} predicting a larger cross–section for the process under consideration than the upper limit set by this analysis can be excluded at the 95 % CL. Figures 6.4 (a) and 6.4 (b) show the excluded region for each search channel. Both search channels exclude the production of charged technipions up to the kinematic limit for $m_{\rho_T/\omega_T} \approx \sqrt{s}$. Limits can only be set for $m_{\rho_T/\omega_T} \geq \sqrt{s}$ due to the influence of initial state radiation for $m_{\rho_T/\omega_T} < \sqrt{s}$ which has not been studied in this analysis, cf. section 2.3.

When combining the exclusion limits obtained in the two search channels, both are treated as independent searches. Hence a point in the (m_{ρ_T/ω_T}, m_{π_T}) plane is excluded if it is excluded by at least one of the search channels. This is a conservative approach and does not utilise all the information available in the data. The same event may be selected by both selections, leading to an overlap in the search channels. To treat these events statistically correct and thus optimising the signal over background ratio in each bin of the mass distribution, the two search channels should be split into three: One containing events selected exclusively by the $e^+e^- \to \rho_T^0/\omega_T \to \pi_T^+\pi_T^- \to b\bar{q}\bar{b}q'$ selection, the second containing events selected exclusively by the $e^+e^- \to \rho_T^0/\omega_T \to \pi_T^+ W_L^- \to \bar{b}q\bar{q}'q''$ selection, and a third one containing all the events selected by both selections. However, interpolating the signal mass distributions for charged technipion masses where no signal Monte Carlo is available turns out to be difficult. No satisfactory solution could be obtained in the scope of this analysis and therefore the more conservative approach is used.

The excluded regions in the (m_{ρ_T/ω_T}, m_{π_T}) plane combining all search channels are shown in Figure 6.5. Here also the limits obtained in the search for $e^+e^- \to \pi_T^0\gamma \to b\bar{b}\gamma$, see [40], are included. The assumed TCSM parameters are N_{TC}=4, N_D=9, Q=5/3, and $M_V = M_A = 200$ GeV. Most of the region excluded by the $e^+e^- \to \pi_T^+\pi_T^- \to b\bar{q}\bar{b}q'$ search is also excluded by the search for $e^+e^- \to \pi_T^+ W_L^- \to \bar{b}q\bar{q}'q''$ production. Only where kinematic constraints prevent the pair production of charged technipions, the $e^+e^- \to \rho_T^0/\omega_T \to \pi_T^+\pi_T^- \to b\bar{q}\bar{b}q'$ search excludes additional points in the (m_{ρ_T/ω_T}, m_{π_T}) plane. On the other hand, this region is also excluded by the search in the $e^+e^- \to \pi_T^0\gamma \to b\bar{b}\gamma$ channel for the chosen set of TCSM parameters. However, if Q is set to zero the $e^+e^- \to \pi_T^0\gamma \to b\bar{b}\gamma$ cross–section vanishes [40] but the $e^+e^- \to \rho_T^0/\omega_T \to \pi_T^+ W_L^- \to \bar{b}q\bar{q}'q''$ process still remains

to exclude this region.

Due to the non–resonant coupling of the charged technipions to γ/Z the production cross–section for $e^+e^- \to \pi_T^+\pi_T^-$ becomes constant for $m_{\rho_T/\omega_T} \gg \sqrt{s}$, cf. section 2.3. This production mechanism depends only on m_{π_T},$\sqrt{s}$ and $N_D = 1/\sin^2(\chi)$. Therefore it is possible to calculate a limit on the technipion mass independently of the other TCSM parameters. In Figure 6.3 (a) the cross–sections for the $e^+e^- \to \rho_T^0/\omega_T \to \pi_T^+\pi_T^- \to b\bar{q}\bar{b}q'$ process with $m_{\rho_T/\omega_T} \to \infty$ is shown for N_D=2 and N_D=9 respectively. Charged technipion pair production can be excluded where the cross–sections for the process are larger than the observed upper limit on the cross–section $\times$ branching ratio shown in the same plot. A lower limit on m_{π_T} of 77 GeV is obtained at 95% CL for $N_D = 9$ independently of m_{ρ_T/ω_T} and the other parameters of the TCSM. This limit is reduced if N_D is set to 2, the minimal number of technifermion doublets in the TCSM. In this case technipion production can be excluded at 95 % CL up to a technipion mass of 63 GeV except for a small region where $56\,\text{GeV} \leq m_{\pi_T} \leq 58\,\text{GeV}$. Nevertheless, it has been checked that in this region technipion pair production can still be excluded at 95 % CL for $m_{\rho_T/\omega_T} \lesssim 1300\,\text{GeV}$.

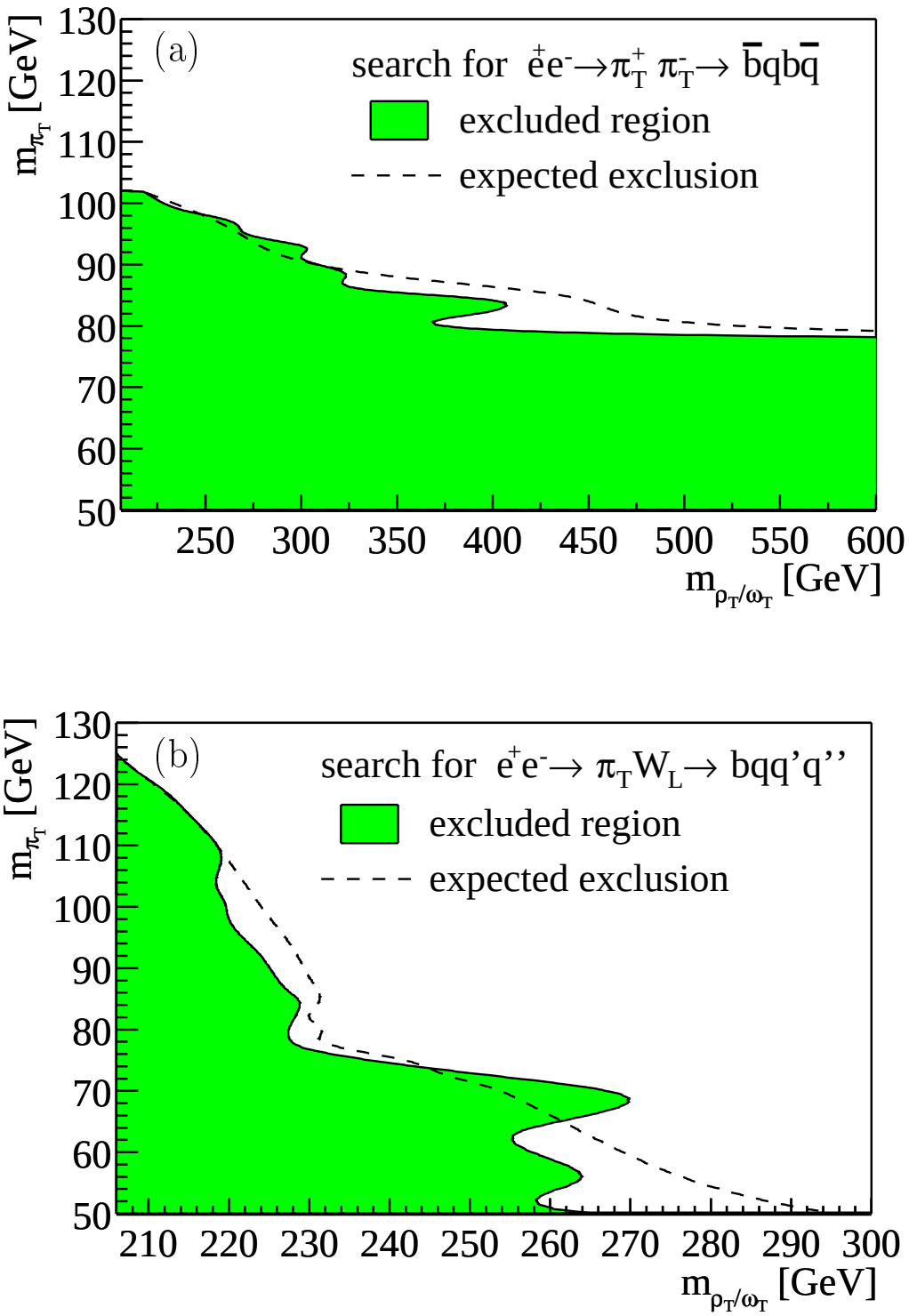

Figure 6.4: *The 95 % CL excluded region in the* $(m_{\rho_T/\omega_T}, m_{\pi_T})$ *plane from the (a)* $e^+e^- \to \rho_T^0/\omega_T \to \pi_T^+\pi_T^- \to b\bar{q}\bar{b}q'$ *and (b)* $e^+e^- \to \rho_T^0/\omega_T \to \pi_T^+ W_L^- \to \bar{b}q\bar{q}'q''$ *search. The dark grey (green) area shows the exclusion obtained from the data. The dashed line shows the corresponding median expected exclusion for the background–only hypothesis.*

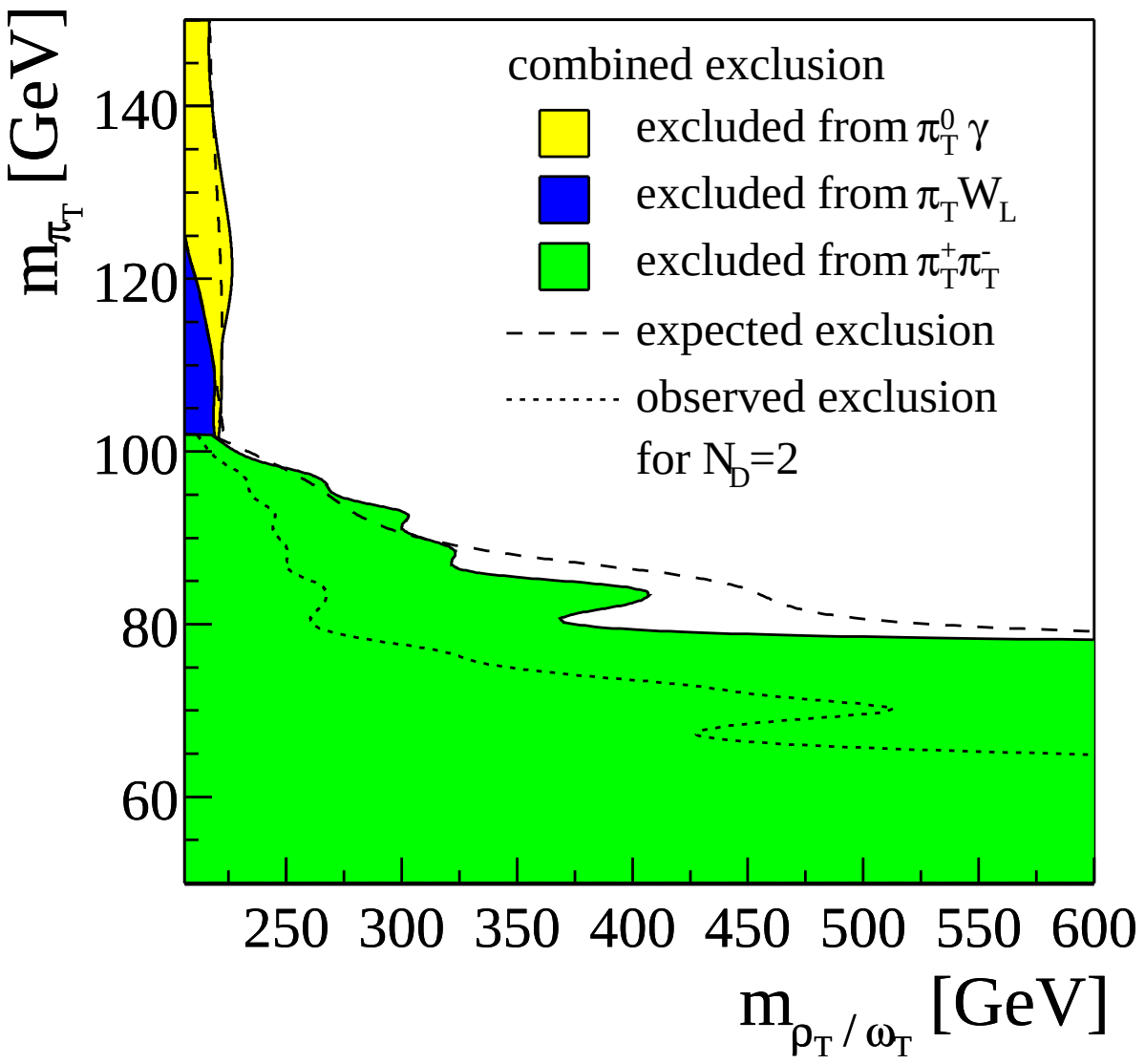

Figure 6.5: *The excluded regions at 95 % CL for all search channels considered. The dark grey (blue) area shows the region excluded by the* $e^+e^- \to \rho_T^0/\omega_T \to \pi_T^+ W_L^- \to \bar{b}q\bar{q}'q''$ *and the medium grey (green) area shows the region excluded by the* $e^+e^- \to \rho_T^0/\omega_T \to \pi_T^+\pi_T^- \to b\bar{q}\bar{b}q'$ *search. In light grey (yellow) the region excluded by the* $e^+e^- \to \rho_T^0/\omega_T \to \pi_T^0\gamma \to b\bar{b}\gamma$ *search described in [40] is also included. The boundaries of the area expected to be excluded when assuming the background–only hypothesis is shown as the dashed line.*
The dotted line indicates the area which is excluded by the $e^+e^- \to \rho_T^0/\omega_T \to \pi_T^+\pi_T^- \to b\bar{q}\bar{b}q'$ *search if the number of technifermion doublets is set to the minimal number* N_D*=2.*

Chapter 7

Summary

In this thesis, a search for Technicolor particles in electron–positron collisions at the highest centre–of–mass energies provided by the LEP storage ring is presented. The analysed data were collected by the OPAL detector in the year 2000 at centre–of–mass energies of $\sqrt{s} \approx 200 - 209\,\mathrm{GeV}$, and correspond to an integrated luminosity of $209.4\,\mathrm{pb}^{-1}$.

The search for charged technipion pair production is carried out in the $\mathrm{e^+e^-} \to \rho_T^0/\omega_T \to \pi_T^+\pi_T^- \to b\bar{q}\bar{b}q'$ channel. A total of 65 events are selected in the data, where 63.6 ± 7.0 events are expected from Standard Model processes. No significant excess over the expectation from the Standard Model is observed and therefore upper limits on the cross–section for the $\mathrm{e^+e^-} \to \rho_T^0/\omega_T \to \pi_T^+\pi_T^- \to b\bar{q}\bar{b}q'$ process are derived.

The search for the production of a charged technipion in association with a longitudinally polarised $\mathrm{W}^\pm$ is carried out in the $\mathrm{e^+e^-} \to \rho_T^0/\omega_T \to \pi_T^+\mathrm{W_L^-} \to \bar{b}q\bar{q}'q''$ channel. 138 events are selected in the data, where 127.2 ± 10.7 are expected from Standard Model processes. Again, no significant excess over the expectation from Standard Model processes is observed and upper limits on the cross–section for the $\mathrm{e^+e^-} \to \rho_T^0/\omega_T \to \pi_T^+\mathrm{W_L^-} \to \bar{b}q\bar{q}'q''$ process are derived.

The obtained upper limits on the production cross–section $\times$ branching ratio for both search channels are interpreted within the framework of the Technicolor Straw Man Model (TCSM). They can be translated directly into excluded regions in the $(m_{\rho_T/\omega_T},\, m_{\pi_T})$ plane, assuming a certain set of TCSM parameters. Here $\mathrm{N_{TC}}$=4, $\mathrm{N_D}$=9, Q=5/3, and $\mathrm{M_V} = \mathrm{M_A} = 200\,\mathrm{GeV}$ are chosen. Technipion masses up to 125 GeV, the kinematic limit in the $\mathrm{e^+e^-} \to \rho_T^0/\omega_T \to \pi_T^\pm\mathrm{W_L^\mp}$ production channel, are excluded for $m_{\rho_T/\omega_T} \approx \sqrt{s}$. ρ_T^0/ω_T masses above 206 GeV are excluded depending on $m_{\pi_T^\pm}$. For ρ_T^0/ω_T masses below 206 GeV radiative returns to the ρ_T^0/ω_T pole may be dominant. The presented analysis is not sensitive to the additional photon expected in the signal topology and therefore the obtained results are only valid for $m_{\rho_T/\omega_T} \geq \sqrt{s}$.

Due to the non–resonant coupling of the charged technipions to γ/Z, the production cross–sections for both search channels become constant for $m_{\rho_T/\omega_T} \gg \sqrt{s}$, depending only on m_{π_T},$\sqrt{s}$ and $\mathrm{N_D} = 1/\sin^2(\chi)$. The predicted cross–section for the $\mathrm{e^+e^-} \to \rho_T^0/\omega_T \to \pi_T^+\pi_T^-$ process is large enough to exclude technipion masses below 77 GeV independent of ρ_T^0/ω_T masses above 206 GeV.

A lower limit on the technipion mass independent of all other TCSM parameters can be obtained if the number of technifermion doublets assumed in the TCSM is reduced to $\mathrm{N_D}$=2, its minimal value. This minimises the predicted cross–section for the $\mathrm{e^+e^-} \to$

$\rho_T^0/\omega_T \to \pi_T^+\pi_T^- \to b\bar{q}\bar{b}q'$ process. Technipion masses up to 63 GeV can be excluded independent of the other TCSM parameters, except for a small region where $56\,\text{GeV} \leq m_{\pi_T} \leq 58\,\text{GeV}$. The latter region can still be excluded for $m_{\rho_T/\omega_T} \lesssim 1300\,\text{GeV}$.

Future hadron colliders as the LHC and the Tevatron or planned linear electron–positron colliders will continue the search for Technicolor particles. A generic prediction of Technicolor theories is the presence of a ρ_T^0/ω_T vector resonance below about 2 TeV which unitarises the W^+W^- scattering cross–section [84]. This resonance should be in reach of the future colliders and the question whether Technicolor is or is not realised in Nature is passed on to those machines.

Bibliography

[1] **ALEPH, DELPHI, L3 and OPAL** Collaboration, "Search for the Standard Model Higgs Boson at LEP." CERN-EP/2001-055, 2001.

[2] **DELPHI** Collaboration, J. Abdallah *et al.*, "Search for technicolor with delphi," `hep-ex/0110056`.

[3] **L3** Collaboration, "Search for Technicolor Production at LEP2." L3 Note 2428, 1999.

[4] **D0** Collaboration, V. M. Abazov *et al.*, "Search for heavy particles decaying into electron positron pairs in p anti-p collisions," *Phys. Rev. Lett.* **87** (2001) 061802, `hep-ex/0102048`.

[5] **CDF** Collaboration, F. Abe *et al.*, "Search for a technicolor omega(t) particle in events with a photon and a b quark jet at cdf," *Phys. Rev. Lett.* **83** (1999) 3124–3129, `hep-ex/9810031`.

[6] **CDF** Collaboration, T. Affolder *et al.*, "Search for color singlet technicolor particles in p anti-p collisions at s**(1/2) = 1.8-tev," *Phys. Rev. Lett.* **84** (2000) 1110–1115.

[7] S. Weinberg, "Implications of dynamical symmetry breaking," *Phys. Rev.* **D13** (1976) 974–996.

[8] S. Weinberg, "Implications of dynamical symmetry breaking: An addendum," *Phys. Rev.* **D19** (1979) 1277–1280.

[9] L. Susskind, "Dynamics of spontaneous symmetry breaking in the weinberg- salam theory," *Phys. Rev.* **D20** (1979) 2619–2625.

[10] P. Schmüser, *Feyman–Graphen und Eichtheorien für Experimentalphysiker*. Springer–Verlag Berlin Heidelberg, 2 ed., 1995.

[11] M. Chaichian and N. F. Nelipa, *Introduction to Gauge Field Theories*. Springer–Verlag Berlin Heidelberg, 1984.

[12] K. D. Lane, "Technicolor 2000," `hep-ph/0007304`.

[13] E. Farhi and L. Susskind, "Technicolor," *Phys. Rept.* **74** (1981) 277.

[14] K. D. Lane, "Technihadron production and decay in low-scale technicolor," *Phys. Rev.* **D60** (1999) 075007, `hep-ph/9903369`.

[15] K. D. Lane, "Technihadron production and decay rates in the technicolor straw man model," hep-ph/9903372.

[16] S. Mrenna, "Technihadron production and decay at lep2," *Phys. Lett.* **B461** (1999) 352, hep-ph/9907201.

[17] C. S. Wu, E. Ambler, R. W. Hayward, D. D. Hoppes, and R. P. Hudson, "Experimental test of parity conservation in beta decay," *Phys. Rev.* **105** (1957) 1413–1414.

[18] M. Gell-Mann *Calif. Inst. Technol. Synchrotron Lab. Rep. No. 20* (1961). Printed in: M. Gell–Mann and Y. Neeman (Hrsg.), The Eightfold Way. W.A. Benjamin, New York 1964.

[19] P. D. B. Collins, A. D. Martin, and E. Squires, *Particle physics and cosmology.* John Wiley & Sons, Inc., 1989.

[20] J. Goldstone, A. Salam, and S. Weinberg, "Broken symmetries," *Phys. Rev.* **127** (1962) 965–970.

[21] F. Englert and R. Brout, "Broken symmetry and the mass of gauge vector mesons," *Phys. Rev. Lett.* **13** (1964) 321–322.

[22] G. S. Guralnik, C. R. Hagen, and T. W. B. Kibble, "Global conservation laws and massless particles," *Phys. Rev. Lett.* **13** (1964) 585–587.

[23] P. W. Higgs, "Broken symmetries, massless particles and gauge fields," *Phys. Lett.* **12** (1964) 132–133.

[24] M. Spira and P. M. Zerwas, "Electroweak symmetry breaking and Higgs physics," hep-ph/9803257.

[25] Y. Nambu and G. Jona-Lasinio, "Dynamical model of elementary particles based on an analogy with superconductivity. i," *Phys. Rev.* **122** (1961) 345–358.

[26] J. Bardeen, L. N. Cooper, and J. R. Schrieffer, "Theory of superconductivity," *Phys. Rev.* **108** (1957) 1175–1204.

[27] M. E. Peskin and D. V. Schroeder, *Introduction to quantum field theory.* Addison–Wesley Publishing Company, 1995.

[28] Y. A. Golfand and E. P. Likhtman, "Extension of the algebra of poincare group generators and violation of p invariance," *JETP Lett.* **13** (1971) 323–326.

[29] D. V. Volkov and V. P. Akulov, "Possible universal neutrino interaction," *JETP Lett.* **16** (1972) 438–440.

[30] J. Wess and B. Zumino, "Supergauge transformations in four-dimensions," *Nucl. Phys.* **B70** (1974) 39–50.

[31] H. E. Haber, "The status of the minimal supersymmetric standard model and beyond," *Nucl. Phys. Proc. Suppl.* **62** (1998) 469–484, hep-ph/9709450.

[32] S. Dimopoulos and L. Susskind, "Mass without scalars," *Nucl. Phys.* **B155** (1979) 237.

[33] E. Eichten and K. D. Lane, "Dynamical breaking of weak interaction symmetries," *Phys. Lett.* **B90** (1980) 125.

[34] B. Holdom, "Raising the sideways scale," *Phys. Rev.* **D24** (1981) 1441.

[35] K. Yamawaki, M. Bando, and K.-i. Matumoto, "Scale invariant technicolor model and a technidilaton," *Phys. Rev. Lett.* **56** (1986) 1335.

[36] T. W. Appelquist, D. Karabali, and L. C. R. Wijewardhana, "Chiral hierarchies and the flavor changing neutral current problem in technicolor," *Phys. Rev. Lett.* **57** (1986) 957.

[37] T. Appelquist and L. C. R. Wijewardhana, "Chiral hierarchies and chiral perturbations in technicolor," *Phys. Rev.* **D35** (1987) 774.

[38] T. Appelquist and L. C. R. Wijewardhana, "Chiral hierarchies from slowly running couplings in technicolor theories," *Phys. Rev.* **D36** (1987) 568.

[39] K. D. Lane and S. Mrenna. private communication.

[40] **OPAL** Collaboration, "Searches for Technicolor with the OPAL Detector in e^+e^- Collisions at the Highest LEP Energies." OPAL PN485, 2001.

[41] **OPAL** Collaboration, K. Ahmet *et al.*, "The opal detector at lep," *Nucl. Instrum. Meth.* **A305** (1991) 275–319.

[42] **OPAL** Collaboration, S. Anderson *et al.*, "The extended opal silicon strip microvertex detector," *Nucl. Instrum. Meth.* **A403** (1998) 326–350.

[43] **OPAL** Collaboration, B. E. Anderson *et al.*, "The opal silicon - tungsten calorimeter front end electronics," *IEEE Trans. Nucl. Sci.* **41** (1994) 845.

[44] G. Aguillion *et al.*, "Thin scintillating tiles with high light yield for the opal endcaps," *Nucl. Instrum. Meth.* **A417** (1998) 266.

[45] T. Sjöstrand *et al.*, "High-energy-physics event generation with pythia 6.1," *Comput. Phys. Commun.* **135** (2001) 238–259, `hep-ph/0010017`.

[46] S. Jadach, B. F. L. Ward, and Z. Was, "Coherent exclusive exponentiation ceex: The case of the resonant e+ e- collision," *Phys. Lett.* **B449** (1999) 97–108, `hep-ph/9905453`.

[47] J. Fujimoto *et al.*, "grc4f v1.1: a four-fermion event generator for e+e- collisions," *Comput. Phys. Commun.* **100** (1997) 128–156, `hep-ph/9605312`.

[48] J. Fujimoto *et al.*, "Physics at lep2," *CERN 96-01* **2** (1996) 30.

[49] G. Corcella *et al.*, "Herwig 6: An event generator for hadron emission reactions with interfering gluons (including supersymmetric processes)," *JHEP* **01** (2001) 010, `hep-ph/0011363`.

[50] **OPAL** Collaboration, J. Allison *et al.*, "The detector simulation program for the opal experiment at lep," *Nucl. Instrum. Meth.* **A317** (1992) 47–74.

[51] R. Brun, R. Hagelberg, M. Hansroul, and J. C. Lassalle, "Geant: Simulation program for particle physics experiments. user guide and reference manual,". CERN-DD-78-2-REV.

[52] **OPAL** Collaboration, "A Matching Algorithm: MT package." OPAL TN381, 1996.

[53] **OPAL** Collaboration, "Attempt to Compensate Energy in OPAL Calorimeter Complex based on MT Package." OPAL TN447, 1996.

[54] **OPAL** Collaboration, "MT 3.00 a new algorithm to calculate energy flow based on MT package." OPAL TN575, 1998.

[55] **OPAL** Collaboration, G. Abbiendi *et al.*, "Search for neutral higgs bosons in e+ e- collisions at $\sqrt{s}$ approx. 189 GeV," *Eur. Phys. J.* **C12** (2000) 567–586, `hep-ex/9908002`.

[56] **OPAL** Collaboration, "Attempt to develop new jet–particle association methods for four–jet topology with the OPAL detector." OPAL TN579, 1998.

[57] S. Catani, Y. L. Dokshitzer, M. Olsson, G. Turnock, and B. R. Webber, "New clustering algorithm for multi - jet cross-sections in e+ e- annihilation," *Phys. Lett.* **B269** (1991) 432–438.

[58] N. Brown and W. J. Stirling, "Jet cross-sections at leading double logarithm in e+ e- annihilation," *Phys. Lett.* **B252** (1990) 657–662.

[59] S. Bethke, Z. Kunszt, D. E. Soper, and W. J. Stirling, "New jet cluster algorithms: Next-to-leading order qcd and hadronization corrections," *Nucl. Phys.* **B370** (1992) 310–334.

[60] N. Brown and W. J. Stirling, "Finding jets and summing soft gluons: A new algorithm," *Z. Phys.* **C53** (1992) 629–636.

[61] **JADE** Collaboration, W. Bartel *et al.*, "Experimental studies on multi - jet production in e+ e- annihilation at petra energies," *Z. Phys.* **C33** (1986) 23.

[62] M. Schumacher, *Suche nach neutralen Higgs–Bosonen mit dem* OPAL*–Detektor bei* LEP*2*. PhD thesis, Rheinische Friedrich–Wilhelms–Universität Bonn, Oct. 1999. Bonn-IR-99-19.

[63] **OPAL** Collaboration, "A New B-tagging Tool for LEP 2." OPAL TN576, 1998.

[64] **OPAL** Collaboration, "LB160: Upgraded B-tagging for LEP 2." OPAL TN578, 1998.

[65] **UA1** Collaboration, G. Arnison *et al.*, "Hadronic jet production at the cern proton - anti-proton collider," *Phys. Lett.* **B132** (1983) 214.

[66] **UA1** Collaboration, G. Arnison *et al.*, "Observation of jets in high transverse energy events at the cern proton - anti-proton collider," *Phys. Lett.* **B123** (1983) 115.

[67] **UA2** Collaboration, J. Alitti *et al.*, "Inclusive jet cross-section and a search for quark compositeness at the cern anti-p p collider," *Phys. Lett.* **B257** (1991) 232–240.

[68] **CDF** Collaboration, F. Abe *et al.*, "The topology of three jet events in anti-p p collisions at s**(1/2) = 1.8-tev," *Phys. Rev.* **D45** (1992) 1448–1458.

[69] **OPAL** Collaboration, "Neural Network Electron and Photon Conversion Identification." OPAL TN556, 1998.

[70] **OPAL** Collaboration, G. Abbiendi *et al.*, "Search for the standard model higgs boson in e+ e- collisions at s**(1/2) = 192-gev - 209-gev," *Phys. Lett.* **B499** (2001) 38–52, `hep-ex/0101014`.

[71] **OPAL** Collaboration, K. Ackerstaff *et al.*, "Tests of the standard model and constraints on new physics from measurements of fermion pair production at 130 GeV to 172 GeV at lep," *Eur. Phys. J.* **C2** (1998) 441–472, `hep-ex/9708024`.

[72] **OPAL** Collaboration, "Search for Charged Higgs Bosons in e^+e^- Collisions at $\sqrt{s} = 189 - 202$ GeV." OPAL PN432, 2000.

[73] **OPAL** Collaboration, G. Alexander *et al.*, "Measurement of cross-sections and asymmetries in e+ e- collisions at 130 GeV - 140 GeV center-of-mass energy," *Phys. Lett.* **B376** (1996) 232–244.

[74] G. Parisi, "Super inclusive cross-sections," *Phys. Lett.* **B74** (1978) 65.

[75] J. F. Donoghue, F. E. Low, and S.-Y. Pi, "Tensor analysis of hadronic jets in quantum chromodynamics," *Phys. Rev.* **D20** (1979) 2759.

[76] **OPAL** Collaboration, "Tracking Performance in 2000." OPAL TN657, 2000.

[77] F. Akesson. private communication.

[78] LEP Heavy Flavor Working Group, "Parameters for the LEP/SLD Electroweak Heavy Flavour Results for Summer 1998 Conferences." LEPHF/98-01, 1998.

[79] M. W. Grünewald *et al.*, "Four-fermion production in electron positron collisions," `hep-ph/0005309`.

[80] F. A. Berends, R. Pittau, and R. Kleiss, "Excalibur: A monte carlo program to evaluate all four fermion processes at lep-200 and beyond," *Comput. Phys. Commun.* **85** (1995) 437–452, `arXiv:hep-ph/9409326`.

[81] T. Junk, "Confidence level computation for combining searches with small statistics," *Nucl. Instrum. Meth.* **A434** (1999) 435–443, `hep-ex/9902006`.

[82] T. Junk, "http://thomasj.home.cern.ch/thomasj/searchlimits/mclimit.f." 2000.

[83] P. Bock, "/afs/cern.ch/user/b/bock/public/poor_mans_KEYS/histo_smear.f." private communication.

[84] **American Linear Collider Working Group** Collaboration, T. Abe *et al.*, "Linear collider physics resource book for snowmass 2001,". Resource book for Snowmass 2001, 30 Jun - 21 Jul 2001, Snowmass, Colorado.

Acknowledgments

I would like to thank Prof. Rolf–Dieter Heuer for welcoming me into his group and giving me the possibility to write my diploma thesis in a pleasant and inspiring atmosphere. For his support for the travels to CERN and Bonn I am grateful.
I am grateful to Prof. Büsser for his role as the second referee.

Without the excellent supervision of Dr. Markus Schumacher and Dr. Klaus Desch this diploma thesis would not have been possible and they receive my greatest thanks. Their patient support during the introduction to the theoretical and practical difficulties of the analysis was essential.

Another big "thank you" goes to Carsten Hensel, who never grew tired of listening to and answering my – sometimes elementary – questions. His readiness to always abandon his own work and assist me with mine was exceptional. The same is true for Götz Gaycken and Kristian Harder who always had time to help me solve my computer problems.

Thorsten Lux and his "car" often spared me the journey by underground. Thanks not only for that!

I enjoyed my time in the FLC group very much. Not only the work but also the coffee breaks were fun. I had the pleasure to be introduced to a view of the Hamburg night life I had not experienced before and I thank those people responsible for this.... You know who you are!

Without the permanent support of my parents, my studies would not have been possible. I could always count on their support and help in difficult times during all of my life. They did and do provide the solid platform on which I can rely. And finally a big kiss to Emma for understanding the need for long working hours and proof reading this thesis.